Final Report on Grant DOE-DE-EE0002750: March 1, 2010 to September 30, 2013

Philip E. Wannamaker, P.I.
University of Utah/EGI
423 Wakara Way, Suite 300
Salt Lake City, UT 84108
U.S.A.
Ph. 801-581-3547
Fx. 801-585-3540
pewanna@egi.utah.edu

Project Title: Fracture Network and Fluid Flow Imaging for Enhanced Geothermal Systems Applications from Multi-Dimensional Electrical Resistivity Structure

There are no restrictions on the distribution of this report.

Executive Summary

We have developed an algorithm for the inversion of magnetotelluric (MT) data to a 3D earth resistivity model based upon the finite element method. Hexahedral edge finite elements are implemented to accommodate discontinuities in the electric field across resistivity boundaries, and to accurately simulate topographic variations. All matrices are reduced and solved using direct solution modules which avoids ill-conditioning endemic to iterative solvers such as conjugate gradients, principally PARDISO for the finite element system and PLASMA for the parameter step estimate. Large model parameterizations can be handled by transforming the Gauss-Newton estimator to data-space form. Accuracy of the forward problem and jacobians has been checked by comparison to integral equations results and by limiting asymptotes. Inverse accuracy and performance has been verified against the public Dublin Secret Test Model 2 and the well-known Mount St Helens 3D MT data set. This algorithm we believe is the most capable yet for forming 3D images of earth resistivity structure and their implications for geothermal fluids and pathways.

Project objectives

The main goals of the project were to:

1), Develop a code for simulating 3-D EM responses over the earth's surface with topographic variations. Two platform choices were to be pursued to determine the superior approach.

2), Incorporate the selected simulation code and the inversion parameter jacobians that follow from it into an existing inversion algorithm for imaging and monitoring and improve its efficiency.

3), Parallelize the inversion code on new-generation multi-core workstations to achieve fast calculations within a single, cost-efficient, shared memory processing (SMP or multi-core) box.

4), Apply the final algorithm to two important geothermal field data sets.

In our view, the project objectives were met and substantially exceeded. The resultant 3D inversion algorithm is the best inexistence in its ability to accurately handle steep topography and achieve close-fitting inversion models in a minimal number of iterations

Technical Approach and Results

Our initial approach to the project was to further develop an existing 3D finite element modeling program placed into the public domain by the Australian research consortium at Macquarie University under the direction of now-retired Professor Art Raiche. This program solved for a magnetic Schelkunoff potential from which the E and H fields were to be obtained through local spatial differentiation. The original program invoked a severe approximation to get these fields through an integral equations approach which was especially limited for the E-field. Attempts to obtain the fields through rigorous spatial derivatives did not yield accurate results and we decided to leave this approach for another direction. A paper providing a rigorous basis for the vector potential approach was published by Kordy et al (2015, IJNAM, attached).

Consequently a new edge finite element (FE) solution for the electric field was developed by Ph.D student Michal Kordy under direction of Wannamaker. Initially we looked at dense tetrahedral elements assembled into hexahedra for straightforward adaptation of our regularization coding, checked against our long-standing integral equations code. While accurate results were obtained, convergence of the iterative matrix solver was observed to be quite slow if the mesh element aspect ratios became extreme (long, thin elements). These are required to keep the total number of unknowns in the system from becoming impractically large while at the same time honoring the very high bandwidth (range of scales of wave penetration) typical of the MT problem. Unstructured meshes can avoid that, but also are complicated for defining a regularization mesh as has typically been used, namely explicit spatial smoothing by linking neighboring conductivity subdomains. Thus, we settled upon deformable hexhedra for defining a mesh, as described below

About that time (autumn, 2012), we embarked upon using direct matrix solvers for the EM forward and jacobian simulations, motivated by our success with direct solutions for the inversion parameter step (Maris and Wannamaker, 2010, C&G, attached) and by advances in multi-core workstation capabilities. We obtained a reasonably economical workstation that contains 24 cores and 500 GB of RAM ($14K USD). We settled upon simpler uniform but deformable (for topography) hexahedral elements which produce a banded system matrix. Initially we applied the matrix tiling approach for parallelizing the LDL^T solution of the parameter step matrix to the banded FE matrix and achieved good scalability (factor of 21 for 24 cores) (Kordy et al., 2013, Proc 3DEM-5 Symp., attached). However, overall run-times were long, and thus we investigated the public domain, direct solution library MUMPS. This lead to a dramatic speedup, of ~30x, and which parallelizes moderately well (6x for 12 cores). Subsequently, we replaced MUMPS with library PARDISO, which yielded a further speedup of

~2.5 and matrix storage reduction of ~3. We are quite please with these results and current state of the algorithm.

Direct solutions are nowhere near as sensitive to element aspect ratio issues as are iterative solutions, and we find almost no sensitivity of solution time upon these ratios which can exceed 1000 in our meshes. A further great advantage of direct solutions is in the very efficient computation of auxiliary source vectors once the system matrix has been factored. This is valuable when computing all the reciprocal source vector terms that represent the parameter sensitivities. A pdf of our paper on the forward modeling is attached to this report (Kordy et al., 2016a, GJI, attached). It demonstrates the great accuracy of the program compared to the integral equations platform and with independent topographic checks. In particular, it can accurately simulate the high-frequency refraction of EM waves normal to a slope for complex models such as the Mt Erebus volcanic edifice. With a current divergence correction, accurate results also can be obtained in dielectric air.

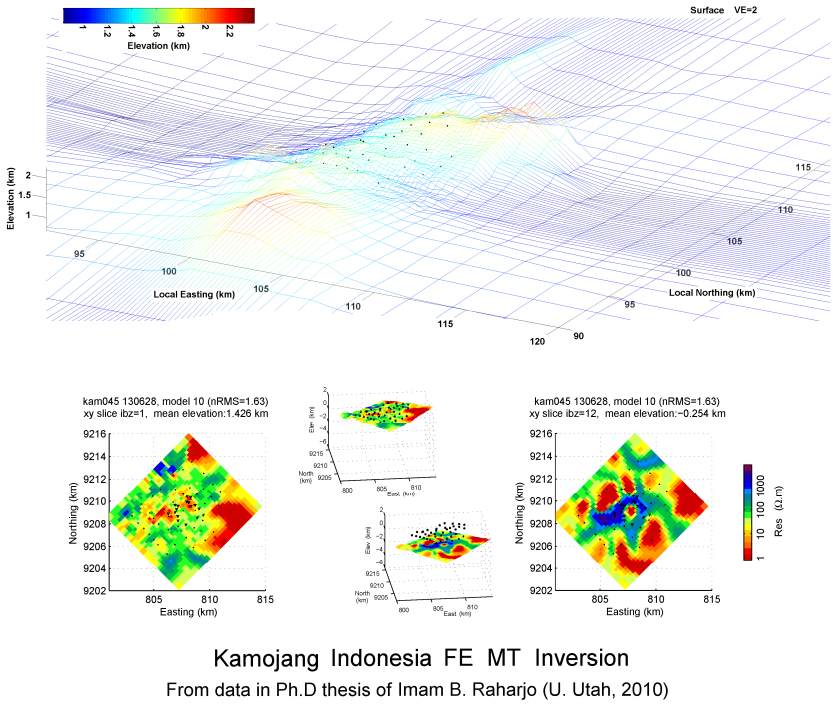

Figure 1. Field example using the new topographic finite element program for the Kamojang Indonesia MT data set. Upper panel shows deformed FE mesh and station distribution. Lower panels show plan views at shallow and fluid production levels.

The hexahedral deformable 3D mesh we now use allowed ready adaptation of the smoothing regularization matrix currently implemented in our finite difference inversion code. This was tested using simple synthetic models and also by comparison on the Sevier and Kamojang field data sets (Wannamaker et al., 2013, GRC Trans.; Raharjo et al., 2010, WGC Proc.) with good comparison (Figure 1). The Kamojang model is embedded above. Furthermore, we transformed the parameter step equation from the traditional model-space formulation to a more recent data-space formulation (Parker, 1994, Princeton Press; Siripunvaraporn et al., 2005, PEPI) as is appropriate when there are many more parameters in the tomographic volume than there are inverted data. Now, computer run-time and memory requirements of the inversion problem are almost entirely determined by the demands of the forward problem. Our published paper on the inversion technology also is appended to this report (Kordy et al.,

2016b). It includes as an example the famous Mount St Helens MT data set across its volcanic edifice. The algorithm is seeing steady use at EGI in geothermal and orogenic-scale MT data sets (e.g., Wannamaker et al., 2016, SGW).

Publications:

Kordy, M. A., P. E. Wannamaker, V. Maris, E. Cherkaev, and G. J. Hill, Three-dimensional magnetotelluric inversion using deformed hexahedral edge finite elements and direct solvers parallelized on SMP computers, Part I: forward problem and parameter jacobians: *Geophysical Journal International*, 204, 74-93, 2016.

Kordy, M. A., P. E. Wannamaker, V. Maris, E. Cherkaev, and G. J. Hill, Three-dimensional magnetotelluric inversion using deformed hexahedral edge finite elements and direct solvers parallelized on SMP computers, Part II: direct data-space inverse solution: *Geophysical Journal International*, 204, 94-110, 2016.

Kordy, M. A., E. Cherkaev, and P. E. Wannamaker, Variational formulation for Maxwell's equations with Lorenz gauge: existence and uniqueness of solution: *International Journal of Numerical Analysis and Modeling*, 12, 731-749, 2015.

Kordy, M., V. Maris, P. Wannamaker, and E. Cherkaev, 3D edge finite element solution for scattered electric field using a direct solver parallelized on an SMP workstation, *Proc. 5th International Symposium on Three-Dimensional Electromagnetics*, Sapporo, May 7-9, 4 pp., 2013.

Maris, V., and P. E. Wannamaker, Parallelizing a 3D Finite Difference MT Inversion Algorithm on a Multicore PC using OpenMP: *Computers & Geosciences*, doi: 10.1016/j.cageo.2010. 03.001, 5 pp., 2010.

At present, the inversion algorithm is considered intellectual property of the University of Utah and is not being distributed in the public domain. This situation may change in the future.

Computers & Geosciences 36 (2010) 1384–1387

Contents lists available at ScienceDirect

Computers & Geosciences

journal homepage: www.elsevier.com/locate/cageo

Short note

Parallelizing a 3D finite difference MT inversion algorithm on a multicore PC using OpenMP

Virginie Maris [a,*], Philip E. Wannamaker [b]

[a] Department of Geology and Geophysics, University of Utah, 383 F. A. Sutton Building, Salt Lake City, UT 84112, USA
[b] Energy and Geoscience Institute, University of Utah, 423 Wakara Way, Suite 300, Salt Lake City, UT 84108, USA

ARTICLE INFO

Article history:
Received 8 September 2009
Received in revised form
4 February 2010
Accepted 5 March 2010

Keywords:
Inversion
Magnetotellurics
Parallelization
Multicore processing

1. Introduction

Technology for imaging geophysical properties of the Earth's interior is increasingly demanding of computing resources as data set sizes increase and the fully three-dimensional (3D) nature of the problem is appreciated. One approach has been to develop distributed computing clusters (e.g., Hargrove et al., 2001), although these can require a substantial investment and facility footprint. An attractive alternative is to exploit multicore PC designs to which single-processor personal computers (PC's) have evolved; this presents the prospect of parallel computing within an affordable, single-box, format.

Here, we describe modifications made to a 3D magnetotelluric (MT) inversion program to allow it to run efficiently on a multicore desktop PC. Parallelization is accomplished using OpenMP, an easy to use application program interface developed for shared-memory platforms, such as multicore PC's. Auto-parallelization, while attractive, is unlikely to yield improvements as large as can be obtained by restructuring and explicit parallelization. We demonstrate that excellent scalability with increasing core number is achieved on important parts of the inverse problem, while particular processor architecture limits efficiency in other parts of the problem.

2. Magnetotelluric inversion overview

MT is a geophysical technique, whereby naturally occurring electromagnetic (EM) waves are used as source fields for imaging Earth's electrical resistivity structure at depths ranging from tens of meters to hundreds of kilometers (Vozoff, 1991; Simpson and Bahr, 2005). It is used in resource exploration and in earthquake and volcano studies. Estimating a discretized subsurface resistivity model from MT data is accomplished by non-linear regularized inversion, requiring minimization of a parametric functional P of the form (Eq. (1)) (Tarantola, 1987, 2005; Zhdanov, 2002)

$$P = \|\boldsymbol{d}_{pre} - \boldsymbol{d}_{obs}\|_2^2 + \|S(\boldsymbol{m})\|_2^2 \quad (1)$$

The recovered resistivity structure, described by model parameters $\boldsymbol{m}$, is that which minimizes the misfit between predicted ($\boldsymbol{d}_{pre}$) and observed ($\boldsymbol{d}_{obs}$) data, subject to a stabilizing functional S such as, for example, a first order differencing matrix emphasizing spatially smooth models. Data are predicted at sounding locations, one frequency at a time, by solving Maxwell's equations to simulate the propagation of quasi-static EM fields, throughout the model, for two orthogonal external plane wave sources. A difficult and computationally intense task, 3D MT inversion remains an active research area (Avdeev, 2005).

Sasaki (2004) developed a Gauss–Newton MT inversion algorithm for serial PC's, using the staggered-grid finite-difference method to solve Maxwell's equations. Minimization of Eq. (1) requires linearizing the forward operator representing Maxwell's equations, accomplished by introducing the Fréchet derivative

* Corresponding author. Tel.: +1 801 581 5126; fax: +1 801 585 3540.
E-mail addresses: vmaris@egi.utah.edu (V. Maris), pewanna@egi.utah.edu (P.E. Wannamaker).

0098-3004/$ - see front matter
doi:10.1016/j.cageo.2010.03.011

matrix $\boldsymbol{F}$, and yielding a system of the form (Eq. (2))

$$[\boldsymbol{F}^T\boldsymbol{F}+\boldsymbol{S}^T\boldsymbol{S}]\Delta\boldsymbol{m}=[\boldsymbol{F}^T(\boldsymbol{d}_{pre}-\boldsymbol{d}_{obs})] \quad (2)$$

where $\boldsymbol{S}$ represents the stabilizing functional, the matrix on the left ($[\boldsymbol{F}^T\boldsymbol{F}+\boldsymbol{S}^T\boldsymbol{S}]$), forms the approximate regularized Hessian, and the vector $(\boldsymbol{d}_{pre}-\boldsymbol{d}_{obs})$ is the residual. Determining the model update $\Delta\boldsymbol{m}$ requires calculating, for some starting model, predicted data and their Fréchet derivatives with respect to a change in model parameters. Fréchet derivatives are computed by imposing, one at a time, four reciprocal dipole sources (two electric, two magnetic) at each sounding location for each frequency, and simulating the fields throughout the domain. Numerically approximating Maxwell's equations generates a system of equations, where the system matrix is identical for all sources and receivers at a particular frequency, while the source vectors vary. Sparse and symmetric with complex diagonal and real off-diagonal entries, the number of rows in the system matrix is proportional to the number of finite-difference nodes. Fields are solved using the biconjugate gradient method, with a divergence correction procedure developed by Smith (1996) to improve convergence rates when processing low frequencies. The model update is obtained by factoring the approximate regularized Hessian, a dense, real, and symmetric matrix, using the LDL^T method (Golub and Van Loan, 1996).

The most time-consuming tasks are calculating the Fréchet derivative matrix, and factoring the Hessian. The serial Fortran77 program has been restructured and parallelized under Linux using OpenMP 2.0 directives embedded in the source code and tested on an Intel Xeon 5355, 2.66 GHz, 8-core PC, with 16 GB of RAM. Two key areas were parallelized, the frequency loop containing the forward modeling, residual and Fréchet derivative calculations, and the factoring of the Hessian matrix. The modifications do not impair serial performance of the program, which can be run with and without the parallelization enabled. We wished to avoid the added complexity of message passing interface (MPI) protocols and examine how much could be achieved using widely accessible, commercial compiler capabilities.

3. Frequency loop parallelization

As there are no dependencies between frequencies, the frequency-indexed loop containing the forward modeling, residual, and Fréchet derivative calculations, originally implemented serially, is readily amenable to coarse-grained parallelization. The modified program assigns to a separate thread the calculations pertaining to a single frequency, until all frequencies have been processed. Threads execute simultaneously and asynchronously. All shared variables are either frequency-indexed or left unmodified. The full Fréchet matrix is never formed. It can be considered as a column of submatrices, each containing the terms for a particular frequency. Only the submatrix entries pertaining to the frequency being processed are stored; once the submatrix is complete, it is written to a scratch file for retrieval when generating the Hessian matrix, and the array is cleared. The residual array is handled similarly. Once all frequencies have been processed, the program exits the parallel section and the misfit is calculated.

Increasing the number of CPU's decreases the time required to process the frequency loop (Fig. 1). However, speedup appears limited. Simulated field calculations are dominated by sparse–matrix–vector computations implemented conventionally using compressed storage. Performance in such tasks is limited largely by the processor-to-memory performance gap (Buttari et al., 2007); these computations on a single processor usually run at 10% or less of the peak floating point performance (Vuduc et al., 2002). With several processes sharing resources, data congestion further degrades speedup. Solving for the fields due to different sources concurrently rather than sequentially, thus transforming inherent sparse–matrix–vector operations into sparse–matrix–matrix operations, improves performance and speedup (Fig. 1). When calculating Fréchet derivatives, fields due to the four dipole sources, at each receiver, are solved for concurrently. Independent solution update and exit criteria of the biconjugate gradient and divergence correction methods are maintained. Fields required for calculating the predicted data are similarly handled.

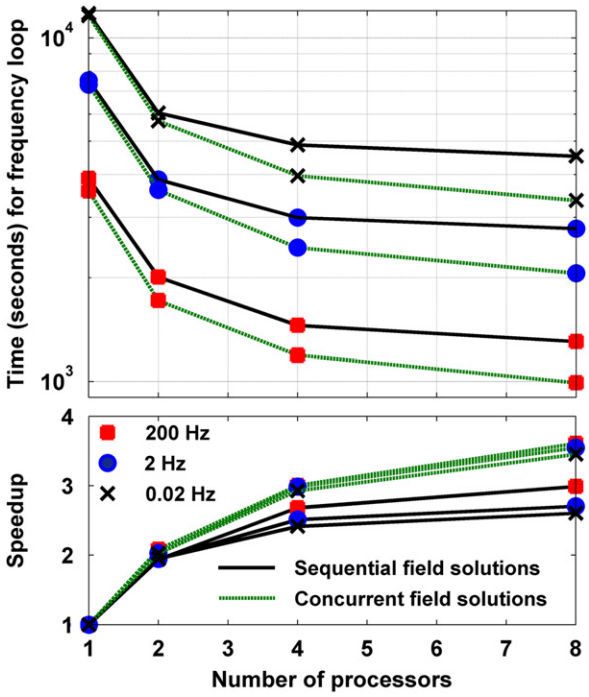

Fig. 1. Time required (top panel) and speedup (bottom panel) observed when calculating predicted data, residual, and Fréchet derivatives at eight frequencies for a synthetic data set. Speedup is calculated as ratio of execution times required, when using one processor and when using several. Synthetic data were generated using a 3D model for 100 sounding locations, over a finite difference mesh, with $35\times35\times29$ nodes. Generally, the higher the frequency, the more quickly field solution converges (Smith, 1996). To avoid complication of different frequencies taking different serial run times, separate tests of scalability were carried out with all eight frequencies assigned identical values of 200, 2, and 0.2 Hz.

4. Parameter update parallelization

We have used fine-grained, asynchronous parallelization (Buttari et al., 2007) to implement the LDL^T method of factoring the approximate regularized Hessian matrix for the model parameter update. To reduce the storage requirements, the diagonal and triangular entries of the Hessian matrix are stored in a 1D array, of length NP(NP−1)/2, where NP is the number of parameters. The $\boldsymbol{F}^T\boldsymbol{F}$ term of the Hessian is generated in double precision in a separate parallel section after the frequency loop and then stored in single precision. The algorithm is based on a block-cyclic column layout similar to that used by Baboulin et al. (2005), within a simple construct consisting of OpenMP locks (Fig. 2). The matrix is subdivided into smaller blocks; work propagates from block to block both horizontally and vertically, maximizing reuse of the data in each block. Each thread is assigned one column of blocks, starting from the leftmost and progressing sequentially through to the rightmost column. Once the leading triangle and adjacent block of a row have been

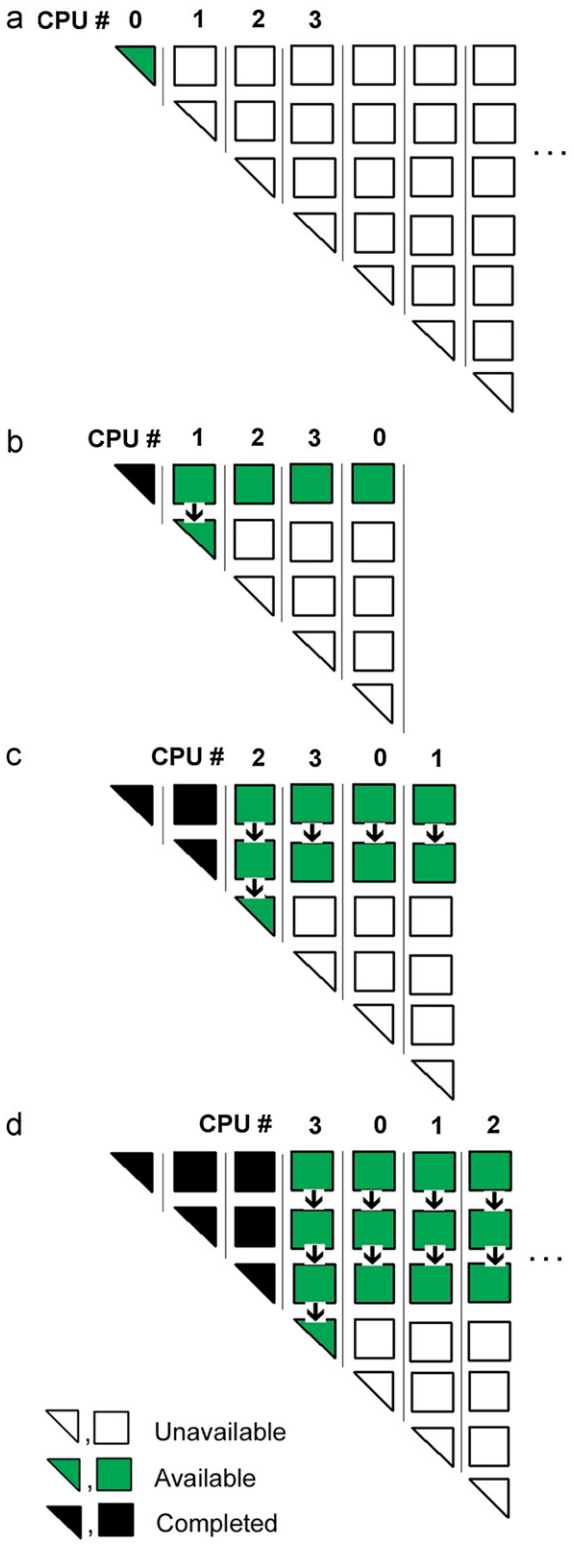

Fig. 2. Schematic representation of workflow for LDL^T factorization, for four CPU's. Work proceeds from panel **a** through panel **d**. For each panel, blocks which are unavailable as yet to process are colored white; those in which processing has been completed are colored black. Remaining blocks are available to be processed, with work in each thread propagating in direction indicated by arrows.

operated on, the algorithm assigns work to proceed vertically down to the leading triangle beneath, or horizontally to adjacent blocks. A column of blocks must be completely processed, before releasing the CPU to a queued column. Numerical accuracy in

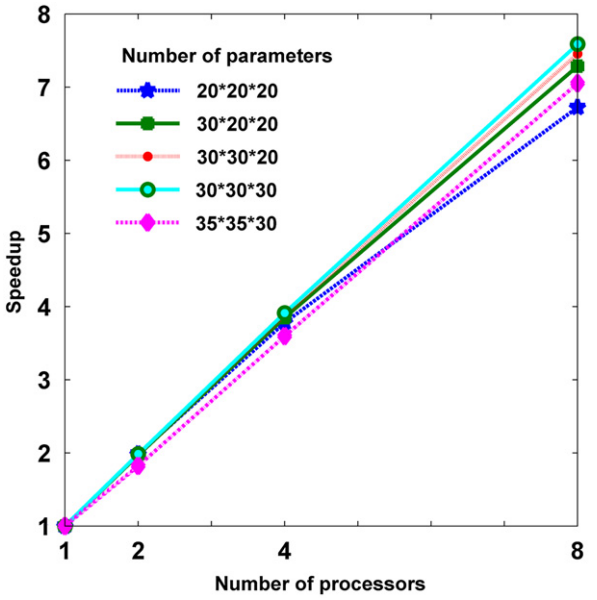

Fig. 3. Speedup observed when factoring Hessian matrix using the LDL^T method. Matrices of order equal to the number of parameters were tested.

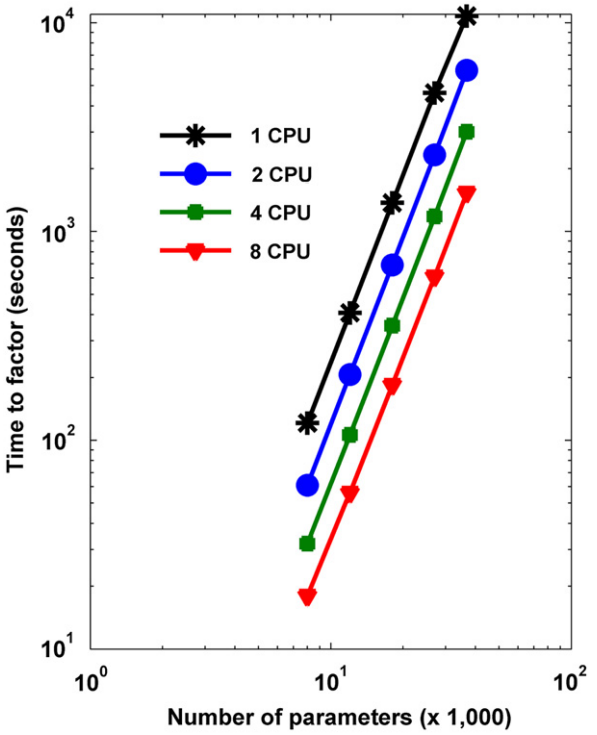

Fig. 4. Time required to factor a matrix using the LDL^T method, as a function of number of parameters and number of CPUs active.

factoring is maintained through double-precision operations and rolling sums. OpenMP locks ensure that blocks are not operated on prematurely by requiring that each thread acquires ownership of the leading triangle prior to working on a block of the same row, stalling until the lock becomes available. The simplicity of this implementation is possible, because we do not require pivoting. Doubling the number of processors used to factor the system matrix, approximately halves the time required (Fig. 3). The NP^3 dependence of runtime, consistent with O(NP^3) operations required by LDL^T factoring, is preserved (Fig. 4).

5. Conclusions

We have achieved substantial efficiency increases for 3D MT inversion by parallelizing an original serial algorithm to run on multicore PC's. Parallelization of the forward modeling, residual, and Fréchet derivative calculations is implemented by assigning the calculations for each frequency to separate threads, which can execute concurrently. Increasing the number of CPU's used allows more frequencies to be processed at the same time, decreasing the time required. Scalability is reduced due to lags in data transfers; newer processor architectures are expected to improve this considerably (Barker et al., 2008). Fine-grained and asynchronous parallelization of the LDL^T process, used to obtain the model parameter update, is implemented by using the block-cyclic algorithm and compact storage. The time required to factor the system is essentially halved as the number of CPU's doubles at least for the 8-core platform considered here. Taken together, these modifications have resulted in significantly reducing the time required to complete a 3D MT inversion, while operating in a single workstation format.

Acknowledgments

This work was supported by U.S. Department of Energy contracts DE-PS36-04GO94001 and DE-EE0002750, and National Science Foundation Grant EAR0440050. Maris received additional support from the Stan and Shirley Ward, and the Charlie and Jean Smith, graduate student scholarships of the Society of Exploration Geophysicists. We thank Professor Yutaka Sasaki for providing the original source code for the finite difference inversion. Fortran programming and parallelization were under the Lahey LF64 v8.0 compiler using the Fedora 8 Linux OS. Clarity of this short note was improved by comments from reviewer Antje Franke-Boerner and an anonymous reviewer.

References

Avdeev, D.B., 2005. Three-dimensional electromagnetic modelling and inversion from theory to application. Surveys in Geophysics 26, 767–799.

Baboulin, M., Giraud, L., Gratton, S., 2005. A parallel distributed solver for large dense symmetric systems: applications to geodesy and electromagnetism problems. International Journal of High Performance Computing Applications 19, 353–363.

Barker, K.J., Davis, K., Hoisie, A., Kerbyson, D.J., Lang, M., Pakin, S., Sancho, J.C., 2008. A performance evaluation of the Nehalem quad-core processor for scientific computing. Parallel Processing Letters 18, 453–469.

Buttari, A., Dongarra, J., Kurzak, J., Langou, J., Luszczek, P., Tomov, S., 2007. The impact of multicore on math software. In: Proceedings of the Workshop on State-of-the-art in Scientific and Parallel Computing (Para06), Umea, Sweden, Springer's Lecture Notes in Computer Science 4699, 1–10.

Golub, G., Van Loan, C., 1996. Matrix Computations third ed. John Hopkins University Press, London 694pp.

Hargrove, W.W., Hoffman, F.M., Sterling, T., 2001. The do-it-yourself supercomputer. Scientific American 256, 72–79.

Sasaki, Y., 2004. Three-dimensional inversion of static-shifted magnetotelluric data. Earth Planets and Space 56, 239–248.

Simpson, F., Bahr, K., 2005. Practical Magnetotellurics. University Press, Cambridge 270pp.

Smith, J.T., 1996. Conservative modeling of 3-D electromagnetic fields, Part II: biconjugate gradient solution and an accelerator. Geophysics 61, 1319–1324.

Tarantola, A., 1987. Inverse Problem Theory. Elsevier, New York 613pp.

Tarantola, A., 2005. Inverse Problem Theory and Methods for Model Parameter Estimation. Society for Industrial and Applied Mathematics, Philadelphia 352pp.

Vozoff, K., 1991. The magnetotelluric method. In: Nabighian, M.N. (Ed.), Electromagnetic Methods In Applied Geophysics, Society of Exploration Geophysics, pp. 641–711.

Vuduc, R., Demmel, J.W., Yelick, K.A., Kamil, S., Nishtala, R., Lee, B., 2002. Performance optimizations and bounds for sparse–matrix–vector multiply. In: Proceedings of the 2002 ACM/IEEE conference on Supercomputing, Baltimore, MD, USA, 1–35.

Zhdanov, M.S., 2002. Geophysical Inverse Theory and Regularization Problems. Elsevier, Oxford 609 pp.

3D Edge Finite Element Solution for Scattered Electric Field using a Direct Solver Parallelized on an SMP Workstation

Michal Kordy[1,2], Virginie Maris[1], Phil Wannamaker [1] and Elena Cherkaev[2]
[1]Energy and Geoscience Institute at the University of Utah
[2]Department of Mathematics at the University of Utah

SUMMARY

We have implemented an edge finite element solution to simulate the Helmholtz equation for scattering of the electric field from subsurface electrical conductivity structure. First-order elements on hexahedral grid are used where the electric field is constant along the edges and varies linearly between edges. Choosing this basis allows the incorporation of topography through deformation of the mesh, and yields a relatively compact system matrix structure. The frequency range considered is appropriate for diffusive EM propagation in a conducting earth, but we retain dielectric properties for the air medium. A secondary E-field formulation is used that facilitates arbitrary impressed sources, which we have tested so far using plane-wave (MT) source fields. Several factors discussed herein have motivated us to migrate from iterative to direct system matrix solvers. Using a matrix tiling approach too parallelizing the modified Cholesky (LDLT) factorization, we have achieved excellent scalability on a 24-core workstation with 0.5 TB RAM. However, use of a direct solution even with double precision arithmetic does not necessarily escape parasitic E-fields in the form of gradient of a scalar potential, especially in the air. Hence, a divergence correction also using a parallelized direct solver was implemented and successfully recovers the correct field. The magnetic field, obtained by curl of E, is not affected by this problem. Good agreement using this solution is obtained for conductive and resistive prisms in a half space, and for a simple hill structure, in comparison to other approaches.

Keywords: forward modeling, finite element, divergence correction, multicore CPU, direct solver, edge elements

FINITE ELEMENT FORMULATION

Consider Maxwell's equations in the frequency domain with $e^{i\omega t}$ time dependence, with the electric source J^{imp}:

$$\begin{cases} \nabla \times E &= -i\omega\mu H \\ \nabla \times H &= \hat{\sigma}E + J^{imp}\,, \qquad \hat{\sigma} = \sigma + i\omega\epsilon \end{cases} \tag{1}$$

The weak form of the equation for E, with homogeneous tangential Dirichlet boundary conditions, is given below:

$$\int_\Omega \frac{1}{\mu}\nabla \times E \cdot \nabla \times K + i\omega \int_\Omega \hat{\sigma}E \cdot K = \int_\Omega J^{imp} \cdot K \tag{2}$$

satisfied for all $K \in H_0(\nabla\times)$. The solution of this equation E is in the same space $H_0(\nabla\times)$, defined as a family of vector fields $K : \Omega \to \mathbb{C}^3$, such that:

$$\int_\Omega ||K||^2 + \int_\Omega ||\nabla \times K||^2 < \infty, \;\; n \times K|_{\partial\Omega} = 0$$

For a finite mesh, $H_0(\nabla\times)$ space is replaced with finite dimensional space $H_0^h(\nabla\times)$ of linear combinations of first order edge shape functions N_i where i is an edge index. A linear system of equations is obtained

$$Ax = b \tag{3}$$

$$A_{i,j} = \left[\int_\Omega \frac{1}{\mu}\nabla \times N_i \cdot \nabla \times N_j + i\omega \int_\Omega \hat{\sigma}N_i \cdot N_j\right] \tag{4}$$

$$b_i = \int_\Omega J^{imp} \cdot N_i \tag{5}$$

Vector x contains coefficients of a linear combination of shape functions. The approximation of the electric field is

$$E = \sum_{i=1}^{n_e} x_i N_i \tag{6}$$

Magnetic field is then calculated from (1) as

$$H = \frac{-\nabla \times E}{i\omega} \tag{7}$$

PARALLEL DIRECT SOLVER

There are several reasons why a direct solver is considered in this paper. Because of the presence of the air in the domain, and as a result the small value of $\omega\hat{\sigma} = \omega^2\epsilon_0$, especially for small frequencies, the system matrix is ill conditioned. The condition number is further increased if element aspect ratios become extreme which is a common issue with a structured hexahedral mesh if the mesh boundaries are to be sufficiently far from the center of the domain. High condition number causes an iterative solution to be slow. Moreover, some geoelectrical methods as well as direct Gauss-Newton inversion approaches require that many source vectors be solved; this can become much more efficient with direct solutions once the system matrix has been factored. Finally, recent advances in the power of symmetric multiprocessing (SMP) computers make available an affordable, single-box workstation with numerous cores to parallelize and up to 1 TB of memory.

The system matrix is symmetric, complex valued and, for a structured grid, banded. As a result LDLT factorization will result in L matrix that has the same bandwidth as the original matrix. This allows one to store only the portion of the matrix within the outer band (2% of the memory is required for the biggest model considered in this paper, with 97x97x50 elements). We discuss parallel factorization at a later point.

DIVERGENCE CORRECTION

Even though a direct solver is used, because of finite precision (double precision is used here), the electric field in the air can experience oscillatory behavior especially toward low frequencies. This is due to a parasitic solution of the form $\nabla\varphi$, which is added to the true solution (e.g., (Smith, 1996)). This error requires a divergence correction to the electric field.

For $H_0(\nabla\times)$ space, there exists a Hodge decomposition (Bochev & Gunzburger, 2006), a decomposition into the range of the gradient $R(\nabla)$ (which is equal to the null space of the curl) and the space orthogonal to it $R(\nabla)^{\perp_{\hat{\sigma}}}$:

$$H_0(\nabla\times) = R(\nabla) \oplus R(\nabla)^{\perp_{\hat{\sigma}}}$$

where

$$\begin{aligned} R(\nabla) &= \{\nabla\varphi : \varphi \in G_0\} \\ R(\nabla)^{\perp_{\hat{\sigma}}} &= \{K \in C_0 : \textstyle\int_\Omega \hat{\sigma} K \cdot \nabla\varphi = 0 \ \forall_{\varphi\in G_0}\} \end{aligned}$$

Let the solution E to equation (2) be represented by

$$E = \nabla\varphi_E + E_\perp \quad \varphi_E \in G_0, \ E_\perp \in R(\nabla)^{\perp_{\hat{\sigma}}}$$

By setting $K = K_\perp \in R(\nabla)^{\perp_{\hat{\sigma}}}$ and then $K = \nabla\varphi$, one can show that (2) is equivallent to two uncoupled equations on $R(\nabla)^{\perp_{\hat{\sigma}}}$ and $R(\nabla)$ respectively.

$$\begin{aligned} \textstyle\int_\Omega \frac{1}{\mu}\nabla\times E_\perp\cdot\nabla\times K_\perp + i\omega\int_\Omega \hat{\sigma}E_\perp\cdot K_\perp &= \textstyle\int_\Omega J^{imp}\cdot K_\perp \\ i\omega\textstyle\int_\Omega \hat{\sigma}\nabla\varphi_E\cdot\nabla\varphi &= \textstyle\int_\Omega J^{imp}\cdot\nabla\varphi \end{aligned}$$

Imposing the second of the two equations is called divergence correction. This correction is important when $\omega\hat{\sigma}$ is small.

Edge elements on hexahedral grid are designed in such a way that the Hodge decomposition holds, if one considers the gradient operating on the space of node shape functions defined on the same grid (Bochev & Gunzburger, 2006). Divergence correction requires solving a Poisson equation which has 3 times less variables, and the matrix has three times smaller bandwidth, than the finite element system matrix. Thus to store the correction matrix in a banded dense format one needs 9 times less memory, and the factorization is about 10 times faster, than for the system matrix.

NUMERICAL RESULTS

Models considered

First we consider two models of a prism in a half space. The prism has dimensions 2km x 1km x 2km and its upper side is buried 500m below the ground. The conceptual plot of this model is presented on Figure 1. Both coarser and finer discretization grids are computed, with the central portion of the finer presented in Figure 2.

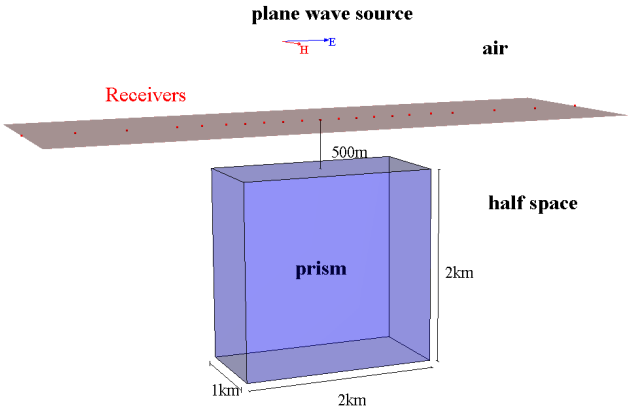

Figure 1. Conceptual plot of a prism in half space model

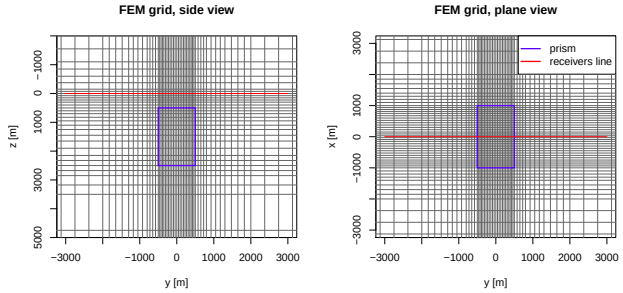

Figure 2. Central portion of the hexahedral grid for finer mesh for prisms in half-space; side and plane view

The first model is a conductive (1Ωm) in a 100Ωm half-space. The second model is a resistive (1000Ωm) prism in a 10Ωm half-space. For both of the prism models we calculate the electric field with plane wave source going downwards, with incident electric field in x-direction and magnetic field in y-direction. The code solves for the scattered field — the difference between the total E-field with the prism and the E-field of half space background only.

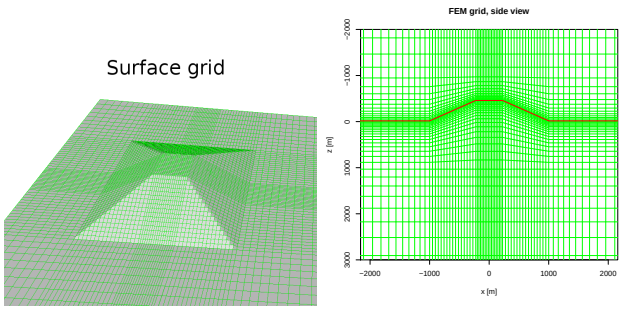

Figure 3. Central portion of the finer grid for 3-D hill model

The third model is the 3D trapezoidal hill considered in (Nam et al., 2007). The hill is 0.45 km high, 0.45 km wide at the hilltop and 2 km wide at the base. The calculations are

done for a single frequency 2Hz, and the magnetotelluric response is compared with the response in (Nam et al., 2007). The finer grid of two grids considered is presented in Figure 3.

Calculated field

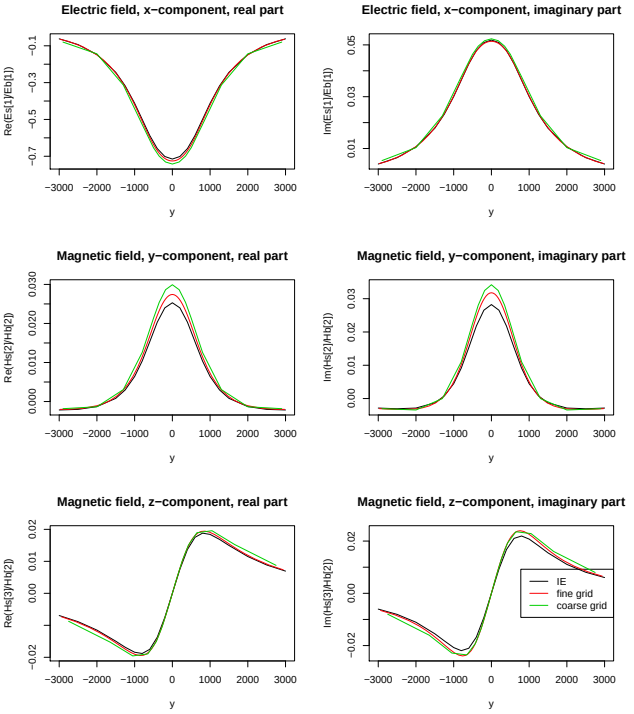

Figure 4. The electric field E and magnetic field H calculated for a **conductive prism** (1Ωm) in a 100Ωm half-space; frequency $\mathbf{0.1Hz}$

For the coarse prism grid of 21x22x23 elements, there were 29,042 unknowns, while for the finer grid of 85x88x46 elements there were 1,001,583 unknowns. The factorization of the system matrix, using 24-core CPU took 10 seconds, and 2 hours and 15 minutes, for the coarse and fine prisms respectively. Electric and magnetic fields at the surface calculated for the conductive prism, normalized by their primary fields, are compared with those from the Integral Equation (IE) code (Wannamaker., 1991) in Figure 4 at 0.1 Hz. For the IE computations, the prism was divided into 20 bricks of equal dimension in the x-y-z directions. Agreement appears good for both discretizations. Similarly good agreement was obtained for 10Hz and 0.001Hz, but is not plotted to save space. For the model of a resistive prism in a half space, the agreement between methods is good as well at 0.1Hz (figure 5), and similarly for 10Hz and 0.001Hz.

For the 3D-hill model two grids were tried. The finer grid has 97x97x50 elements and as a result the number of unknowns (edges inside the domain) is 1,373,376. To store the system matrix in dense banded format, 301GB was needed. The factorization of the system matrix, using 24 core-CPU took 4 hours and 46 minutes. A coarser grid has 27x27x24 elements, the number of unknowns is 48,516, the memory needed to store the system matrix is 1.4GB, and the factorization time is 30 s.

Our values for apparent resistivity and phase from the MT impedance elements Z_{xy} and Z_{yz} are compared in Figure 6 with those in Nam et al (2007), which we have digitized. The agreement between the results is considered very good. Apart from using a direct solver, it is worth noting that both our and the Nam formulations are the same: edge finite elements of the first order on hexahedral grid. The grids presented here also differ from Nam et al, which was 31x31x24. In part the large grid was computed to test direct solution run times for model sizes that could be practical for moderately large field data sets.

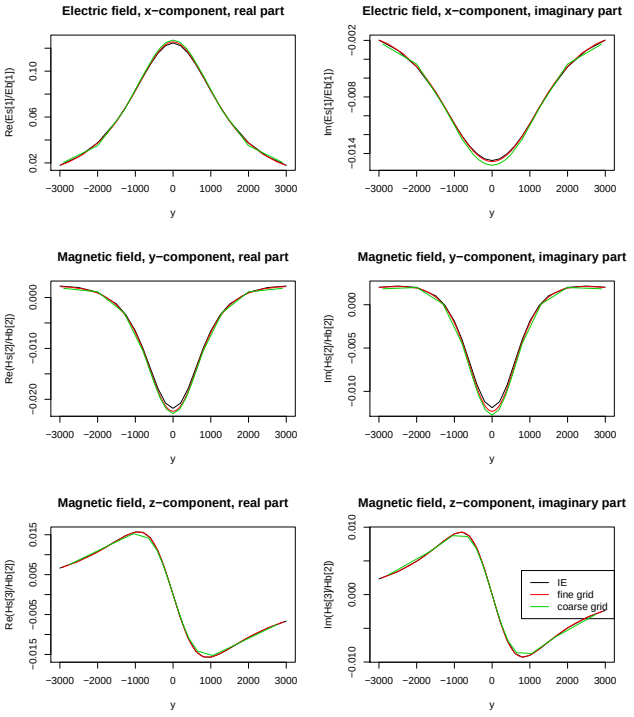

Figure 5. The electric field E and magnetic field H calculated for a **resistive prism** (1000Ωm) in a 10Ωm half-space; frequency $\mathbf{0.1Hz}$

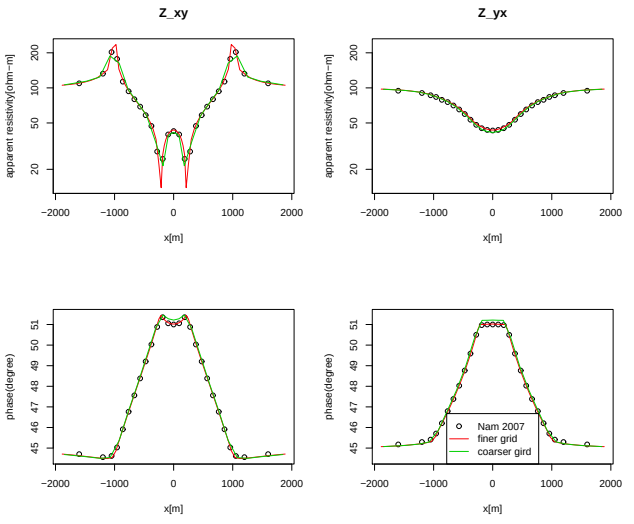

Figure 6. The apparent resistivity and the phase calculated for Z_{xy} and for Z_{yx} for a 3-D hill model

Divergence correction

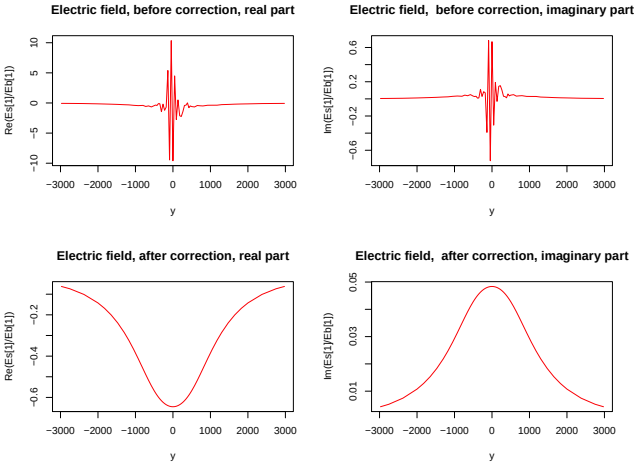

Figure 7. The electric field E calculated for a conductive prism (1Ωm) in a 100Ωm half-space; calculated **in the air**, at height 75m; frequency **0.1Hz**; before and after divergence correction

Using our conductive prism as an example, the electric field response at 0.1Hz before and after the divergence correction is presented in Figure 7. One can observe that the field values before the correction have large numerical error especially over center of the body which divergence correction successfully removes. The divergence error is even worse at the lower frequency of 0.001Hz, but again can be fully corrected as in Figure 8. It is worth noting that the magnetic field in the air (not plotted), which is calculated using curl of the electric field (see equation (7)) is not affected by the parasitic solution and has the same (proper) value before and after the correction. The divergence problem was not visible at the frequency 10Hz.

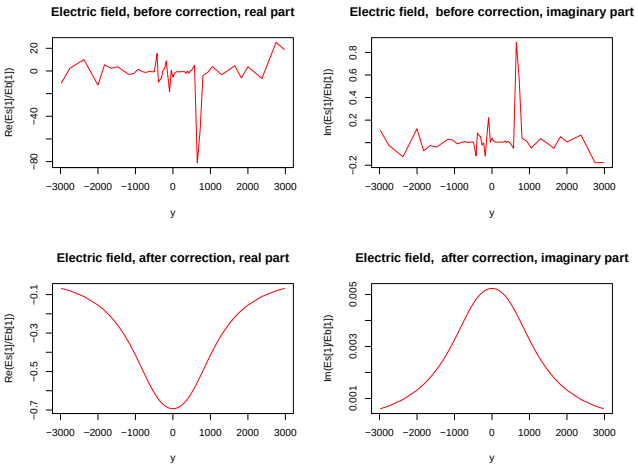

Figure 8. The electric field E calculated for a conductive prism (1Ωm) in a 100Ωm half-space; calculated **in the air**, at height 75m; frequency **0.001Hz**; before and after divergence correction

Direct solver scalability

A parallel factorization algorithm, that uses a matrix tiling approach in modified Cholesky (LDLT) factorization, described in detail in Maris and Wannamaker (2010), has been adapted to complex valued and banded matrices. The scalability of the direct solver, measured in the speedup in the factorization time depending on the number of cores used, is presented in Figure 9. The values were calculated on a model with grid: 53x53x38, number of unknowns: 306,696, and the system matrix in the dense banded format needed 28GB. We achieve nearly linear speedup versus number of cores. Efficiency of this process is still being researched, for example determining the optimal tile size relative to processor cache memory.

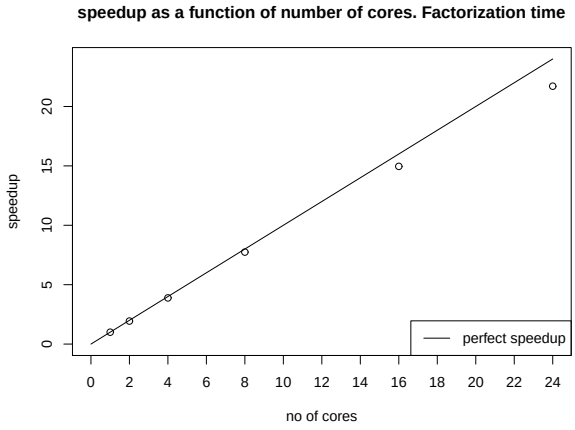

Figure 9. Scalability of the factorization measured in speedup (time of factorization using one core/ time of factorization using n cores)

ACKNOWLEDGEMENTS

This research and presentation was supported under U.S. Dept. of Energy contract DE-EE0002750 to P. Wannamaker.

REFERENCES

Bochev, P., & Gunzburger, M. (2006). Least-squares finite element methods. In *Proceedings of the international congress of mathematicians (icm)*. Madrid.

Maris, V., & Wannamaker, P. E. (2010, October). Parallelizing a 3D finite difference MT inversion algorithm on a multicore PC using OpenMP. *Computers and Geosciences*, *36*, 1384-1387.

Nam, M. J., Kim, H. J., Song, Y., Lee, T. J., Son, J. S., & Suh, J. H. (2007). 3D magnetotelluric modelling including surface topography. *Geophysical Prospecting*, *55*, 277-287.

Smith, J. (1996). Conservative modeling of 3-d electromagnetic fields, part ii: Biconjugate gradient solution and an accelerator. *Geophysics*, *61*(5), 1319-1324.

Wannamaker., P. (1991). Advances in three-dimensional magnetotelluric modeling using integral equations. *Geophysics*, *56*, 1716-1728.

INTERNATIONAL JOURNAL OF
NUMERICAL ANALYSIS AND MODELING
Volume 12, Number 4, Pages 731–749

VARIATIONAL FORMULATION FOR MAXWELL'S EQUATIONS WITH LORENZ GAUGE: EXISTENCE AND UNIQUENESS OF SOLUTION

MICHAL KORDY, ELENA CHERKAEV, AND PHIL WANNAMAKER

Abstract. The existence and uniqueness of a vector scalar potential representation with the Lorenz gauge (Schelkunoff potential) is proven for any vector field from H(curl). This representation holds for electric and magnetic fields in the case of a piecewise smooth conductivity, permittivity and permeability, for any frequency. A regularized formulation for the magnetic field is obtained for the case when the magnetic permeability μ is constant and thus the magnetic field is divergence free. In the case of a non divergence free electric field, an equation involving scalar and vector potentials is proposed. The solution to both electric and magnetic formulations may be approximated by the nodal shape functions in the finite element method with system matrices that remain well-conditioned for low frequencies. A numerical study of a forward problem of a computation of electromagnetic fields in the diffusive electromagnetic regime shows the efficiency of the proposed method.

Key words. Lorenz gauge, Schelkunoff potential, Maxwell's equations, Finite Element Method, Nodal shape functions, Regularization

1. Introduction

Fast and stable methods are needed for calculating electromagnetic (EM) fields in and over the Earth. Such a simulation has applications in imaging of subsurface electrical conductivity structures related to exploration for geothermal, mining, and hydrocarbon resources. Over commonly used frequencies, EM propagation in the Earth is diffusive since the conduction dominates over the dielectric displacement. The finite element method (FEM) is attractive for this simulation in comparison with other techniques in that it may be easily adapted to complex boundaries between regions of constant EM properties, including the topography or the bathymetry. The 3D interpretation of geophysical data is numerically expensive, as the forward problem needs to be computed many times [26, 3, 14].

For large scale simulation problems, iterative methods have been the ones of choice to solve linear systems resulting from FEM formulations [7, 16, 11, 34, 29]. The speed of iterative methods is strongly related to the properties of the variational problem used. Difficulties arise when the computational domain includes a high contrast, both the non-conducting air and a conducting medium in the Earth's subsurface, especially for low frequencies. Furthermore, the Earth's subsurface in general is characterized by the spatially changing conductivity, dielectric permittivity and magnetic permeability. This can slow or prevent iteration convergence [23, 31].

There have been multiple approaches to addressing the difficulties encountered with high physical property contrasts and potentially discontinuous EM field variables. One is to apply special finite elements, so-called edge elements, that have a discontinuous normal component of the vector field across elements, while keeping the tangential field component continuous [24, 18, 4]. The edge elements are also

Received by the editors June 21, 2013 and, in revised form, January 25, 2015.
2000 *Mathematics Subject Classification.* 65N30,86A04,35Q61.

compatible with the curl operator and are a part of the de Rham diagram [6]. However, if the curl-curl equation for the electric field E is used, and if the conductivity is very small in a part of the domain (e.g., in the air) or if the frequency is very low, the problem becomes ill-posed and the system matrix has a very large near null space. This requires use of sophisticated preconditioners that handle the null space of the curl properly in order to use iterative solvers. Such preconditioners have been developed (see [38, 17, 19, 21, 2, 39]).

An alternative is to not solve directly for the EM fields themselves, but instead to initially solve a well conditioned equation for a quantity which is continuous across interfaces. Subsequently, the EM fields are obtained through a spatial differentiation with the field discontinuities defined by the property jumps. One such quantity is a vector potential with the Lorenz gauge, also called the Schelkunoff potential [37, 8, 33, 9], which we examine in this paper. In general, this potential has both scalar and vector components, and there are both electric and magnetic versions. Using the Lorenz gauge, the scalar potential can be expressed as a function of the vector potential, and as a result only the vector potential is needed to represent the EM field.

In this paper, we show that the Lorenz gauged vector potential representation exists for any member of $\mathcal{H}(\nabla\times)$. Thus one can use it to represent the electric field E as well as the magnetic field H. We prove that this representation exists for any frequency $\omega > 0$, if the permittivity ϵ is bounded and the magnetic permeability μ and the conductivity σ are bounded away from 0 and ∞. The electromagnetic properties ϵ, μ, σ are allowed to be discontinuous. We discuss an application of this potential for FEM approximation of the EM field. In principle, it is enough to use only the vector Lorenz gauged potential to represent the EM field. However, when the conductivity σ is not constant and the electric field is not divergence-free, it is difficult to find a weak equation involving only the vector potential. In particular, we show that the vector potential does not satisfy the weak form of the Helmholtz equation, sometimes erroneously used as a basis for FEM simulation [33]. For the general case of non divergence-free EM fields, we propose a mixed formulation involving the scalar and vector potentials.

We consider also the case of representing the magnetic field using a vector potential with the Lorenz gauge. If the magnetic permeability μ is constant, the magnetic field is divergence-free and the vector potential coincides with the magnetic field. We show that the Lorenz gauge approach leads to a regularized weak equation for the magnetic field involving a divergence term, and as a result the equation does not suffer from the large near null space.

We show that sesquilinear forms of the equations for both magnetic vector potential and electric scalar-vector formulations remain coercive at low frequencies. It makes iterative solvers fast even if only standard vector multigrid preconditioners [35] are used. Another advantage is that the considered vector potential is a member of $\mathcal{H}(\nabla\times) \cap \mathcal{H}(\nabla\cdot)$. This allows to use nodal elements, which have more widely available implementations than edge elements. The edge elements, due to a discontinuity of the shape functions across elements boundaries, require post processing to get a value of a field at a specific point within an element. In geophysical applications, the domain is a convex polygon, so nodal discretization is dense in $\mathcal{H}_0(\nabla\times) \cap \mathcal{H}(\nabla\cdot)$ or in $\mathcal{H}(\nabla\times) \cap \mathcal{H}_0(\nabla\cdot)$ [13, 6].

Regularization of the curl-curl equation using a divergence term has been also suggested in [1, 13]. The current paper extends these ideas to the case of non-constant, complex valued electromagnetic properties and non divergence-free fields.

In [1], the authors consider the existence, the uniqueness and proper boundary conditions for a Lorenz gauged vector potential only for the case of constant electromagnetic properties. In [13], the authors consider non-constant properties; however, they seek a solution $E \in \mathcal{H}(\nabla\times)$ such that $\sigma E \in \mathcal{H}(\nabla\cdot)$. If σ is not constant, it is difficult to construct a compatible finite element discretization for the space of vector fields of the suggested kind.

In this paper, we consider a different approach. The vector potential term $-i\omega A$ and the vector electric field E differ by $\nabla\varphi$. The scalar potential φ satisfies the Poisson equation for which the source term is given by the jumps of the normal component of E across boundaries of regions with different EM properties. Representing the discontinuities of the electric field using $\nabla\varphi$ allows the vector potential to be continuous, or more precisely to lie in the space $\mathcal{H}(\nabla\times)\cap\mathcal{H}(\nabla\cdot)$, which allows to approximate it using the nodal elements.

A representation of the electric field related to our vector-scalar formulation was considered in ([9] Lorenz gauge #2), where the authors proved the uniqueness of the Schelkunoff potential continuous across interfaces for a nonlossy medium using a mixed formulation that involved both scalar and vector potentials. The mixed formulation involving scalar and vector potentials considered in the current paper (section 6) is a reformulation of this approach for a medium with losses. We prove not only the uniqueness, but also the existence of the solution (Theorem 6.1).

A closely related work was presented in [15], where the authors consider an eddy current problem, with $\epsilon = 0$ and $\sigma > 0$ in a part of the domain and $\epsilon = \sigma = 0$ in the rest of the domain. They show existence and uniqueness of the vector potential representation with the Lorenz gauge. They consider also a mixed formulation similar to ours. Here, we consider $\epsilon > 0$. Also in our equation we apply a scaling to the scalar potential, which makes a sesquilinear form coercive at $\omega \to 0$. Finally our proof of the coercivity is more general, it does not require a smallness of the coefficients used in the equation.

The structure of the paper is as follows. In section 2, a brief description of the vector-scalar representation of the electric field with the Lorenz gauge is given in the way it typically appears in the literature. We also show that it satisfies the Helmholtz equation if the electromagnetic properties are constant.

In the third section, a theorem of the existence and the uniqueness of a Lorenz gauged vector potential representation for any vector field in $\mathcal{H}(\nabla\times)$ is formulated and proven.

The purpose of section 4 is to build some intuition about the vector potential with the Lorenz gauge. We consider a representation of the electric field by the Schelkunoff potential. We present conditions that are satisfied on an interface between two regions with different conductivity. We show how a jump in the normal component of the electric field is represented by a jump of the normal derivative of the scalar potential, allowing the vector potential to be continuous.

In section 5, a difficulty in obtaining a weak equation involving only the vector electric Schelkunoff potential is presented.

In section 6, a mixed formulation involving a scalar and a vector potential is developed for the electric Schelkunoff potential.

In section 7, a different approach is suggested to avoid the difficulties with the electric potential. A magnetic Schelkunoff potential is defined and, in the situation where magnetic permeability μ is constant, an appealing weak form of the governing equation is derived.

The last section (8) shows results of numerical simulations. We use the developed magnetic Schelkunoff potential approach to calculate the electromagnetic field generated by a conductive brick in a resistive whole space with a plane-wave (magnetotelluric) source. A comparison of the results with calculations done by an independent Integral Equations code [36], is shown. A good agreement between the calculated fields provides a verification of the validity of the method.

2. Lorenz gauged formulation of Maxwell's equations

Let us consider the electromagnetic field satisfying Maxwell's equations in the frequency domain, with a time dependence $e^{i\omega t}$, with the electric source J^{imp}, in some bounded domain $\Omega \subset \mathbb{R}^3$:

$$\left\{ \begin{array}{rcl} \nabla \times E &=& -i\omega\mu H \\ \nabla \times H &=& \hat{\sigma} E + J^{imp} \end{array} \right. , \qquad \hat{\sigma} = \sigma + i\omega\epsilon \tag{1}$$

Here, σ and ϵ are the conductivity and the permittivity of the medium, μ is the magnetic permeability, and ω is the frequency.

The Schelkunoff potential, or the electric Schelkunoff potential, is a vector potential A used together with a scalar potential φ to represent the electric field E [37, 8, 33, 9] in a form:

$$E = -i\omega A + \nabla\varphi \tag{2}$$

A relationship between A and φ, called the Lorenz gauge, is imposed:

$$\nabla \left(\frac{\nabla \cdot A}{\hat{\sigma}\mu} \right) = \nabla\varphi \tag{3}$$

As a result the electric field is represented as:

$$E = -i\omega A + \nabla \left(\frac{\nabla \cdot A}{\hat{\sigma}\mu} \right) \tag{4}$$

Substituting the first equation to the second one in (1) and using (2) to represent the electric field E, in a region of *constant properties* $\hat{\sigma}, \mu$ we obtain:

$$\nabla \times \left(\nabla \times \frac{1}{\mu} A \right) = J^{imp} - \hat{\sigma} i\omega A + \hat{\sigma} \nabla\varphi$$

Application of the vector identity (51) results in:

$$\nabla \left(\nabla \cdot \frac{1}{\mu} A \right) - \nabla \cdot \left(\nabla \left(\frac{1}{\mu} A \right) \right) = J^{imp} - \hat{\sigma} i\omega A + \hat{\sigma} \nabla\varphi$$

If the equation is multiplied by $-\mu$ (it is assumed that $\hat{\sigma}, \mu$ are constant), the Lorenz gauge (3) is used, then the following vector Helmholtz equation is obtained:

$$\Delta A - i\hat{\sigma}\mu\omega A = -\mu J^{imp} \tag{5}$$

Yet the vector potential satisfies this equation only if the electromagnetic properties are constant. The weak form of the Helmholtz equation is a separate equation for each component A_k of the vector field, $k = 1, 2, 3$. For any test function $K_k \in \mathcal{H}^1(\Omega)$ the following is satisfied:

$$\int_\Omega \nabla K_k \cdot \nabla A_k + i\omega \int_\Omega \hat{\sigma}\mu A_k \cdot K_k = \int_\Omega \mu J_k^{imp} \cdot K_k \tag{6}$$

The equation above imposes conditions on interfaces between regions of different $\hat{\sigma}, \mu$ listed below:

1. A_k is continuous, $k = 1, 2, 3$ 2. $\frac{\partial}{\partial n} A_k$ is continuous, $k = 1, 2, 3$

where n is a vector normal to the interface. In section 3 the existence and the uniqueness of an electric Schelkunoff potential satisfying those conditions is investigated. As it turns out, with some reasonable assumptions when $\hat{\sigma}, \mu$ are not constant, an electric Schelkunoff potential continuous across interfaces (condition 1 is satisfied) exists, yet the condition 2 is not satisfied. As a result there is no electric Schelkunoff potential that satisfies the weak form of the Helmholtz equation (6), so it should not be used as a basis for finite element approximation if the electromagnetic properties are not constant.

3. Existence and uniqueness of the Schelkunoff potential

In this section we formulate and prove a theorem stating the existence and the uniqueness of the Schelkunoff potential. All is done in an abstract setting that uses the theory of the Sobolev spaces. Some physical interpretation, for the case of representation of the electric field E, is given in the following section.

Consider an open bounded domain $\Omega \subset \mathbb{R}^3$ with Lipschitz boundary. We use the following notation for the Sobolev spaces:

$$
\begin{array}{cl}
L^2 & = L^2(\Omega) = \left\{\psi : \Omega \to \mathbb{C} : \int_\Omega |\psi|^2 < \infty\right\} \\
\mathcal{H}^1 & = \mathcal{H}^1(\Omega) = \left\{\psi : \Omega \to \mathbb{C} : \int_\Omega |\nabla\psi|^2 + \int_\Omega |\psi|^2 < \infty\right\} \\
\mathcal{H}(\nabla\times) & = \mathcal{H}(\nabla\times, \Omega) = \left\{K : \Omega \to \mathbb{C}^3 : \int_\Omega |\nabla \times K|^2 + \int_\Omega |K|^2 < \infty\right\} \\
\mathcal{H}(\nabla\cdot) & = \mathcal{H}(\nabla\cdot, \Omega) = \left\{K : \Omega \to \mathbb{C}^3 : \int_\Omega |\nabla \cdot K|^2 + \int_\Omega |K|^2 < \infty\right\}
\end{array} \tag{7}
$$

If homogeneous boundary conditions are assumed, a subscript "0" is added. For $\mathcal{H}_0^1$, $\mathcal{H}_0(\nabla\times)$, $\mathcal{H}_0(\nabla\cdot)$, the value of the function, tangential and normal components of a vector field are fixed respectively. If n is a vector normal to the boundary $\partial\Omega$, then

$$
\begin{array}{cccccc}
\mathcal{H}_0^1 & = & \mathcal{H}_0^1(\Omega) & = & \left\{\psi \in \mathcal{H}^1(\Omega) : \psi|_{\partial\Omega} = 0\right\} \\
\mathcal{H}_0(\nabla\times) & = & \mathcal{H}_0(\nabla\times, \Omega) & = & \{K \in \mathcal{H}(\nabla\times, \Omega) : n \times K|_{\partial\Omega} = 0\} \\
\mathcal{H}_0(\nabla\cdot) & = & \mathcal{H}_0(\nabla\cdot, \Omega) & = & \{K \in \mathcal{H}(\nabla\cdot, \Omega) : n \cdot K|_{\partial\Omega} = 0\}
\end{array} \tag{8}
$$

Additionally, the notation for norms is as follows:

$$
\begin{array}{rcl}
\|\psi\|_0 & = & \sqrt{\int_\Omega |\psi|^2} \\
\|\psi\|_1 & = & \sqrt{\|\psi\|_0^2 + \|\nabla\psi\|_0^2} = \sqrt{\int_\Omega |\psi|^2 + \int_\Omega |\nabla\psi|^2}
\end{array} \tag{9}
$$

We use the following Poincare inequality (see Appendix A in [6]). There is a constant $c > 0$, dependent on the domain Ω, such that:

$$
c\|\psi\|_0 \le \|\nabla\psi\|_0 \quad \text{for } \psi \in \mathcal{H}_0^1 \tag{10}
$$

Theorem 3.1. *For a vector field $G \in \mathcal{H}_0(\nabla\times)$ and a scalar complex valued function γ satisfying*

$$
\begin{array}{rcl}
\gamma & = \gamma_R + i\gamma_I, & \gamma_R, \gamma_I : \Omega \to \mathbb{R} \\
|\gamma_R| & \le \gamma_{RM} < \infty & \\
0 < \gamma_{Im} \le |\gamma_I| & \le \gamma_{IM} < \infty & \\
\gamma_I > 0 \text{ in } \Omega & \text{or} \quad \gamma_I < 0 \text{ in } \Omega &
\end{array} \tag{11}
$$

there is a unique $T \in \mathcal{H}_0(\nabla\times) \cap \mathcal{H}(\nabla\cdot)$ satisfying

$$
\frac{\nabla \cdot T}{\gamma} \in H_0^1 \tag{12}
$$

$$
G = T + \nabla\left(\frac{\nabla \cdot T}{\gamma}\right) \tag{13}
$$

Proof. Consider an equation for $\varphi \in \mathcal{H}_0^1$:

$$\int_\Omega \nabla\varphi \cdot \nabla\overline{\psi} - \int_\Omega \gamma\varphi\overline{\psi} = \int_\Omega G \cdot \nabla\overline{\psi} \tag{14}$$

satisfied for any $\psi \in \mathcal{H}_0^1$. We will prove that there is a unique solution φ to this equation, $\varphi = \frac{\nabla\cdot T}{\gamma}$. It is obvious that with assumptions (11), the sesquilinear form

$$\mathcal{B}(\varphi,\psi) = \int_\Omega \nabla\varphi \cdot \nabla\overline{\psi} - \int_\Omega \gamma\varphi\overline{\psi} \tag{15}$$

is bounded with respect to the norm $\|.\|_1$, defined in (9). We will prove that $\mathcal{B}$ is also coercive.

$$|\mathcal{B}(\psi,\psi)| = \left|\int_\Omega |\nabla\psi|^2 - \int_\Omega \gamma|\psi|^2\right| = \left|\left(\int_\Omega |\nabla\psi|^2 - \int_\Omega \gamma_R|\psi|^2\right) - i\int_\Omega \gamma_I|\psi|^2\right|$$

If the real part of a complex number is decreased, then the modulus is decreased, so we can write that for any $\alpha \in (0,1]$

$$\begin{array}{ll} |\mathcal{B}(\psi,\psi)| & \geq \left|\alpha\left(\int_\Omega |\nabla\psi|^2 - \int_\Omega \gamma_R|\psi|^2\right) - i\int_\Omega \gamma_I|\psi|^2\right| \\ & \geq \frac{1}{\sqrt{2}}\left[\left|\alpha\left(\int_\Omega |\nabla\psi|^2 - \int_\Omega \gamma_R|\psi|^2\right)\right| + \left|\int_\Omega \gamma_I|\psi|^2\right|\right] \\ & \geq \frac{1}{\sqrt{2}}\left[\alpha\left(\int_\Omega |\nabla\psi|^2 - \int_\Omega |\gamma_R\|\psi|^2\right) + \int_\Omega |\gamma_I\|\psi|^2\right] \\ & \geq \frac{1}{\sqrt{2}}\left[\alpha\left(\|\nabla\psi\|_0^2 - \gamma_{RM}\|\psi\|_0^2\right) + \gamma_{Im}\|\psi\|_0^2\right] \\ & \geq \min\left(\frac{\alpha}{\sqrt{2}}, \frac{\gamma_{Im}-\alpha\gamma_{RM}}{\sqrt{2}}\right)\left(\|\nabla\psi\|_0^2 + \|\psi\|_0^2\right) \end{array} \tag{16}$$

This proves the coercivity of $\mathcal{B}$ if only α is taken such that $\frac{\gamma_{Im}}{\gamma_{RM}} > \alpha > 0$.

As $G \in \mathcal{H}_0(\nabla\times) \subset (L^2)^3$, the right hand side of (14) is a bounded linear functional on H_0^1, thus from the Lax-Milgram theorem there is a unique $\varphi \in \mathcal{H}_0^1$ satisfying (14).

Define

$$T = G - \nabla\varphi \tag{17}$$

As $\varphi \in \mathcal{H}_0^1$, then $\nabla\varphi \in \mathcal{H}_0(\nabla\times)$. As $G \in \mathcal{H}_0(\nabla\times)$, we conclude that $T \in \mathcal{H}_0(\nabla\times)$.

Take any smooth function with a compact support in Ω, $\psi \in \mathcal{C}_c^\infty(\Omega)$. Such a function is also in $\mathcal{H}_0^1$, so it satisfies (14). Evaluation of $\nabla\cdot T$ at ψ gives

$$\langle \nabla\cdot T, \psi\rangle = -\int_\Omega T\cdot\nabla\overline{\psi} \overset{(17)}{=} -\int_\Omega (G-\nabla\varphi)\cdot\nabla\overline{\psi} \overset{(14)}{=} \int_\Omega \gamma\varphi\overline{\psi}$$

This shows that $\nabla\cdot T$ is a function and

$$\nabla\cdot T = \gamma\varphi$$

As $|\gamma| \leq \sqrt{\gamma_{RM}^2+\gamma_{IM}^2} < \infty$ and $\varphi \in L^2$, then $\nabla\cdot T \in L^2$, which proves that $T \in \mathcal{H}(\nabla\cdot)$. Moreover as $\gamma \neq 0$, we have

$$\frac{\nabla\cdot T}{\gamma} = \varphi \tag{18}$$

which proves (12). Definition (17) of T, together with (18) proves (13). □

Remark 3.2.

- *One could consider non-homogeneous Dirichlet boundary conditions. For any $G \in \mathcal{H}(\nabla\times)$ the same proof would give a vector potential $T \in \mathcal{H}(\nabla\times)\cap\mathcal{H}(\nabla\cdot)$ such that $n\times T = n\times G$ on $\partial\Omega$.*

- *One could consider $G \in \mathcal{H}(\nabla\times)$ and a different potential T, satisfying different boundary conditions. If equation (14) is considered for $\phi, \psi \in \mathcal{H}^1$, it will lead to $T \in \mathcal{H}(\nabla\times) \cap \mathcal{H}_0(\nabla\cdot)$. To prove that in this case T has the normal component equal to 0 on $\partial\Omega$, one can take any $\psi \in \mathcal{H}^1$ and evaluate*

$$\int_{\partial\Omega} (T\cdot n)\overline{\psi} = \int_\Omega T\cdot\nabla\overline{\psi} + \int_\Omega (\nabla\cdot T)\overline{\psi} = \int_\Omega (G-\nabla\varphi)\cdot\nabla\overline{\psi} + \int_\Omega \gamma\varphi\overline{\psi} = 0$$

- *In the case of (14) for $\varphi, \psi \in \mathcal{H}^1_0$ assumption $|\gamma_I| > 0$. may be weakened. Even if $\gamma_I = 0$ the theorem holds as long as $\gamma_{RM} \neq 0$ and $\gamma_{RM} < c$, where c is the constant in Poincare inequality (10). The proof of the coercivity has to be adapted as follows. Continuing with the calculation (16) for $\alpha = 1$ we obtain for some β, such that $1 > \beta > \frac{\gamma_{RM}}{c} > 0$:*

$$\begin{aligned}\sqrt{2}|\mathcal{B}(\psi,\psi)| &\geq \|\nabla\psi\|^2 - \gamma_{RM}\|\psi\|^2 = (1-\beta)\|\nabla\psi\|^2 + \beta\|\nabla\psi\|^2 - \gamma_{RM}\|\psi\|^2 \\ &\geq min(1-\beta, \beta c - \gamma_{RM})(\|\nabla\psi\|^2 + \|\psi\|^2)\end{aligned}$$

Corollary 3.3. *To obtain the Schelkunoff potential representation (4) of the electric field E, one has to set $G = E$, $T = -i\omega A$ and $\gamma = -i\omega\mu\hat{\sigma} = \omega^2\epsilon\mu - i\omega\sigma\mu$. The assumptions (11) of Theorem 3.1 will be satisfied for any $\omega > 0$ if there exist constants $\mu_m, \mu_M, \sigma_m, \sigma_M, \epsilon_M$ such that*

$$\begin{array}{rcl} & |\epsilon| & \leq \epsilon_M < \infty \\ 0 < \sigma_m \leq & \sigma & \leq \sigma_M < \infty \\ 0 < \mu_m \leq & \mu & \leq \mu_M < \infty \end{array} \tag{19}$$

4. Interface conditions

In this section, we discuss interface conditions of the Schelkunoff potential for the electric field E. Consider a fragment of the domain Ω with two subsets V_1, V_2 and the interface $\partial V_1 \cap \partial V_2$ between them (see Figure 1). For simplicity, we assume that all considered vector and scalar fields are smooth in V_1 as well as in V_2, and have limits of values and derivatives on the interface $\partial V_1 \cap \partial V_2$, yet the limit if one approaches the interface from V_1 may be different from the limit if one approaches the interface from V_2. With this assumption, the members of $\mathcal{H}^1$, such as the scalar potential φ, are continuous across the interface. The members of $\mathcal{H}(\nabla\times)$, such as the electric field E and $\nabla\varphi$ have continuous tangential components across the interface, but may have discontinuous normal components. Members of $\mathcal{H}(\nabla\times) \cap \mathcal{H}(\nabla\cdot)$, such as A and T have continuous both tangential and normal components across the interface. The fields in the subdomain V_j are denoted by a subscript "j". The vector normal to the surface and pointing out of V_1, towards V_2 (see Figure 1), is denoted by n.

Let us consider representation (2) of the electric field E, with $\varphi = \frac{\nabla\cdot A}{\hat{\sigma}\mu}$. In this representation, all the components, E, A, $\nabla\varphi$ are members of $\mathcal{H}(\nabla\times)$, so they have continuous tangential components across the interface. Analysis of the normal components is more interesting. Using the fact that the normal component of A has to be continuous, we obtain the condition on the jump of the normal derivative of φ:

$$\begin{array}{rcl} -i\omega\,(n\cdot A_1) & = & -i\omega\,(n\cdot A_2) \\ n\cdot(E_1 - \nabla\varphi_1) & = & n\cdot(E_2 - \nabla\varphi_2) \\ n\cdot(\nabla\varphi_2 - \nabla\varphi_1) & = & n\cdot(E_2 - E_1) \end{array} \tag{20}$$

We will show that this is exactly the condition imposed by equation (14). Integrating equation (14) by parts for a test function ψ with the support in the interior

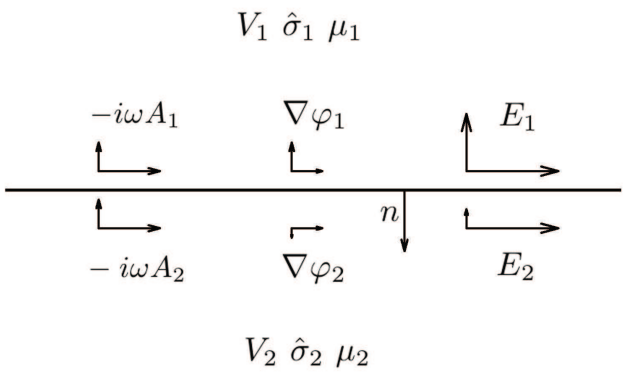

FIGURE 1. The properties $\hat{\sigma}$, μ experience a jump on $\partial V_1 \cap \partial V_2$. As a result the normal component of E has a jump. The field $\nabla\varphi$ is chosen in such a way, that its normal component jump allows $-i\omega A$ to be continuous.

of $V_1 \cup V_2$ and using $G = E$, we obtain the following:

$$\begin{aligned}\int_{V_1\cup V_2}[-\nabla\cdot\nabla\varphi-\gamma\varphi]\overline{\psi}+\int_{\partial V_1\cap\partial V_2} n\cdot(\nabla\varphi_1-\nabla\varphi_2)\overline{\psi}=\\ -\int_{V_1\cup V_2}(\nabla\cdot E)\overline{\psi}+\int_{\partial V_1\cap\partial V_2} n\cdot(E_1-E_2)\overline{\psi}\end{aligned} \tag{21}$$

For a test function with the support entirely in V_1 or entirely in V_2, the interface terms are 0, hence

$$\nabla\cdot\nabla\varphi+\gamma\varphi=\nabla\cdot E \tag{22}$$

almost everywhere in $V_1 \cup V_2$. Using this result in (21), for a test function non-zero on the interface, one gets only the boundary terms and subsequently one obtains condition (20) for the jump in the normal derivatives of φ.

Notice that in many applications, the source term J^{imp} in (1) is divergence free. If additionally $\hat{\sigma} = \text{const}$ in V_1 and in V_2, then taking divergence of the second equation in (1), one obtains that

$$\nabla\cdot E=0$$

in V_1 as well as in V_2. In this case, the strong equation (22) has the right hand side equal to zero. As a result the source term in (14) is related only to the jump of the normal component of E. More precisely if E has a jump in the normal component, then its divergence is a distribution. This distribution is the source term in equation (14).

If the electromagnetic properties have corners or edges, then the electric field has singularities [12], which can be represented by a gradient of a scalar function $\nabla\varphi$. The Lorenz gauged vector potential that we consider, exploits exactly this property. It allows to represent the electromagnetic field, which is a member of $\mathcal{H}(\nabla\times)$, with a more regular field A, which is in $\mathcal{H}(\nabla\cdot)\cap\mathcal{H}(\nabla\times)$. The singularity is contained in the term $\nabla\left(\frac{\nabla\cdot A}{\hat{\sigma}\mu}\right)$.

5. A difficulty in obtaining a weak form of the governing equation for the vector potential representation of the electric field E

To be able to use the finite element method for a calculation of the EM field, a weak form of a governing equation satisfied by the electric Schelkunoff potential is needed.

In order to obtain a weak equation, one starts from Maxwell's equations (1). Dividing the first equation by $-i\omega\mu$, taking curl and substituting into the second equation, one obtains

$$\nabla \times \frac{1}{-i\omega\mu}\nabla \times E - \hat{\sigma}E = J^{imp} \tag{23}$$

Next $-i\omega A + \nabla\left(\frac{\nabla\cdot A}{\hat{\sigma}\mu}\right)$ is substituted for E and the equation is multiplied by a test vector field K. The result is

$$\int_\Omega \left(\nabla \times \frac{1}{\mu}\nabla \times A\right)\cdot K - \int_\Omega \nabla\left(\frac{\nabla\cdot A}{\hat{\sigma}\mu}\right)\cdot(\hat{\sigma}K) + \int_\Omega i\omega\hat{\sigma}A\cdot K = \int_\Omega J^{imp}\cdot K$$

In order to integrate by parts the first term in the above equation, one uses continuity of the tangential component of $\frac{1}{\mu}\nabla\times A$, which is equivalent to continuity of the tangential component of the magnetic field H and one needs the tangential components of K to be continuous across interfaces (like the interface $\partial V_1 \cap \partial V_2$ considered in section 4).

On the other hand, in order to integrate by parts the second term, one would use a continuity of $\frac{\nabla\cdot A}{\hat{\sigma}\mu}$, and one needs the normal components of $\hat{\sigma}K$ to be continuous across interfaces. So if $\hat{\sigma}$ is discontinuous, so is the normal component of K. This is the essence of the problem in obtaining a proper weak form of the equation for A. A family of vector finite element shape functions with continuous tangential components and normal components experiencing specific jumps is difficult to build. One may consider a mixed formulation involving scalar and vector potentials (see section 6), but that increases the number of coefficients needed to represent the field.

It turns out that, assuming that μ is constant, it is possible to obtain an equation involving only the vector potential, but for a vector potential representation of the magnetic field H. This idea is presented in section 7.

6. A formulation with both scalar and vector potentials

If the original field is not divergence free, an equation involving both scalar and vector components must be considered. Although the number of coefficients per point in space increases from 3 to 4, the obtained equation is valid for non-constant electromagnetic properties and a non divergence free field. Also, if the boundary of the domain Ω is connected, a sesquilinear form of the equation remains coercive as $\omega = 0$.

In [9], in the case of the Lorenz gauge #2, the authors proved the uniqueness of the Schelkunoff potential given as a solution of an equation (see (58) in [9]) that has the following bilinear form in the left hand side:

$$\begin{aligned}\mathcal{G}\left((A,\rho),\,(K,\psi)\right) \quad &= \textstyle\int_\Omega [\nabla\times A\cdot\frac{1}{\mu}\nabla\times K + \nabla\cdot A\frac{1}{\mu}\nabla\cdot K - \omega^2\epsilon A\cdot K \\ &\quad -i\omega\epsilon\nabla\cdot\psi A + \epsilon\nabla\rho\cdot\nabla\psi - \omega^2\epsilon^2\mu\rho\psi - i\omega\epsilon\nabla\cdot\rho K]\end{aligned}$$

This bilinear form, considered for a purely imaginary frequency $\omega = i\tilde{\omega},\ \tilde{\omega} > 0$, may be rewritten as

$$\mathcal{G} = \int_\Omega \frac{1}{\mu}(\nabla\cdot A+\mu\tilde{\omega}\epsilon\rho)(\nabla\cdot K+\mu\tilde{\omega}\epsilon\psi)+\int_\Omega \epsilon(\tilde{\omega}A+\nabla\rho)\cdot(\tilde{\omega}K+\nabla\psi)+\int_\Omega \frac{1}{\mu}(\nabla\times A)\cdot(\nabla\times K)$$

Using this form we can prove the boundedness and the coercivity of $\mathcal{G}$ for $A,\ K \in \mathcal{H}_0(\nabla\times,\Omega)\cap\mathcal{H}(\nabla\cdot,\Omega),\ \rho,\psi \in \mathcal{H}_0^1(\Omega)$. So from the Lax-Milgram theorem, there exists a unique solution to the equation for the Lorenz gauged vector and scalar potentials that is considered in [9]. This formulation may be adapted to a lossy medium, which is expressed in Theorem 6.1.

Theorem 6.1. *Let the assumptions (19) be satisfied. The unique electric Schelkunoff potential A, together with a scalar field*

$$\phi = \frac{\nabla\cdot A}{\sqrt{\omega}\hat{\sigma}\mu} \tag{24}$$

satisfy the following equation

$$\begin{aligned}\int_\Omega \tfrac{1}{\mu}(\nabla\times A)\cdot\overline{(\nabla\times K)} + \int_\Omega \tfrac{1}{\mu}(\nabla\cdot A-\sqrt{\omega}\mu\hat{\sigma}\phi)\overline{(\nabla\cdot K-\sqrt{\omega}\mu\hat{\sigma}\psi)}\\ +i\int_\Omega \hat{\sigma}(\sqrt{\omega}A+i\nabla\phi)\cdot\overline{(\sqrt{\omega}K+i\nabla\psi)} = \int_\Omega J^{imp}\cdot\overline{(K+i\tfrac{\nabla\psi}{\sqrt{\omega}})}\end{aligned} \tag{25}$$

$$\forall K \in \mathcal{H}_0(\nabla\times)\cap\mathcal{H}(\nabla\cdot) \text{ and } \psi \in \mathcal{H}_0^1$$

$$A \in \mathcal{H}(\nabla\times)\cap\mathcal{H}(\nabla\cdot), \qquad n\times(-i\omega A) = n\times E \text{ on } \partial\Omega,\ \phi \in \mathcal{H}_0^1. \tag{26}$$

The sesquilinear form associated with equation (25) is bounded and coercive with respect to the norm

$$\|(K,\psi)\|_{\mathcal{B}} = \sqrt{\|K\|_0^2+\|\nabla\times K\|_0^2+\|\nabla\cdot K\|_0^2+\|\nabla\psi\|_0^2+\|\psi\|_0^2} \tag{27}$$

Hence if $J^{imp} \in (L^2)^3$, then the solution to this equation exists and is unique.

Remark 6.2.

- *If the domain is a convex polygon, or if the domain has C^2 boundary, then one may use nodal shape functions to approximate both A and ϕ.*
- *In order to obtain the electric field E, one has to calculate*

$$E = -i\omega A + \sqrt{\omega}\nabla\phi \tag{28}$$

- *If one drops all the terms multiplied by ω, the resulting sesquilinear form remains coercive. To prove this, one has to use the Poincare inequality for $H_0(\nabla\times)\cap\mathcal{H}(\nabla\cdot)$ (see* [1]*, Corollary 3.19). The proof of this result is easier than the proof of coercivity of the original sesquilinear form, so it is omitted.*
- *In* [15]*, the authors present a similar equation to ours. In our formulation, we apply a scaling $\frac{1}{\sqrt{w}}$ on the scalar function φ. As a result our sesquilinear form remains coercive for $\omega = 0$. Instead of $\frac{1}{\mu}$, one can consider an arbitrary weight in the middle term of the sesquilinear form, the term containing the divergences. The authors of* [15] *denoted this weight by $\frac{1}{\mu_*}$ and their proof of the coercivity of the sesquilinear form depends on the smallness of the upper bound of μ_*. The proof we present is not dependent on such a bound, thus is valid as long as μ_* is bounded away from 0 and from ∞. Also in our formulation and in the proof, we consider the case of non zero ϵ and an arbitrarily large frequency ω, thus an arbitrarily large term $i\omega\epsilon$.*

Proof. The fact that the vector potential A of Corollary 3.3 and ϕ defined in (24) satisfy equation (25) is straightforward and is explained as follows. A consequence of (24) is that the middle term on the right hand side of (25) vanishes. The definition of ϕ implies (28). If (28) is used, then equation (25) simplifies to

$$\int_\Omega \frac{1}{\mu}(\nabla\times E)\cdot\overline{(\nabla\times K)} + i\omega\int_\Omega \hat\sigma E\cdot\overline{\left(K+i\frac{\nabla\psi}{\sqrt{\omega}}\right)} = -i\omega\int_\Omega J^{imp}\cdot\overline{\left(K+i\frac{\nabla\psi}{\sqrt{\omega}}\right)}$$

Since $K\in\mathcal{H}_0(\nabla\times)\cap\mathcal{H}(\nabla\cdot)$ and $\psi\in\mathcal{H}_0^1$, then $\tilde K = \overline{K+i\frac{\nabla\psi}{\sqrt{\omega}}}\in\mathcal{H}_0(\nabla\times)$ and $\nabla\times\tilde K = \nabla\times\overline{K}$, so it remains to show that for any $\tilde K\in\mathcal{H}_0(\nabla\times)$ the following equation is satisfied:

$$\int_\Omega \frac{1}{\mu}(\nabla\times E)\cdot(\nabla\times\tilde K) + i\omega\int_\Omega \hat\sigma E\cdot\tilde K = -i\omega\int_\Omega J^{imp}\cdot\tilde K$$

This is a standard equation satisfied by the electric field E which satisfy Maxwell's equations (1). The equation is satisfied for all $\tilde K\in\mathcal{H}_0(\nabla\times)$. This concludes the proof that A and ϕ defined in (24) satisfy equation (25).

Let us now focus on a proof of the boundedness and the coercivity of the sesquilinear form $\mathcal{B}((A,\phi),(K,\psi))$ defined as the left hand side of the equation (25).

Denote $\hat\sigma_M = (\sigma_M+\omega\epsilon_M)$. The boundedness of $\mathcal{B}$ is straightforward, as from the Cauchy-Schwartz inequality, it follows that:

$$\begin{aligned}
&|\mathcal{B}((A,\phi),(K,\psi))| = \\
&= \left|\int_\Omega \frac{1}{\mu}(\nabla\times A)\cdot\overline{(\nabla\times K)} + \int_\Omega \frac{1}{\mu}(\nabla\cdot A-\sqrt{\omega}\mu\hat\sigma\phi)\overline{(\nabla\cdot K-\sqrt{\omega}\mu\hat\sigma\psi)}\right. \\
&\qquad\left. +i\int_\Omega \hat\sigma(\sqrt{\omega}A+i\nabla\phi)\cdot\overline{(\sqrt{\omega}K+i\nabla\psi)}\right| \\
&\le \frac{1}{\mu_m}\int_\Omega |\nabla\times A|\,|\nabla\times K| + \int_\Omega \frac{1}{\mu_m}|\nabla\cdot A-\sqrt{\omega}\mu\hat\sigma\phi|\,|\nabla\cdot K-\sqrt{\omega}\mu\hat\sigma\psi| \\
&\qquad + \int_\Omega \hat\sigma_M|\sqrt{\omega}A+i\nabla\phi|\,|\sqrt{\omega}K+i\nabla\psi| \\
&\le \frac{1}{\mu_m}\|\nabla\times A\|_0\|\nabla\times K\|_0 + \frac{1}{\mu_m}\|\nabla\cdot A-\sqrt{\omega}\mu\hat\sigma\phi\|_0\|\nabla\cdot K-\sqrt{\omega}\mu\hat\sigma\psi\|_0 \\
&\qquad + \hat\sigma_M\|\sqrt{\omega}A+i\nabla\phi\|_0\|\sqrt{\omega}K+i\nabla\psi\|_0 \\
&\le \frac{1}{\mu_m}\|\nabla\times A\|_0\|\nabla\times K\|_0 + \frac{1}{\mu_m}(\|\nabla\cdot A\|_0+\sqrt{\omega}\mu_M\hat\sigma_M\|\phi\|_0)\,(\|\nabla\cdot K\|_0+\sqrt{\omega}\mu_M\hat\sigma_M\|\psi\|_0) \\
&\qquad + \hat\sigma_M(\sqrt{\omega}\|A\|_0+\|\nabla\phi\|_0)\,(\sqrt{\omega}\|K\|_0+\|\nabla\psi\|_0) \\
&\le \max\left(\frac{1}{\mu_m},\frac{\sqrt{\omega}\mu_M}{\mu_m}\hat\sigma_M,\frac{\omega\mu_M^2}{\mu_m}\hat\sigma_M^2,\hat\sigma_M,\hat\sigma_M\sqrt{\omega},\hat\sigma_M\omega\right)\|(A,\phi)\|_{\mathcal{B}}\|(K,\psi)\|_{\mathcal{B}}
\end{aligned}$$

To prove the coercivity, we have to prove that there exists a constant $d>0$ such that for any $(K,\psi)\in(\mathcal{H}_0(\nabla\times,\Omega)\cap\mathcal{H}(\nabla\cdot,\Omega))\times\mathcal{H}_0^1(\Omega)$

$$|\mathcal{B}((K,\psi),(K,\psi))|\ge d\|(K,\psi)\|_{\mathcal{B}}^2$$

It is enough to prove that it is not possible to have a sequence of $(K_n,\psi_n)_{n=1}^\infty$ such that

$$\begin{aligned}
1 &= \|(K_n,\psi_n)\|_{\mathcal{B}}^2 \\
&= \|K_n\|_0^2+\|\nabla\times K_n\|_0^2+\|\nabla\cdot K_n\|_0^2+\|\nabla\psi_n\|_0^2+\|\psi_n\|_0^2 \qquad (29)
\end{aligned}$$

and

$$\mathcal{B}((K_n,\psi_n),(K_n,\psi_n))\xrightarrow[n\to\infty]{}0 \qquad (30)$$

For a proof by contradiction, assume that there is a sequence (K_n, ψ_n) satisfying (29) and (30). We will prove that there is a subsequence of (K_n, ϕ_n) convergent to 0 in $\|.\|_{\mathcal{B}}$. Using the compact embedding of $\mathcal{H}_0(\nabla\times) \cap \mathcal{H}(\nabla\cdot)$ in $(L^2)^3$ (Maxwell's compactness property, [25]) and the compact embedding of H_0^1 in L^2 (Rellich's theorem), there is a subsequence (K_{n_k}, ψ_{n_k}) convergent to (K, ψ) in $(L^2)^4$. To simplify the notation we will write n instead of n_k, thus replacing the original sequence with its subsequence. We obtain that

$$\|K_n - K\|_0 \xrightarrow[n\to\infty]{} 0 \tag{31}$$

$$\|\psi_n - \psi\|_0 \xrightarrow[n\to\infty]{} 0 \tag{32}$$

We will prove that K_n converges to K in $\mathcal{H}_0(\nabla\times) \cap \mathcal{H}(\nabla\cdot)$, ψ_n converges to ψ in H_0^1, and that $\psi = 0$ and $K = 0$.

Consider the imaginary part of $\mathcal{B}((K_n, \psi_n), (K_n, \psi_n))$. Using the fact that $\hat{\sigma} = \sigma + i\omega\epsilon$, we obtain:

$$\mathrm{Im}[\mathcal{B}((K_n, \psi_n), (K_n, \psi_n))] = \int_\Omega \sigma |\sqrt{\omega} K_n + i\nabla\psi_n|^2 \xrightarrow[n\to\infty]{} 0 \tag{33}$$

Similarly, taking the real part, we have:

$$\mathrm{Re}[\mathcal{B}((K_n, \psi_n), (K_n, \psi_n))] =$$
$$\int_\Omega \frac{1}{\mu} |\nabla \times K_n|^2 + \int_\Omega \frac{1}{\mu} |\nabla \cdot K_n - \sqrt{\omega}\mu\hat{\sigma}\psi_n|^2 - \int_\Omega \omega\epsilon |\sqrt{\omega} K_n + i\nabla\psi_n|^2$$

Using (33) and the bounds (19) for σ and ϵ, we conclude that the third term in the above approaches 0. As the remaining two terms are nonnegative, we conclude that:

$$\int_\Omega \frac{1}{\mu} |\nabla \times K_n|^2 \xrightarrow[n\to\infty]{} 0 \tag{34}$$

$$\int_\Omega \frac{1}{\mu} |\nabla \cdot K_n - \sqrt{\omega}\mu\hat{\sigma}\psi_n|^2 \xrightarrow[n\to\infty]{} 0 \tag{35}$$

Using the bounds (19) on σ and μ, we conclude that (33), (34), (35) imply:

$$\|\sqrt{\omega} K_n + i\nabla\psi_n\|_0 \xrightarrow[n\to\infty]{} 0 \tag{36}$$

$$\|\nabla \times K_n\|_0^2 \xrightarrow[n\to\infty]{} 0 \tag{37}$$

$$\|\nabla \cdot K_n - \sqrt{\omega}\mu\hat{\sigma}\psi_n\|_0^2 \xrightarrow[n\to\infty]{} 0 \tag{38}$$

Taking any smooth vector field Z with a compact support in Ω, $Z \in (\mathcal{C}_c^\infty(\Omega))^3$, using (31) and (36), we obtain:

$$\left| \langle i\nabla\psi, Z\rangle + \int_\Omega \sqrt{w} K \cdot \overline{Z} \right| = \left| - \int_\Omega i\psi(\nabla \cdot \overline{Z}) + \int_\Omega \sqrt{w} K \cdot \overline{Z} \right|$$
$$\leq \left| \int_\Omega i(\psi_n - \psi)(\nabla \cdot \overline{Z}) + \int_\Omega (i\nabla\psi_n + \sqrt{w} K_n) \cdot \overline{Z} + \int_\Omega \sqrt{w}(K - K_n) \cdot \overline{Z} \right|$$
$$\leq \|\psi_n - \psi\|_0 \|\nabla \cdot Z\|_0 + \|i\nabla\psi_n + \sqrt{w} K_n\|_0 \|Z\|_0 + \sqrt{w}\|K - K_n\|_0 \|Z\|_0 \xrightarrow[n\to\infty]{} 0$$

which implies that

$$i\nabla\psi = -\sqrt{\omega} K \in (L^2)^3 \tag{39}$$

Moreover as a consequence of (31) and (36)

$$\begin{aligned} &\|\nabla\psi_n - \nabla\psi\|_0 = \|i\nabla\psi_n - i\nabla\psi\|_0 \\ &\leq \|\sqrt{\omega}K - \sqrt{\omega}K_n\|_0 + \|\sqrt{w}K_n + i\nabla\psi_n\|_0 \xrightarrow[n\to\infty]{} 0 \end{aligned} \tag{40}$$

Thus ψ_n converges to ψ in $\|.\|_1$, and as $\psi_n \in \mathcal{H}_0^1$ and $\mathcal{H}_0^1$ is a closed subspace of $\mathcal{H}^1$, then $\psi \in \mathcal{H}_0^1$.

Similarly, taking any $Z \in (\mathcal{C}_c^\infty(\Omega))^3$, using (31) and (37), we obtain

$$\begin{aligned} &|\langle \nabla \times K, Z\rangle| = |\langle \nabla \times (K - K_n), Z\rangle + \langle \nabla \times K_n, Z\rangle| \\ &= \left|\int_\Omega (K - K_n)\cdot(\nabla \times \overline{Z}) + \int_\Omega (\nabla \times K_n)\cdot \overline{Z}\right| \\ &\leq \|K - K_n\|_0 \|\nabla \times Z\|_0 + \|\nabla \times K_n\|_0 \|Z\|_0 \xrightarrow[n\to\infty]{} 0 \end{aligned} \tag{41}$$

Thus $\nabla \times K = 0$. This, together with (37) implies that

$$\|\nabla \times K - \nabla \times K_n\|_0 = \|\nabla \times K_n\|_0 \xrightarrow[n\to\infty]{} 0 \tag{42}$$

In a similar way, using (38) and (32) one shows that

$$\nabla \cdot K = \sqrt{\omega}\mu\hat{\sigma}\psi \in L^2 \tag{43}$$

$$\|\nabla \cdot K_n - \nabla \cdot K\|_0 \xrightarrow[n\to\infty]{} 0 \tag{44}$$

We have proven that (K_n, ψ_n) converges to (K, ψ) in $\|.\|_{\mathcal{B}}$. To prove that $K = 0$ and $\psi = 0$, notice that (43) and (39) imply

$$-\nabla \cdot \nabla\psi + i\omega\mu\hat{\sigma}\psi = 0 \tag{45}$$

which rewritten in a weak form says:

$$\int_\Omega \nabla\psi \cdot \nabla\overline{\nu} - \int_\Omega (-i\omega\mu\hat{\sigma})\psi\overline{\nu} = 0 \tag{46}$$

for any test function $\nu \in \mathcal{H}_0^1$. The sesquilinear form of this equation is a bounded and coercive sesquilinear form, which has been shown in the proof of Theorem 3.1 for $\gamma = -i\omega\mu\hat{\sigma}$. Thus from the Lax-Milgram theorem the equation admits a unique solution $\psi = 0$. This and (39) imply $K = 0$. We have obtained a contradiction with (29). Hence the sesquilinear form $\mathcal{B}$ is coercive.

If $J^{imp} \in (L^2)^3$, then the right hand side of (25) is a bounded linear functional on the space $(\mathcal{H}_0(\nabla\times) \cap \mathcal{H}(\nabla\cdot)) \times \mathcal{H}_0^1$ with the norm $\|.\|_{\mathcal{B}}$, thus from the Lax-Milgram theorem, there exists a unique solution to equation (25). □

The vector-scalar formulation of Theorem 6.1 forms a basis for a general finite element simulation scheme for non divergence-free EM fields.

7. A representation of the magnetic field H

If the original field is divergence-free, a simpler weak equation involving only the vector potential may be obtained. This approach is presented for a representation of the magnetic field H. This representation is mentioned in [37],

$$H = F - \nabla\left(\frac{\nabla \cdot F}{i\omega\hat{\sigma}\mu}\right) \tag{47}$$

Existence of this representation follows from Theorem 3.1 if assumptions (19) are satisfied. Although in a geophysical setting it cannot be assumed that the conductivity is constant, most of the rocks have magnetic permeability $\mu = \mu_0$. In this case the magnetic field H is divergence free:

$$\nabla \cdot H = 0$$

In this situation, the vector potential for which $\frac{\nabla \cdot F}{i\omega\hat{\sigma}\mu} = 0$ on $\partial\Omega$, coincides with the magnetic field:

$$F = H$$

We start with the standard curl-curl equation for the magnetic field H:

$$\int_\Omega \frac{1}{\hat{\sigma}}(\nabla \times H) \cdot (\overline{\nabla \times K}) + i\omega \int_\Omega \mu_0 H \cdot \overline{K} = \int_\Omega \frac{1}{\hat{\sigma}} J^{imp} \cdot (\overline{\nabla \times K}) \tag{48}$$

Substitution of $\left(H - \nabla\left(\frac{\nabla \cdot H}{i\omega\hat{\sigma}\mu}\right)\right)$ instead of H, results in the equation presented below:

$$\begin{aligned} \int_\Omega \frac{1}{\hat{\sigma}}(\nabla \times H) \cdot (\overline{\nabla \times K}) + \int_\Omega \frac{1}{\hat{\sigma}}(\nabla \cdot H)(\overline{\nabla \cdot K}) + i\omega \int_\Omega \mu_0 H \cdot \overline{K} \\ = \int_\Omega \frac{1}{\hat{\sigma}} J^{imp} \cdot (\overline{\nabla \times K}) \end{aligned} \tag{49}$$

$$\forall\ K \in \mathcal{H}(\nabla\times) \cap \mathcal{H}(\nabla\cdot),\quad n \times K|_{\partial\Omega} = 0$$

$$H \in \mathcal{H}(\nabla\times) \cap \mathcal{H}(\nabla\cdot),\quad n \times H|_{\partial\Omega} = n \times \hat{H}|_{\partial\Omega}$$

where $n \times \hat{H}$ denote tangential boundary values for H.

The sesquilinear form of this equation for $\hat{\sigma} \in \mathbb{R}$ and $0 < \sigma_m \leq \hat{\sigma} \leq \sigma_M < \infty$ is coercive and bounded with respect to the norm

$$\|K\|_{\nabla\cdot,\nabla\times} = \sqrt{\|\nabla \times K\|_0^2 + \|\nabla \cdot K\|_0^2 + \|K\|_0^2}$$

So the equation admits a unique solution, which is the magnetic field H.

The advantage of the equation (49) is that the sesquilinear form is coercive, even if the term $i\omega \int_\Omega \mu_0 H \cdot K$ is not present, as long as the boundary of the domain Ω is connected. This situation happens when the frequency $w = 0$. As a result the system matrix is well conditioned for small frequencies. If there is a jump in conductivity, the condition number of the system matrix increases, yet the situation is similar to the case of a discontinuous coefficient in the Poisson equation. Even for a high contrast in conductivity, it should be sufficient to use standard vector multigrid preconditioners [35] for an iterative solver to converge.

This kind of regularization has been studied in the literature (see [1, 13]) without introducing the notion of the Schelkunoff potential. Indeed, if the original field is divergence free, then the Schelkunoff potential of Theorem 3.1 coincides with the original field. An interesting eigenvalue analysis for the equation with and without the divergence term is presented in [30].

In geophysical applications a computational domain is usually a convex polygon (in magnetotellurics it is a cuboid). In this situation $(\mathcal{H}^1)^3 \cap \mathcal{H}_0(\nabla\times)$ is dense in $\mathcal{H}(\nabla\cdot) \cap \mathcal{H}_0(\nabla\times)$, so the use of the nodal shape functions leads to a convergent discretization. Caution is needed when applying this method to other problems as $(\mathcal{H}^1)^3 \cap \mathcal{H}_0(\nabla\times)$ is not always dense in $\mathcal{H}(\nabla\cdot) \cap \mathcal{H}_0(\nabla\times)$ (see [13] or Appendix B in [6]). In application to magnetotellurics, numerical tests involving equation (49) are presented in section 8.

8. Numerical results

In this section, the magnetic field H for a plane-wave (magnetotelluric) source is calculated using equation (49) and compared with a field calculated by an independent integral equation code of [36].

The considered model is a conductive brick of resistivity $1\Omega m$ and dimensions 1km x 2km x 2km in the whole space of resistivity $100\Omega m$. The field is calculated

500m above the brick, along a line going in the y-direction. The second order nodal shape functions for a hexahedral mesh (Q2) are used for each component of the field. A sketch of the model and the hexahedral mesh is presented in Figure 2.

The solution H is approximated by

$$H = \sum_{j=1}^{n} x_j N_j \tag{50}$$

where n is the number of degrees of freedom, N_j are shape functions. Inserting (50) into equation (49) gives

$$\begin{aligned}\int_\Omega \tfrac{1}{\hat\sigma}\left(\nabla \times \textstyle\sum_{j=1}^n x_j N_j\right)\cdot(\nabla\times N_k) + \int_\Omega \tfrac{1}{\hat\sigma}\left(\nabla\cdot\textstyle\sum_{j=1}^n x_j N_j\right)(\nabla\cdot N_k)\\ +i\omega\int_\Omega \mu_0 \textstyle\sum_{j=1}^n x_j N_j\cdot N_k = \int_\Omega \tfrac{1}{\hat\sigma} J^{imp}(\nabla\times N_k)\end{aligned}$$

which produces a linear system $Ax = b$ to be solved, where

$$A_{kj} = \int_\Omega \frac{1}{\hat\sigma}(\nabla\times N_j)\cdot(\nabla\times N_k) + \int_\Omega \frac{1}{\hat\sigma}(\nabla\cdot N_j)(\nabla\cdot N_k) + i\omega\int_\Omega \mu_0 N_j\cdot N_k$$

$$b_k = \int_\Omega \frac{1}{\hat\sigma} J^{imp}\cdot(\nabla\times N_k)$$

The total field generated by a plane wave in the whole space with the brick, is decomposed into a primary electromagnetic field (H_p, E_p) and a secondary electromagnetic field (H_s, E_s)

$$H_t = H_p + H_s, \quad E_t = E_p + E_s$$

The primary field is a plane wave traveling in increasing z direction in the 100Ωm whole space with H field purely in the y direction. The secondary field is the change of the field due to the presence of the brick. The code solves for the secondary field H_s, with $n\times H_s = 0$ on $\partial\Omega$. It is assumed that $\sigma = \sigma_t$ is the conductivity of a conducting brick in a whole-space, with the source $J^{imp} = E_p\sigma_s$, where $\sigma_s = \sigma_t - \sigma_p$ is the difference between the conductivity of the whole-space with the conducting brick and the conductivity of the whole space. Two frequencies were considered: 0.001Hz and 10Hz. The mesh consisted of 15x15x20 hexahedral elements and extended more than 20km from the brick. The inner part of the mesh is presented in Figure 2. The linear system had $98,397$ unknowns. QMR with incomplete LU preconditioner converged to the relative residual norm of 10^{-7} in 28 iterations for the frequency 10Hz and in 54 iterations for 0.001Hz.

Figure 3 presents a ratio of the secondary field to the primary field. The fields calculated by an Integral Equation code [36] and FEM code that uses (49), are similar for both frequencies. The proposed method gives proper values of the magnetic field H.

Acknowledgments

We acknowledge the support of this work from the U.S. Dept. of Energy under contract DE-EE0002750 to PW. EC acknowledges the partial support of the U.S. National Science Foundation through grants ARC-0934721 and DMS-1413454. We would like to thank the reviewers for many helpful comments. We are especially grateful to one of the referees for a suggestion that allowed us to generalize the results to any positive frequency.

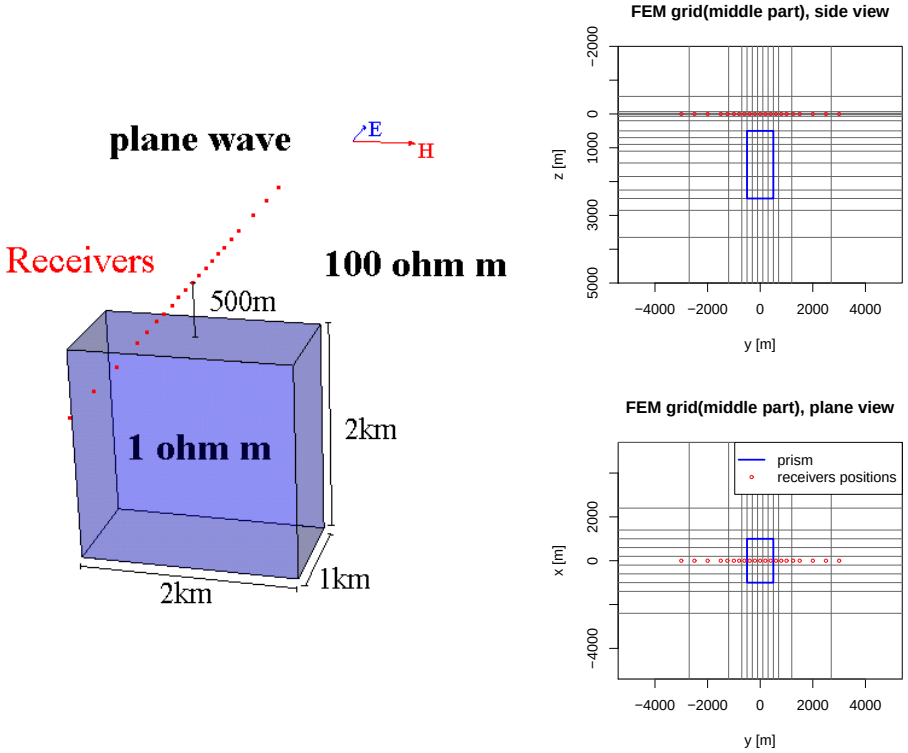

FIGURE 2. Sketch of a considered model for numerical simulation(left); Hexahedral mesh cross-sections(right).

9. Appendix

Three vector identities are used. For $K, L : \mathbb{R}^3 \to \mathbb{C}^3, u : \mathbb{R}^3 \to \mathbb{C}$, which are at least $\mathcal{C}^2$ regular in $\overline{\Omega}$, we have:

$$\nabla \times \nabla \times K = \nabla(\nabla \cdot K) - \nabla \cdot (\nabla K) \tag{51}$$

$$\int_\Omega (\nabla \times K) \cdot L = \int_\Omega K \cdot (\nabla \times L) + \int_{\partial\Omega} (n \times K) \cdot L \tag{52}$$

$$\int_\Omega \nabla u \cdot K = -\int_\Omega u \nabla \cdot K + \int_{\partial\Omega} u(K \cdot n) \tag{53}$$

References

[1] C. Amrouche, C. Bernardi, M. Dauge and V. Girault, Vector potentials in three-dimensional nonsmooth domains, Mathematical Methods in the Applied Sciences, 21 (1998) 823–864.
[2] D. Arnold, R. Falk and R. Winther, Multigrid in H(div) and H(curl), Numer. Math., 85 (2000) 197–217.
[3] D. Avdeev and A. Avdeeva, 3D magnetotelluric inversion using a limited-memory quasi-Newton optimization, Geophysics, 74 (2009) F45–F57.
[4] A. Bermúdez, R. Rodríguez and P. Salgado, Numerical analysis of electric field formulations of the eddy current model, Numer. Math., 102 (2005) 181–201.

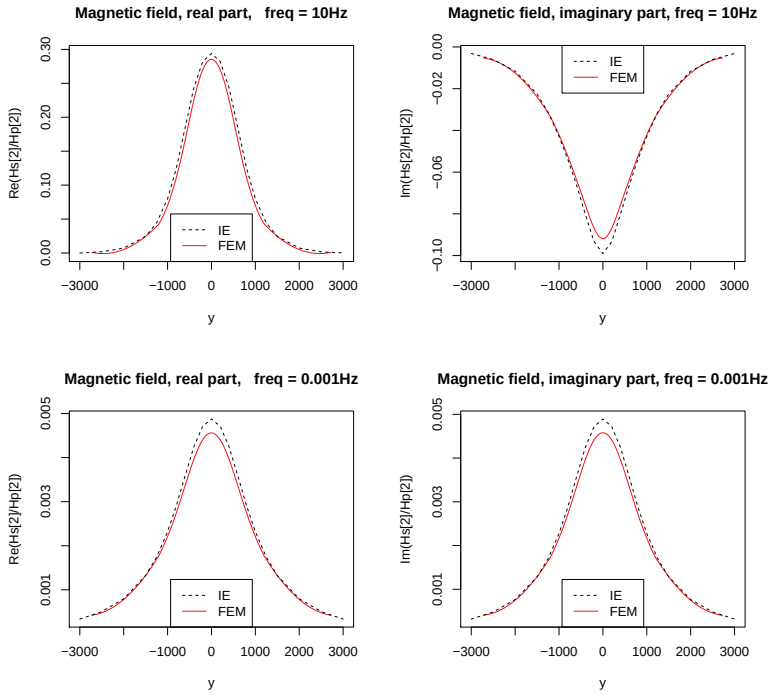

FIGURE 3. Ratio of the secondary field to the primary field for frequency 10Hz(top) and for frequency 0.001Hz(bottom).

[5] A. Bermúdez, R. Rodríguez and P. Salgado, Numerical solution of eddy current problems in bounded domains using realistic boundary conditions, Computer Methods in Applied Mechanics and Engineering, 194 (2005) 411–426.

[6] P. B. Bochev and M. D. Gunzburger, Least-Squares Finite Element Methods, Springer New York, 2009.

[7] R.-U. Boerner, Numerical modelling in geo-electromagnetics: advances and challenges, Surv. Geophys., 31 (2010) 225–245.

[8] A. Bossavit, On the Lorenz gauge, COMPEL - the International Journal for Computation and Mathematics in Electrical and Electronic Engineering, 18 (1999) 323–336.

[9] W. E. Boyse, D. R. Lynch, K. D. Paulsen and G. N. Minerbo, Nodal-based finite-element modeling of Maxwell's equations, IEEE Transactions on Antennas and Propagation, 40 (1992) 642–651.

[10] C. F. Bryant, C. R. I. Emson and C. W. Trowbridge, Comparison of Lorentz gauge formulations in eddy current computations, IEEE Transactions on Magnetics, 26 (1990) 430–433.

[11] M. Commer, and G. A. Newman, New advances in three-dimensional controlled-source electromagnetic inversion, Geophys. J. Int., 172 (2008) 513–535.

[12] M. Costabel, M. Dauge and S. Nicaise, Singularities of Maxwell interface problems, ESAIM: Mathematical Modelling and Numerical Analysis, 33 (1999) 627–649.

[13] A.-S. B.-B. Dhia, C. Hazard and S. Lohrengel, A singular field method for the solution of Maxwell's equations in polyhedral domains, SIAM Journal on Applied Mathematics, 59 (1999) 2028–2044.

[14] C. G Farquharson, D. W. Oldenburg, E. Haber and R. Shekhtman, An algorithm for the three-dimensional inversion of magnetotelluric data, In 72st Ann. Internat. Mtg., Soc. Expl. Geophys, (2002) pp. 649–652.

[15] P. Fernandes and A. Valli, Lorenz-gauged vector potential formulations for the time-harmonic eddy-current problem with L^∞- regularity of material properties, Math. Methods Appl. Sci., 31 (2008) 71–98.

[16] E. Haber, D. Oldenburg and R. Shekhtman, Inversion of time-domain three-dimensional data, Geophys. J. Int., 171 (2007) 550–564.
[17] R. Hiptmair, Multigrid method for Maxwell's equations, SIAM Journal on Numerical Analysis, 36 (1998) 204–225.
[18] R. Hiptmair, Finite elements in computational electromagnetism, Acta Numerica, 11 (2002) 237–339.
[19] R. Hiptmair, Analysis of multilevel methods for eddy current problems, Mathematics of Computation, 72 (2003) 1281–1303.
[20] Y. Huang, J. Li, and Y. Lin, Finite element analysis of Maxwell's equations in dispersive lossy bi-isotropic media, Adv. Appl. Math. Mech., 5 (2013) 494–509.
[21] T. V. Kolev and P. S. Vassilevski, Some experience with a H1-based auxiliary space AMG for H(curl) problems, Lawrence Livermore National Laboratory, Technical report UCRL-TR-221841, Livermore, CA. (2006).
[22] W. Li, D. Liang, and Y. Lin, A new energy-conserved S-FDTD scheme for Maxwell's equations in metamaterials, Int. J. Numer. Anal. Model., 10 (2013) 775–794.
[23] R. L. Mackie, J. T. Smith and T. R. Madden, Three-dimensional electromagnetic modeling using finite difference equations: The magnetotelluric example, Radio Science, 29 (1994) 923–935.
[24] J. C. Nedelec, Mixed finite elements in $\mathbb{R}^3$, Numer. Math., 35 (1980) 315–341.
[25] R. Picard, An elementary proof for a compact imbedding result in generalized electromagnetic theory, Mathematische Zeitschrift, 187 (1984) 151–164.
[26] W. Rodi, and R. L. Mackie, Nonlinear conjugate gradients algorithm for 2-D magnetotelluric inversion, Geophysics, 66 (2001) 174–187.
[27] A. A. Rodríguez, R. Hiptmair and A. Valli, Mixed finite element approximation of eddy current problems, IMA Journal of Numerical Analysis, 24 (2004) 255–271.
[28] A. A. Rodríguez, R. Hiptmair and A. Valli, A hybrid formulation of eddy current problems, Numerical Methods for Partial Differential Equations, 21 (2005) 742–763.
[29] Y. Saad, Iterative methods for sparse linear systems, SIAM, 2003.
[30] W. Shin and S. Fan, Accelerated solution of the frequency-domain Maxwell's equations by engineering the eigenvalue distribution of the operator, Optics Express, 21 (2013) 22578–22595.
[31] J. Smith, Conservative modeling of 3-D electromagnetic fields, Part II: Biconjugate gradient solution and an accelerator, Geophysics, 61 (1996) 1319–1324.
[32] O. Sterz, A. Hauser, and G. Wittum, Adaptive local multigrid methods for solving time-harmonic eddy-current problems, IEEE Transactions on Magnetics, 42 (2006) 309–318.
[33] E. S. Um, D. L. Alumbaugh and J. M. Harris, A Lorenz-gauged finite-element solution for transient CSEM modeling, In SEG Annual Meeting, 17-22 October, Denver, Colorado (2010).
[34] E. S. Um, J. M. Harris and D. L. Alumbaugh, An iterative finite element time-domain method for simulating three-dimensional electromagnetic diffusion in the earth, Geophys. J. Int., 190 (2012) 871–886.
[35] P. Vanek, J. Mandel, and M. Brezina, Algebraic multigrid by smoothed aggregation for second and fourth order elliptic problems, Computing, 56 (1996) 179–196.
[36] P. Wannamaker, G. Hohmann and W. SanFilipo, Electromagnetic modeling of three-dimensional bodies in layered earths using integral equations, Geophysics, 49 (1984) 60–74.
[37] S. Ward, and G. Hohmann, Electromagetic Theory for Geophysical Applications, Electromagnetic Methods in Applied Geophysics-Theory Volume I, chapter 4., 1988.
[38] J. Xu, The auxiliary space method and optimal multigrid preconditioning techniques for unstructured grids, Computing, 56 (1996) 215–235.
[39] J. Xu, L. Chen and R. H. Nochetto, Optimal multilevel methods for H(grad) H(curl) and H(div) systems on graded and unstructured grids. In multiscale, nonlinear and adaptive approximation, Springer Berlin Heidelberg, 2009.
[40] W. Zheng, Z. Chen and L. Wang, An adaptive finite element method for the H-ψ formulation of time-dependent eddy current problems, Numerische Mathematik, 103 (2006) 667–689.

Michal Kordy, Department of Mathematics, University of Utah, 155 S 1400 E JWB 233, Salt Lake City, UT 84112-0090 and Energy & Geoscience Institute, University of Utah, 423 Wakara Way, Suite 300, Salt Lake City, UT 84108, USA
E-mail: kordy@math.utah.edu

Elena Cherkaev, Department of Mathematics, University of Utah, 155 S 1400 E JWB 233, Salt Lake City, UT 84112-0090
E-mail: elena@math.utah.edu
URL: http://www.math.utah.edu/∼elena

Phil Wannamaker, Energy & Geoscience Institute, University of Utah, 423 Wakara Way, Suite 300, Salt Lake City, UT 84108, USA
E-mail: pewanna@egi.utah.edu
URL: http://egi.utah.edu/about/staff/phil-wannamaker.php

Geophysical Journal International

Geophys. J. Int. (2016) **204,** 94–110 doi: 10.1093/gji/ggv411

GJI Geomagnetism, rock magnetism and palaeomagnetism

3-dimensional magnetotelluric inversion including topography using deformed hexahedral edge finite elements and direct solvers parallelized on symmetric multiprocessor computers – Part II: direct data-space inverse solution

M. Kordy,[1,2] P. Wannamaker,[2] V. Maris,[2] E. Cherkaev[1] and G. Hill[3]

[1]*Department of Mathematics, University of Utah.,* 155 *S* 1400 *E Room* 233, *Salt Lake City, UT* 84112-0090, *USA. E-mail: kordy@math.utah.edu*
[2]*Energy and Geoscience Institute, University of Utah,* 423 *Wakara Way, Suite* 300, *Salt Lake City, UT* 84108, *USA*
[3]*Gateway Antarctica, University of Canterbury, Private Bag* 4800 *Christchurch* 8140 *and Antarctica Scientific Limited, Unit 5E/39 Taranaki Street Wellington* 6011

Accepted 2015 September 23. Received 2015 September 22; in original form 2014 November 3

SUMMARY

Following the creation described in Part I of a deformable edge finite-element simulator for 3-D magnetotelluric (MT) responses using direct solvers, in Part II we develop an algorithm named HexMT for 3-D regularized inversion of MT data including topography. Direct solvers parallelized on large-RAM, symmetric multiprocessor (SMP) workstations are used also for the Gauss–Newton model update. By exploiting the data-space approach, the computational cost of the model update becomes much less in both time and computer memory than the cost of the forward simulation. In order to regularize using the second norm of the gradient, we factor the matrix related to the regularization term and apply its inverse to the Jacobian, which is done using the MKL PARDISO library. For dense matrix multiplication and factorization related to the model update, we use the PLASMA library which shows very good scalability across processor cores. A synthetic test inversion using a simple hill model shows that including topography can be important; in this case depression of the electric field by the hill can cause false conductors at depth or mask the presence of resistive structure. With a simple model of two buried bricks, a uniform spatial weighting for the norm of model smoothing recovered more accurate locations for the tomographic images compared to weightings which were a function of parameter Jacobians. We implement joint inversion for static distortion matrices tested using the Dublin secret model 2, for which we are able to reduce nRMS to ∼1.1 while avoiding oscillatory convergence. Finally we test the code on field data by inverting full impedance and tipper MT responses collected around Mount St Helens in the Cascade volcanic chain. Among several prominent structures, the north–south trending, eruption-controlling shear zone is clearly imaged in the inversion.

Key words: Numerical solutions; Inverse theory; Electrical properties; Magnetotellurics; Volcanic arc processes; Explosive volcanism.

1 INTRODUCTION

In Part I (Kordy *et al.* 2015), we have shown that moderately large 3-D magnetotelluric (MT) models including topography can be simulated accurately in practical run-times using a direct solver on a single-box, server-class multicore workstation with large RAM. The deformable mesh approach allows us to avoid expending many rows of cells to define just the topography as is done typically with finite differences, and which even then may not escape local electric field distortion (e.g. Liu *et al.* 2009; Stark *et al.* 2013). The MKL PARDISO library is effective on this platform, showing an overall scalability of 15 on 24 cores. For a mesh with 176 cells in x-direction, 176 cells in y-direction and 70 cells in z-direction (176x 176y 70z), 2000 source vectors (corresponding to 400 MT sites) could be solved in 2.5 times the time required for factorization, with total time for both under 2.5 hr. Meshes comparable to that could simulate site arrays of similar size to the Earthscope MT Transportable Array of the U.S. Pacific Northwest using this parallelized direct solver (Meqbel *et al.* 2014).

Here in Part II, we also use direct solvers exclusively to create a 3-D regularized inversion algorithm for MT data including topography, which we name HexMT. Due to its good convergence

properties, we pursue a Gauss–Newton formulation for the nonlinear, iterative parameter update, as have others (deGroot-Hedlin & Constable 1990; Key & Constable 2011; Grayver *et al.* 2013; Oldenburg *et al.* 2013). The number of parameters usually is significantly greater than the number of data for tomographic-style, regularized inversion. As noted by Siripunvaraporn *et al.* (2005a), inverse formulations using fewer parameters than data may suffer from a dependence of solution upon parametrization. One may also expect some lack of fit to data to occur if parameters are not defined optimally. On the other hand, tomographic inversions for MT data sets of a few hundred sites may require a number of parameters of order one million (e.g. Meqbel *et al.* 2014). Direct factorization of the reduced Hessian matrix in the traditional model-space definition (e.g. deGroot-Hedlin & Constable 1990; Sasaki 2001; Usui 2015), even using parallelization across multicore (Maris & Wannamaker 2010), is not practical for that scale of parametrization. As a result, researchers have tended to retain iterative solvers for the model update whether cast as Gauss–Newton or otherwise (e.g. Commer & Newman 2008; Zhdanov *et al.* 2011; Grayver *et al.* 2013; Schwarzbach & Haber 2013).

An alternative is to investigate the data-space formulation for solving the Gauss–Newton model update (Parker 1994; Siripunvaraporn & Egbert 2000; Siripunvaraporn *et al.* 2005a). This approach reduces the size of the matrix that needs to be inverted from $N_m \times N_m$ to $N_d \times N_d$ (m = model parameters, d = data), while the solutions in theory are identical. Consider an MT survey of 400 sites with 20 frequencies (four per decade say) and 12 data per frequency (four complex impedance and two complex tipper elements). The total data set size would be 96 000. As we show, this turns out to be a very manageable size of matrix to invert using direct solvers, particularly as parallelized across multicore symmetric multiprocessor (SMP) computers. Matrices twice this size in fact are not impractical, allowing data sets of more sites, greater bandwidth, or finer frequency sampling, with a fairly arbitrary number of model parameters.

This paper sets out with a brief overview of both model- and data-space approaches to solving the Gauss–Newton model update. Attention is paid to the mechanics of solving stably the normal system equation for a model gradient regularization functional. Runtime and scalability of the model update solver is investigated for multicore using different sized trial models. At this point it appears that model update solution time will remain significantly smaller than forward simulation run-time across all models with moderately fine parameter discretization. The inversion code is tested on several models. These include a simple conductive brick below a hill to show the strength of effect that topography can have on inversion models assuming a flat surface. Subsequently we examine a multiprism test model used as a community standard (Miensopust *et al.* 2013) and experiment with various regularization weighting schemes. Finally, we invert an extensive MT data set acquired over the volcano Mount St Helens (Hill *et al.* 2009) to show performance for a model where parameter number approaches one million.

2 FORWARD PROBLEM

The forward problem is described in detail by Kordy *et al.* (2015), touched on briefly here to define terms. We consider the MT problem in a domain Ω that includes the air and earth's subsurface. The Earth's surface is allowed to have topography. In order to calculate the MT response due to an arbitrary 3-D conductivity structure $\sigma = \sigma(x, y, z)$ we consider a hexahedral edge finite-element discretization of the equation for the secondary electric field E:

$$\int_\Omega \frac{1}{\mu}\nabla\times E\cdot\nabla\times M + \mathrm{i}\omega\int_\Omega \hat{\sigma}\,E\cdot M = \int_\Omega -\mathrm{i}\omega(\hat{\sigma}-\hat{\sigma}^p)E^p\cdot M \tag{1}$$

for $E, M \in \mathcal{H}_0(\nabla\times,\Omega)$, where ω is angular frequency, $\epsilon > 0$ is dielectric permittivity, μ is magnetic permeability, $\hat{\sigma} = \sigma + \mathrm{i}\omega\epsilon$ and $\hat{\sigma}^p = \sigma_p + \mathrm{i}\omega\epsilon$. E^p is the primary electric field, which is that of an arbitrarily 1-D earth of conductivity structure σ_p. We assume that $\sigma \approx \sigma_p$ close to the domain boundaries. The solution space is defined below:

$$\mathcal{H}_0(\nabla\times,\Omega) = \left\{ M{:}\Omega\to\mathbb{C}^3 : \int_\Omega (|M|^2 + |\nabla\times M|^2) < \infty, \; n\times M|_{\partial\Omega} = 0 \right\}. \tag{2}$$

The approximate solution to eq. (1) is obtained using edge elements. Secondary magnetic field H is calculated as

$$H = \frac{-\nabla\times E}{\mathrm{i}\omega\mu}. \tag{3}$$

The total field E^t, H^t is a sum of secondary and primary fields:

$$E^t = E + E^p, \quad H^t = H + H^p. \tag{4}$$

The MT response is obtained by finding Z, K such that

$$\begin{bmatrix} E^t_x \\ E^t_y \\ H^t_z \end{bmatrix} = \begin{bmatrix} Z_{xx} & Z_{xy} \\ Z_{yz} & Z_{yy} \\ K_{zx} & K_{zy} \end{bmatrix} \begin{bmatrix} H^t_x \\ H^t_y \end{bmatrix} \tag{5}$$

is satisfied no matter what is the polarization of the primary (E^p, H^p) plane wave.

3 GAUSS-NEWTON INVERSION PROCEDURE

For defining inversion terminology, we consider again fig. 1 of Part I (Kordy *et al.* 2015) where layers of hexahedral elements are deformed vertically to represent topography. This was efficient for the forward problem, but also will be for inversion. Although elements below the earth surface could be grouped to form a parameter, for maximal flexibility we usually consider each element as being a possible parameter linked through regularization in a tomographic inversion.

3.1 Description of the method

As is usual, the portion of the model domain Ω below the air–earth interface is split into N_m model parameters, which are disjoint regions with constant resistivity. Let $m = (m_1, \ldots, m_{N_m})$ be the vector of parameter $\log_{10}$ resistivity values. We work with $\log_{10}$ resistivity as this ensures that resistivity remains positive during inversion and makes the square norms of the reduced Hessian matrix columns more nearly equal in magnitude (Hohmann & Raiche 1988). There are N_d data points collected, denoted as $d = (d_1, \ldots, d_{N_d})$. As individual data values, we consider the real and imaginary parts of all entries in Z, K for all N_{rec} receivers, namely $N_d = 12N_{\mathrm{rec}}$ and for all frequencies. Let $e_1, \ldots, e_{N_d}$ be the vector of measurements errors, for which standard deviations s_i are known. By $F(m) \in \mathbb{R}^{N_d}$ we denote the response of the current model m, calculated by the forward code.

Denote B_d as a diagonal matrix with $\frac{1}{s_i^2}$ as entries. The inversion procedure seeks a model m such that the weighted data misfit

$$\|F(m)-d\|_{B_d}^2 = (F(m)-d)^T B_d (F(m)-d) = \sum_{i=1}^{N_d} \left(\frac{F_i(m)-d_i}{s_i}\right)^2 \quad (6)$$

is minimal, together with the constraint that some measure of roughness of the model m is limited. The roughness will be measured by

$$\|m-m_0\|_{B_m}^2 = (m-m_0)^T B_m (m-m_0) \quad (7)$$

where m_0 is a reference model and B_m is a symmetric non-negative definite matrix, so that $\|.\|_{B_m}$ is a seminorm. Often B_m is such that $\|m-m_0\|_{B_m} = \|\nabla(m-m_0)\|_{L_2}$, where ∇ denotes spatial gradient (in all three directions) of the $\log_{10}$ resistivity model. In the deformed mesh geometry we implement, the three directions in general are not purely perpendicular; one remains vertical while the other two lie along the variably deformed layer of elements.

Specifically, in the inversion we seek a model m that minimizes the functional

$$W(m) = \|F(m)-d\|_{B_d}^2 + \lambda \|m-m_0\|_{B_m}^2 \quad (8)$$

for some suitable value of $\lambda > 0$.

The Gauss–Newton is an iterative procedure that seeks a minimizer of (8). It starts with an initial guess m_1. Given a current model m_n, the Gauss–Newton scheme approximates the response $F(m)$ around m_n by the first-order Taylor expansion:

$$F(m) \approx F(m_n) + J\,[m-m_n] \quad (9)$$

where J is a $N_d \times N_m$ matrix of derivatives of F

$$J_{i,j} = \frac{\partial F_i}{\partial m_j}(m), \quad i = 1,\ldots,N_d, \quad j = 1,\ldots,N_m \quad (10)$$

whose computation we have described in Part I. If (9) is used, the functional (8) becomes quadratic and the minimizer m_{n+1} satisfies a linear equation:

$$[J^T B_d J + \lambda B_m](m_{n+1}-m_0) = J^T B_d \hat{d} \quad (11)$$

where $\hat{d} = d - F(m_n) + J[m_n - m_0]$.

The reduced Hessian matrix enclosed in square brackets in eq. (11) is dense, symmetric positive definite, and has dimension $N_m \times N_m$. This is the traditional model-space parameter update formulation. The numerical complexity of solving this equation using Cholesky decomposition is $O(N_m^3)$. This cubical growth eventually makes direct solution of the model-space Gauss–Newton scheme impractical for arbitrarily large model size N_m.

The data-space method (Parker 1994; Siripunvaraporn & Egbert 2000; Siripunvaraporn *et al.* 2005a) replaces eq. (11) with a linear equation having only N_d unknowns. For the moment we assume that B_m is invertible (which implies that B_m is positive definite and $\|.\|_{B_m}$ is a norm), the treatment of which we will revisit shortly. When (11) is left-multiplied by B_m^{-1}, we obtain:

$$B_m^{-1}[J^T B_d J + \lambda B_m](m_{n+1}-m_0) = B_m^{-1} J^T B_d \hat{d}$$

$$B_m^{-1} J^T (B_d J)(m_{n+1}-m_0) + \lambda(m_{n+1}-m_0) = B_m^{-1} J^T B_d \hat{d}$$

$$m_{n+1}-m_0 = B_m^{-1} J^T \frac{1}{\lambda} B_d [\hat{d} - J(m_{n+1}-m_0)]$$

This proves that

$$m_{n+1}-m_0 = B_m^{-1} J^T \beta \quad (12)$$

for some $\beta \in \mathbb{R}^{N_d}$. When (12) is plugged into (11) and the equation is left-multiplied by B_m^{-1}, we obtain an equation equivalent to (11):

$$B_m^{-1} J^T [B_d J B_m^{-1} J^T + \lambda I]\beta = B_m^{-1} J^T B_d \hat{d}. \quad (13)$$

This equation will be satisfied if β satisfies

$$[B_d J B_m^{-1} J^T + \lambda I]\beta = B_d \hat{d} \quad (14)$$

which is equivalent to

$$[J B_m^{-1} J^T + \lambda B_d^{-1}]\beta = \hat{d}. \quad (15)$$

The latter equation has a unique solution as $J B_m^{-1} J^T$ is symmetric nonnegative definite and B_d^{-1} is symmetric positive definite. The data-space Gauss–Newton method finds β, the solution to (15) and uses (12) to calculate a model update m_{n+1}.

The model update m_{n+1} in eq. (11) minimizes the inversion functional W using a linearized forward response F. However, the update may fail to decrease W if it is too far from current model m_n for the approximation in (9) to be accurate. A line search in the direction $m_{n+1} - m_n$ to minimize W (Nocedal & Wright 2006) can avoid this, but at the expense of multiple forward problems. One could use the Levenberg–Marquardt algorithm (Levenberg 1944) to keep the update m_{n+1} close to m_n by adding a term $\alpha\|m-m_n\|^2$ to W. This may be interpreted as choosing m_{n+1} that minimizes W for a trust region (Nocedal & Wright 2006) of models $\{m\colon \|m-m_n\|_2 \le \delta\}$ for some $\delta > 0$ than depends on α. The regularization term in W has a similar stabilizing effect, yet with a trust region defined as $\{m : \|m-m_0\|_{B_m} \le \delta\}$ for some $\delta > 0$ dependent on λ.

Apart from minimizing W, one also should select a value of λ to minimize the norm $\|m-m_0\|_{B_m}$ among models having a specific data misfit of X^2 (Parker 1994). A well-known method for this is Occam's inversion (Constable *et al.* 1987; deGroot-Hedlin & Constable 1990). As Occam also involves multiple forward calculations per iteration, we simply begin with a large value of λ and decrease it for subsequent iterations during the minimization. More precisely, λ that is used to obtain model m_{n+1} is set as:

$$\lambda = \mathrm{nRMS}(m_j)\cdot\kappa \quad (16)$$

From an initial value $\kappa_0 > 0$, parameter κ will be decreased by a factor of two if the normalized root mean square (nRMS) at an iteration does not fall by more than a user-specified amount (e.g. 10%). As a result in our inversions, the parameter λ steadily decreases and the model acquires increasing amounts of structure. This may be considered a form of cooling strategy (*cf.* Haber *et al.* 2007). The scaling with respect to nRMS is consistent with experience of Constable *et al.* (1987) where the optimal λ decreased as iterations proceeded and misfit improved. Procedures for determining λ warrant further investigation.

3.2 Computational considerations

In the data-space method, one has to invert B_m and apply it to J^T in order to calculate $J B_m^{-1} J^T$. In Siripunvaraporn & Egbert (2000), matrix B_m^{-1} was denoted C_m and called the model covariance matrix. It was not defined explicitly as a result of inverting a norm matrix B_m, but was treated as a natural matrix to consider for regularization.

The choice of a proper regularization functional $\|.\|_{B_m}$ is important, as minimizing the functional W in (8) is equivalent to minimizing the data misfit

$$(F(m)-d)^T B_d (F(m)-d) \quad (17)$$

subject to a condition on the model norm

$$\|m - m_0\|_{B_m} \leq \delta \tag{18}$$

where $\delta > 0$ depends on the choice of λ. The regularization functional we consider is L_2 norm of the gradient of the model,

$$\|m - m_0\|_{B_m} = \|\nabla(m - m_0)\|_{L_2}. \tag{19}$$

In order to use this functional in data-space method, matrix B_m must be inverted. However if (19) is used, B_m is non-negative definite and thus singular. To make it positive definite, we add a small number $\epsilon > 0$ to its diagonal before inverting. The functional is negligibly modified as then

$$\|v\|_{B_m} = \sqrt{\|\nabla v\|^2_{L_2} + \epsilon \sum_{i=1}^{N_m} v_i^2} \tag{20}$$

The nonzero value of ϵ tends to keep the inversion model slightly closer to the *a priori* model, which we do not view as a drawback. For very small values of ϵ, this effect is negligible.

To estimate the cost of calculation of $B_m^{-1}J^T$, we exploit the fact that matrix B_m has a nonzero pattern of a matrix coming from finite-difference approximation of a scalar Poisson equation over the inversion cell grid. Even if each inversion cell consists of only one element, the number of inversion cells will be no more than the number of vertices in the earth's subsurface. Thus B_m has less nonzero entries and less variables than the matrix used for the divergence correction described in Part I and the number of variables should be less. Even though the number of linear systems to be solved is $12 \times N_{\text{rec}}$, and for the divergence correction it was $5 \times N_{\text{rec}}$, here all variables are real valued. Thus if the solution library MKL PARDISO is used, the time of factorization of B_m and applying B_m^{-1} to J^T is expected to be less than the cost of applying the divergence correction, which takes a fraction of time of the forward problem. One concludes that the calculation of $B_m^{-1}J^T$ will not add a significant execution time to the inversion process no matter how large the grid is, as long as the direct solver is used for forward modeling.

For matrix multiplications like $J^T B_d J$ and the Cholesky factorization needed to solve eqs (11) and (15), we use the PLASMA library (Buttari *et al.* 2009; Baboulin *et al.* 2011). PLASMA is a linear algebra library for dense matrices, parallelized for shared memory machines (such as the SMP unit we use). It employs a matrix tiling approach (*cf.* Baboulin *et al.* 2005; Maris & Wannamaker 2010; Kordy *et al.* 2013), which reduces the time of transporting the matrix entries from RAM to CPU. The scalability of Cholesky factorization and matrix multiplication using PLASMA is presented in Fig. 1. The speedup using 24 cores is ∼17 and ∼19 for Cholesky factorization and matrix multiplication, respectively.

To assemble the model-space Gauss–Newton matrix (11), one has to evaluate $J^T B_d J$, which has numerical complexity $O(N_m^2 N_d)$. Solving the matrix as noted previously has complexity $O(N_m^3)$. For the data-space method on the other hand, to assemble the matrix in eq. (15) one has to evaluate $(B_m^{-1}J^T)$. By analysing the run-times for models 2–5 of Table 1, we estimate the numerical complexity to be $O(N_m^{1.13})$, $O(N_m^{1.5})$ and $O(N_d N_m^{1.18})$ for the reordering, factorization and the solution phases, respectively. Most of the time (over 98%) for the considered test cases is spent in the solution phase. With the direct solver approach, the time to calculate $(B_m^{-1}J^T)$ is always a small fraction of the cost of the forward problem. Further, $(B_m^{-1}J^T)$ is used to evaluate $J(B_m^{-1}J^T)$, which has numerical complexity $O(N_m N_d^2)$. Solving the equation

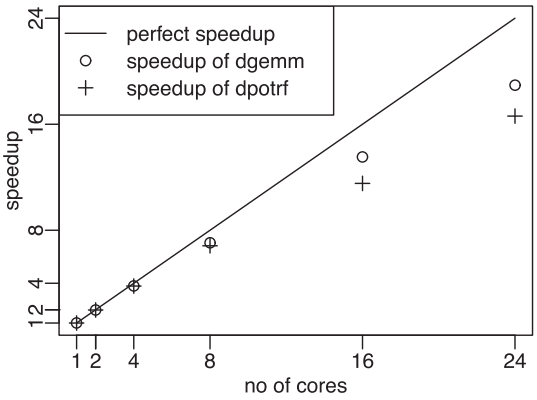

Figure 1. Speedup of PLASMA library for Cholesky factorization (dpotrf) and matrix multiplication (dgemm).

using Cholesky decomposition has complexity $O(N_d^3)$. As typically $N_d < N_m$, the computational cost associated with data-space method is less. The difference becomes more pronounced for larger MT surveys.

Example computation times for models listed in Table 1(a) are presented in Table 1(b). The time to solve the model-space Gauss–Newton eq. (11) increases rapidly with the model size and quickly gets impractical, reaching over 27 hr for the largest grid considered. On the other hand, the time to solve the data-space eq. (15) remains short, less than one minute for all the grids considered. In the case of the data-space method, more time consuming than solving eq. (15) is evaluating $J(B_m^{-1}J^T)$, which takes 1 hr for the largest mesh considered. Nevertheless, the corresponding evaluation of $J^T B_d J$ for model-space Gauss–Newton takes longer, more than seven times longer for mesh 5. Comparable to the time of calculation of $J(B_m^{-1}J^T)$ is the time of evaluation of $B_m^{-1}J^T$. However, as we expected, this time is less than that of applying the divergence correction (more than two times less), which in turn is almost 10 times less than the total time spent solving forward problem. Thus the advantage of the data-space Gauss–Newton approach over the model-space version for this application is clear.

Concerning RAM requirements, for model-space GN one needs to store the matrix J, which is $N_d \times N_m$ as well as the matrix in the eq. (11), which is a symmetric $N_m \times N_m$ matrix. In the data-space version, one needs to store matrix J and the matrix $B_m^{-1}J^T$ of the same size, but depending on implementation those may be saved on hard disk and parts of them may be read into RAM memory when needed. Also, one needs to store the matrix of eq. (15), which is a symmetric $N_d \times N_d$ matrix. One can see that as typically $N_d < N_m$ the memory requirements are smaller for data-space Gauss–Newton than for its model-space cousin.

In Table 1(c) we present the RAM memory requirements for the grids considered. The matrix J is $N_d \times N_m$ in size, but largely can be stored on hard disk and parts accessed as needed. For the largest mesh considered, the model-space GN update requires 413 GB, whereas the data-space update requires as little as 7.9 GB of RAM memory depending upon treatment of J.

3.3 Regularization norm weight

Up to this point, we have not specified details of the entries of matrix B_m, other than that it is a finite-difference representation of spatial gradients in the model parameter vector m. Several investigators have explored whether entries of B_m should also be weighted

Table 1. Run-times and memory use for forward modeling, model-space Gauss–Newton iteration and data-space Gauss–Newton iteration.

ID	FEM grid	inversion grid	edges no	recv no	freq no	N_d	N_m
1	$41x\ 41y\ 30z$	$39x\ 39y\ 19z$	143 120	81	13	12 636	28 899
2	$65x\ 65y\ 45z$	$63x\ 63y\ 29z$	550 400	121	15	21 780	115 101
3	$81x\ 81y\ 47z$	$79x\ 79y\ 31z$	896 960	64	15	11 520	193 471
4	$81x\ 81y\ 47z$	$79x\ 79y\ 31z$	896 960	196	15	35 280	193 471
5	$101x\ 101y\ 50z$	$99x\ 99y\ 34z$	1,489 800	256	15	46 080	333 234

(a) Statistics of test meshes used for run times testing.

ID	FP total	FP DC	GN J^TB_dJ	GN slv	DS $B_m^{-1}J^T$	DS JJ^T	DS slv	DS tot.
1	00:03:57	00:00:30	00:00:38	00:00:25	00:00:13	00:00:24	00:00:03	00:04:46
2	00:39:47	00:04:32	00:14:42	00:25:09	00:02:16	00:03:40	00:00:15	00:46:41
3	01:00:14	00:05:33	00:22:18	01:59:12	00:02:02	00:02:11	00:00:03	01:05:12
4	02:04:20	00:11:53	01:05:05	01:59:27	00:07:28	00:15:29	00:01:01	02:30:36
5	04:04:15	00:28:52	03:55:47*	10:00:49*	00:19:15	00:44:28	00:02:22	05:07:58

(b) Run times in format hh:mm:ss for meshes listed in table 1(a). "FP" denotes the total time of calculation of the forward problem (response $F(m)$ and Jacobian J) using MKL PARDISO. "FP DC" is the time spent on divergence correction using MKL PARDISO (fraction of "FP"). "GN J^TB_dJ" denotes the time spent on evaluation of J^TB_dJ using PLASMA. "GN slv" denotes time needed to solve Gauss-Newton equation (11) using PLASMA once the matrix $J^TB_dJ + \lambda B_m$ has been assembled. "DS $B_m^{-1}J^T$" denotes the time spent to calculate $B_m^{-1}J^T$ using MKL PARDISO. "DS JJ^T" denotes the time spent to evaluate $J(B_m^{-1}J^T)$ using PLASMA. "DS slv" denotes the time spent to solve equation (15) using PLASMA, once the matrix $JB_m^{-1}J^T + \lambda B_d^{-1}$ has been assembled. * denotes the estimated time, the calculation hasn't been done due to insufficient RAM memory. "DS tot." denotes the total time of one data space Gauss-Newton iteration. For the GN solve time, the estimate has been calculated by fitting a line for $\log(time)$ and $\log(N_m)$. The estimate for the matrix multiplication time has been calculated by fitting a linear model for $\log(time)$ as a function of $\log(N_m)$ and $\log(N_d)$. The calculations have been done on a 24-core workstation (four Intel Xeon E5-4607 v2 Hexa-core 2.60 GHz processors)

ID	N_m	N_d	FP	J	GN	DS
1	28 899	12 636	1.8 GB	2.7 GB	3.1 GB	0.6 GB
2	115 101	21 780	10.1 GB	18.7 GB	49.4 GB	1.8 GB
3	193 471	11 520	20.0 GB	16.6 GB	139.4 GB	0.5 GB
4	193 471	35 280	20.0 GB	50.9 GB	139.4 GB	4.6 GB
5	333 234	46 080	34.2 GB	114.4 GB	413.7 GB	7.9 GB

(c) RAM memory needed for matrices related to Gauss-Newton update using model-space and data-space for meshes listed in table 1(a). "FP" denotes RAM needed to calculate the forward problem. "J" denotes the memory needed to store the matrix J of size $N_m \times N_d$. "GN" denotes the memory needed to store the (symmetric) matrix $J^TB_dJ + \lambda B_m$ of size $N_m \times N_m$. "DS" denotes the memory needed to store the (symmetric) matrix $JB_m^{-1}J^T + \lambda B_d^{-1}$ of size $N_d \times N_d$.

according to influence (Jacobian) of their corresponding parameter (e.g. Zhdanov 2002; Yi *et al.* 2003). Here we present three different regularization functionals, the performance of which will be compared in numerical tests.

Consider the infinite-dimensional problem and its response $F(m)$ given a spatially varying $\log_{10}$ resistivity model $m = m(\mathbf{r})$. Also consider the derivative $S(\mathbf{r})$ of F with respect to m satisfying:

$$F(m + \delta m) \approx F(m) + \int_\Omega S(\mathbf{r})\delta m(\mathbf{r})d\mathbf{r} \tag{21}$$

for a small change in model δm. The quantity $\|S(\mathbf{r})\|_2$ measures the sensitivity of the response F to the change of the conductivity at the point $\mathbf{r}$.

As the regularization functional $(m - m_0)^TB_m(m - m_0)$, we will consider L_2 norms of the gradient of m with a weight $\nu(\mathbf{r}) > 0$ defined as follows:

$$\|\nabla(m - m_0)\|^2_{L_2(\nu)} = \int_\Omega |\nabla(m - m_0)|^2\nu(\mathbf{r})d\mathbf{r} \tag{22}$$

Further, we consider three possible values for ν:

$$\begin{aligned}\nu(\mathbf{r}) &= \|S(\mathbf{r})\|_2\\ \nu(\mathbf{r}) &= 1\\ \nu(\mathbf{r}) &= \frac{1}{\|S(\mathbf{r})\|_2}\end{aligned} \tag{23}$$

Norm $\|\nabla(m - m_0)\|_{L_2(1)}$ uses no information about the influence of the inversion cell on the data. If norm $\|\nabla(m - m_0)\|_{L_2(\|S\|_2)}$ is used for regularization, smoothing is suppressed for parameter regions with low sensitivity allowing them to show additional structure (*cf.* Zhdanov 2002). Norm $\|\nabla(m - m_0)\|_{L_2(\frac{1}{\|S\|_2})}$ will smooth the model in regions with low sensitivity, using the reasoning that if we cannot detect the properties of a region well, we will make it similar to its surroundings. This is similar to the approach of Yi *et al.* (2003), although they make a rigorous evaluation of the parameter resolution matrix which is computationally intractible for the larger problems we consider here.

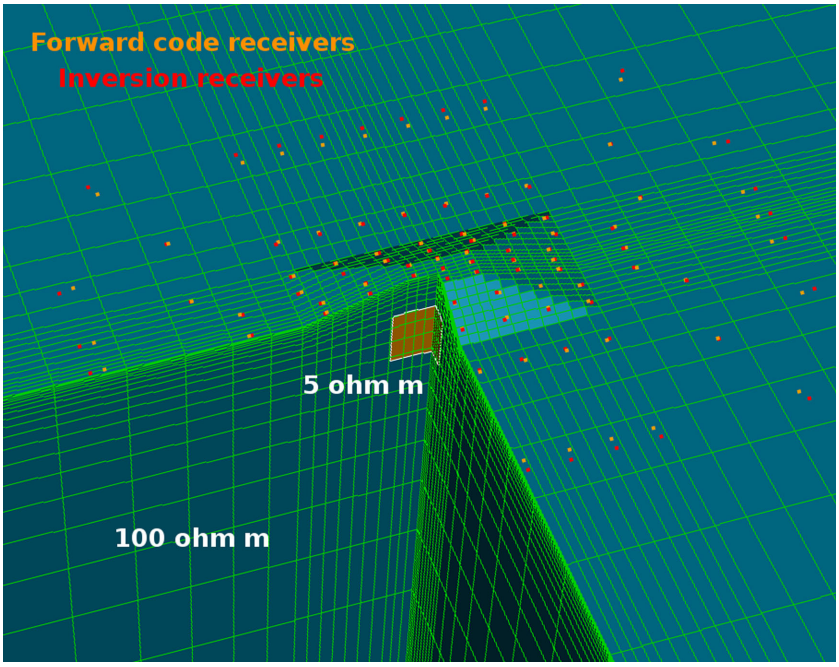

Figure 2. Central part of the inversion grid together with the receiver locations in three quadrants. Conductive brick is shown below the hill.

If the norms $\|m - m_0\|_{L_2(v)}$ and $\|\nabla(m - m_0)\|_{L_2(v)}$ are properly approximated on a discrete level, they will be mesh independent. An explanation of this claim and the details of the way we approximate the norms are provided in Appendix A.

4 SYNTHETIC INVERSION EXAMPLES

In this section, we present results of the inversion of synthetic MT data to evaluate algorithm performance under controlled conditions. As a measurement error we will use the value

$$\begin{aligned} e(Z_{ij}) &= \max\left\{3.5\%\tfrac{|Z_{xy}-Z_{yx}|}{2}\right\}, \quad i,j = x,y \\ e(K_{zj}) &= 0.03, \qquad\qquad\qquad\quad j = x,y \end{aligned} \tag{24}$$

We use $Z_{xy} - Z_{yx}$ because it is a rotational invariant and shows relative stability to data noise (see Groom & Bahr 1992). As the measurement error s_j (noted in (6)) for real or imaginary part of Z and K, we take the above value e. The data used in the inversion are calculated by the forward problem for the true conductivity model, with Gaussian noise having zero mean and standard deviation s added to the real and imaginary parts of Z and K.

To assess goodness of fit of a model response to the data, we use the nRMS, defined as:

$$\mathrm{nRMS}(m) = \sqrt{\frac{1}{N_d}\sum_{j=1}^{N_d}\left(\frac{d_j - F_j(m)}{s_j}\right)^2} \tag{25}$$

where d is the vector of our synthetic data, F is a vector of response of the model m and s is the measurement error vector.

4.1 Brick under a hill

Our first model is a brick under a hill in 100 Ωm background. The hill has dimensions 2000 and 4000 m in x- and y-directions at the bottom and 500 and 1000 m at the top. The hill is 450 m high. The object is placed below the hill with the top and the bottom of the object at 650 and 1600 m, respectively, below the top of the hill and its XY cross-section is a rectangle $[-328\text{ m}, 328\text{ m}] \times [-700\text{ m}, 700\text{ m}]$. We consider a conductive (5 Ωm) and resistive (2000 Ωm) object as well as no object at all. We compare the inversion that has the mesh conforming to the topography as in Fig. 2 to the mesh without topography (flat surface). Both meshes have the same location of cells in x- and y-directions and the same x and y coordinates of receivers. The only difference is the elevation of layers close to the earth surface.

We generated the data using a different grid than the one used for inversion. The forward code grid was $95x$, $95y$, $50z$ and extended to 18 km from the grid centre in x- and y-directions, 5.6 km above the earth's surface (air layer) and 12.5 km below the surface. The inversion grid was $41x$, $41y$ and $30z$. It extended 14 and 15 km from the centre of the grid in x- and y-directions, respectively. There were 106 receivers. The location of a receiver is always at the centre of the face of an element lying on the earth's surface, thus the location of the forward code receivers is slightly different than the inversion receivers. The inversion grid, together with the location of the brick and receivers in three of the four quadrants is presented in cutaway view in Fig. 2.

The data consisted of the impedance Z and the tipper K for 13 frequencies between 1 and 1000 Hz distributed evenly in $\log_{10}$ space. We added Gaussian error with standard deviation (24) to the forward data. The initial value of κ_0 started at the same value for all inversions. The starting and reference (*a priori*) models were set to 50 Ωm uniformly. The regularization functional used was $\|\nabla m\|_{L_2(1)}$.

Iteration history is presented in Fig. 3. The regularization norm $\|\nabla m\|_{L_2(1)}$ increases as the inversion proceeds and λ decreases in the effort to decrease nRMS. One can see that inversion with topography is able to achieve nRMS close to 1 in less than 3 iterations, whereas the inversion without topography is struggling to decrease nRMS below 1.6 even though the model norm is larger than in the case of inversion with topography.

We have plotted cross-sections of selected models for six inversions in Figs 4 and 5 for comparison. In all cases, the inversion with topography is able to recover a smoothed version of the original

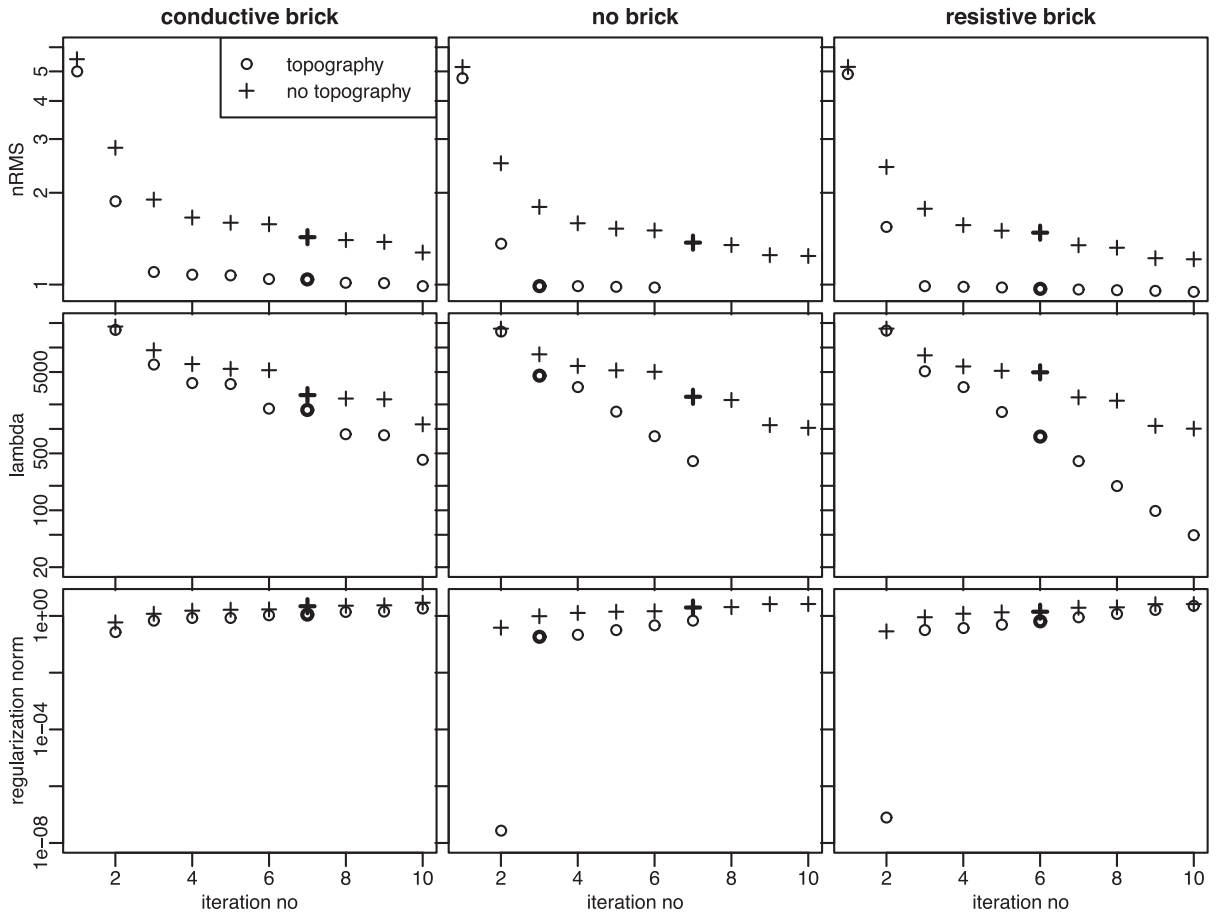

Figure 3. Inversion iteration history for model of bricks under a hill. nRMS(m_j), λ used to obtain model m_j, $\|\nabla m\|_{L_2(1)}$ as a function of iteration number j are plotted. The models plotted in Figs 4 and 5 are denoted by bold symbols.

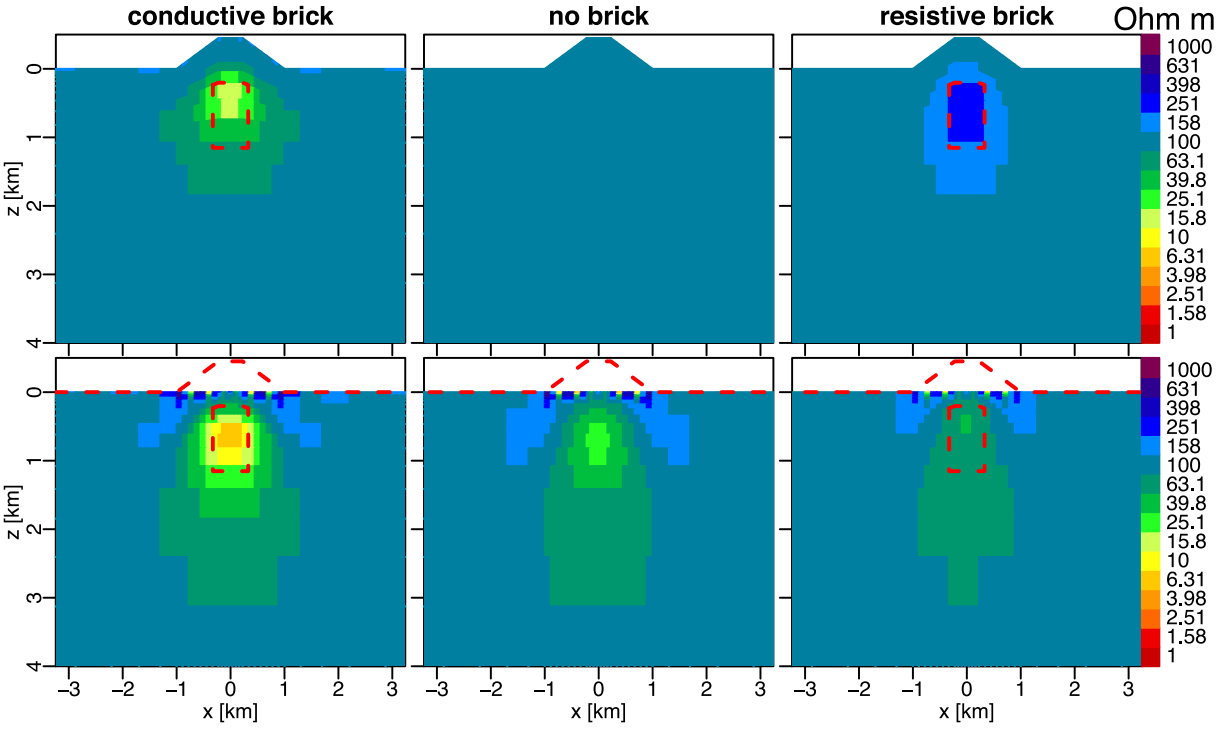

Figure 4. Inversion results for bricks under a hill along *XZ* cross-section at $y = 0$ km. Top row shows inversion with topography, bottom row the inversion without topography.

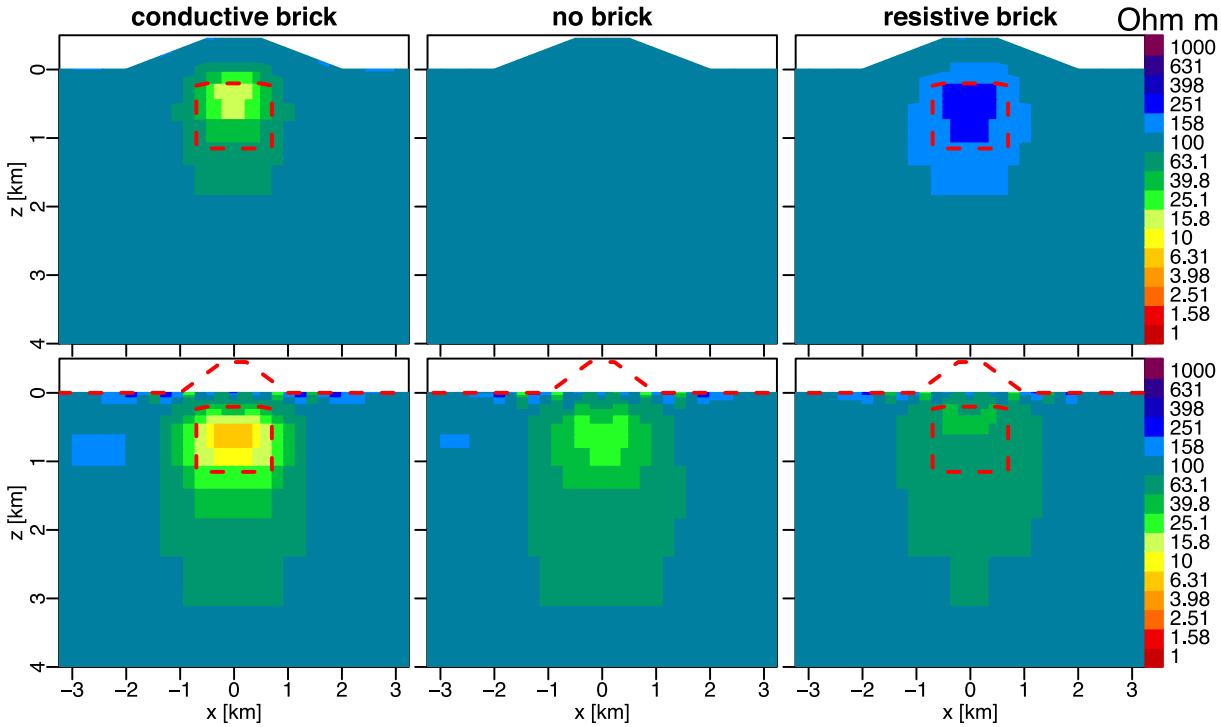

Figure 5. Inversion results for bricks under a hill along *YZ* cross-section at $x = 0$ km. Top row shows inversion with topography, bottom row the inversion without topography.

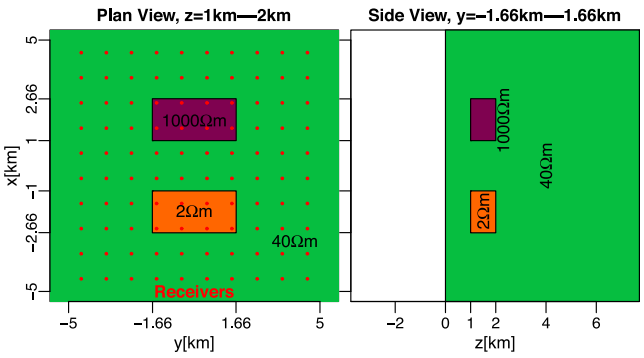

Figure 6. Sketch of two bricks model.

object (or no object in the no brick case). Inversion without topography puts a more conductive object below the ground to make-up for the absence of a hill. This occurs because the electric field is reduced by the hill as background electric current only partially flows upward into that volume (see TM mode results in Wannamaker *et al.* 1986). Even for the resistive brick forward data, the inversion without topography returns a (somewhat) conductive object. The inversion also creates an oscillatory region above the object (more apparent on *XZ* cross-section) that resembles the shape of a hill. These results emphasize the importance of including the topography in the inversion of MT data.

4.2 Simple two brick model

Our next synthetic model consists simply of two buried and separated bricks, one conductive (2 Ωm) and one resistive (1000 Ωm), in a 40 Ωm half-space (Fig. 6). With this model we examine the effect of inversion regularization weights on model characteristics.

The forward mesh consists of $58x$ $58y$ $45z$ elements. In the *XY* plane, the central 33×33 elements are square with sides equal to 0.333 km. Further from the centre, the element sizes grow gradually and extend 130 km from the centre of the grid. In the *Z*-direction, there were 34 elements below the surface and 11 elements in the air. The mesh extends to 100 km above the surface and 140 km below the surface. There are 10×10 receivers evenly distributed in *XY* plane, separated by 10 km. The forward response (impedance *Z* and tipper *K*) was generated for 31 frequencies evenly distributed in log space between 0.01 and 1000 Hz, which gives six frequencies per decade. We added Gaussian error with standard deviation (24) to the forward data.

The inversion mesh consists of $41x$ $41y$ $41z$ elements. In the *XY* plane, the central 24-by-24 elements are square with sides equal to 0.5 km. Further from the centre, the element sizes grow gradually and extend 135 km from the centre of the grid. In the *Z*-direction, there were 31 elements below the surface and 10 elements in the air. The mesh extends to 110 km above the surface and 140 km below the surface. Thus the forward and inversion meshes differ in discretization but have the same locations for the receivers, which are at the centre of elements faces in both cases. The inversion mesh is presented in Fig. 7.

For this model, we conducted inversions using different regularization functionals. We used (A5), (A2) and (A7) that give regularization functionals resembling $\|\nabla m\|^2_{L_2(\|S\|_2)}$, $\|\nabla m\|^2_{L_2(1)}$, and $\|\nabla m\|^2_{L_2(1/\|S\|_2)}$, respectively. The value of $\|S\|_2$ was confined to change within a factor of 10^4. More precisely, two values were found S_1 and S_2, such that $\frac{S_2}{S_1} = 10^4$ and the value of $\|S\|_2$ was truncated if it lies outside the interval $[S_1, S_2]$. Additionally, weights ν have been multiplied by a normalization constant, so that the average ν over the central part of the domain is the same in all cases. This allows us to use the same initial value of λ. The nRMS, λ and the regularization norm as a function of the iteration number

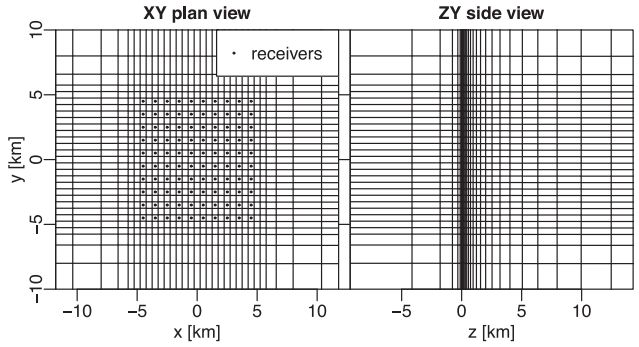

Figure 7. Cross-sections of the inversion grid for the two bricks model. Central part of the grid is shown.

are presented in Fig. 8. One can see that the nRMS values as a function of iteration number are almost the same for the different regularization schemes, and thus the amount of regularization is similar for all weightings.

The models calculated by the different inversion schemes at iteration 6 are presented in Fig. 9, with weights ν of $L_2(\nu)$ norms used for regularization to obtain those models plotted in Fig. 10. Generally speaking, the weight $\nu = \|S\|_2$ decreases with depth and the weight $\nu = \frac{1}{\|S\|_2}$ increases with depth. Thus, the effect of using $L_2(\|S\|_2)$ is to prolong the depth extent of the formed image to minimize the value of the regularization norm. For $L_2\left(\frac{1}{\|S\|_2}\right)$, the recovered objects tend to be compressed toward the surface for comparable reasons. In the case of $L_2\left(\frac{1}{\|S\|_2}\right)$, significant resistivity oscillations are apparent at shallow depths; one of their effects is to drive the background resistivity toward 25 Ωm rather than the true 40 Ωm because of the cell-scale heterogeneity formed under the receivers. Nevertheless, the nRMS values are all very close, underscoring the non-uniqueness inherent in this ill-posed inversion problem. We observed no systematic difference in the fit of the final models across the frequency range for the three regularizations. Results for other models might differ, however. Further challenges in establishing appropriate regularization may be expected for more complex settings.

4.3 DSM2 model

The Dublin MT Modeling and Inversion workshops have provided model results for the EM community to test newly developed simulation and imaging codes (see Miensopust *et al.* 2013). Here we consider inversion of the MT responses of the Dublin secret model 2 (DSM2) presented in Fig. 11. It is a flat-earth model with two contacting, shallow bricks in a four-layer earth. There are 144 MT receivers arranged in a uniform grid 12 × 12 with 7 km spacing.

The forward data, supplied by the workshop organizers, consist of the impedance tensor Z values only (no tipper) for 30 frequencies between 0.016 and 10 000 s evenly distributed in $\log_{10}$. Random galvanic distortion was applied to the responses by the organizers as described in Miensopust *et al.* (2013). Gaussian noise of 5% of the maximal impedance value also had been added to the distorted data set. This supplied error bound was treated as a standard deviation and was used for both real and imaginary parts of Z. The data from all sites and frequencies were used in our inversion.

The applied static distortion provides an opportunity for us to implement and test recent distortion removal procedures (Avdeeva *et al.* 2015), summarized in Appendix B. Initially, an inversion model is sought without distortion correction. This model is used as an initial guess to estimate a new, more stable model plus the static distortion matrices of the impedance Z. We invert the data using the $L_2(1)$ regularization functional.

We considered coarse and fine inversion meshes. The coarse mesh has two columns of parameters between sites in the central portion of the model whereas the fine mesh has five columns of parameters between sites. The purpose of the latter mesh is to test whether a fine discretization allows formation of small-scale shallow structure which can simulate the impedance galvanic distortion without having to solve explicitly for correction factors (*cf.* e.g. Meqbel *et al.* 2014).

Specifically, the coarse(fine) mesh consisted of 45x 45y 41z(78x 78y 50z) elements. In the XY plane, the central 23-by-23(58-by-58) elements are squares with sides = 3.5 km (1.4 km). Further from the centre, the element sizes grow gradually and extend 600 km from the centre of the grid. In the Z-direction, there were 31(38) elements below the surface and 10(12) elements in the air. The mesh extends to 300 km above the surface and 700 km below the surface. The central part of the coarse mesh is presented in Fig. 12.

The inverted models are presented in Fig. 13. Inverting only for $\log_{10}$ resistivity on the coarse mesh with no distortion correction yields a model with nRMS of 4.2, with little further improvement by relaxing the regularization factor (see Fig. 14). Subsequently, inverting also for the distortion matrices obtains a model with nRMS of 1.1. The latter model achieves generally smoother resistivity structure with values closer to the true values, especially in the deeper structure, than does the former model. For the coarse model,

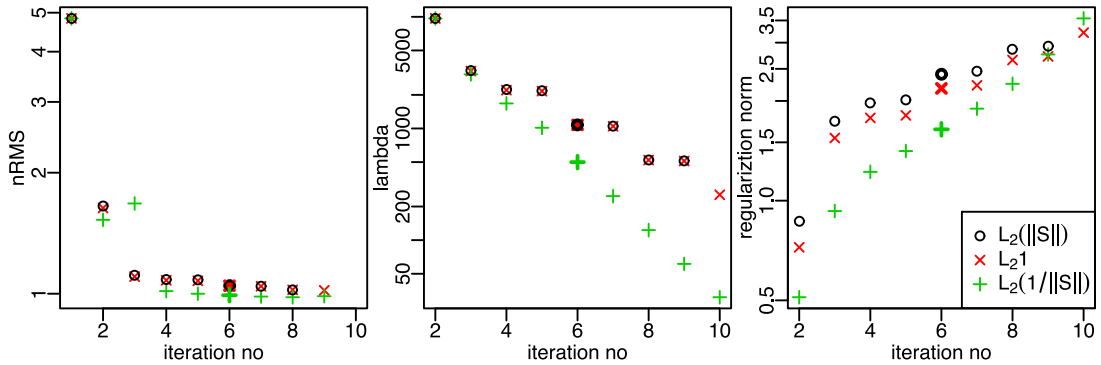

Figure 8. Two bricks model iteration history. nRMS(m_j), λ used to obtain model m_j as well as $\|m_j - m_0\|_{B_m}$ as a function of iteration number j are plotted. The model number 6, plotted on Fig. 9 is denoted by a bold symbol.

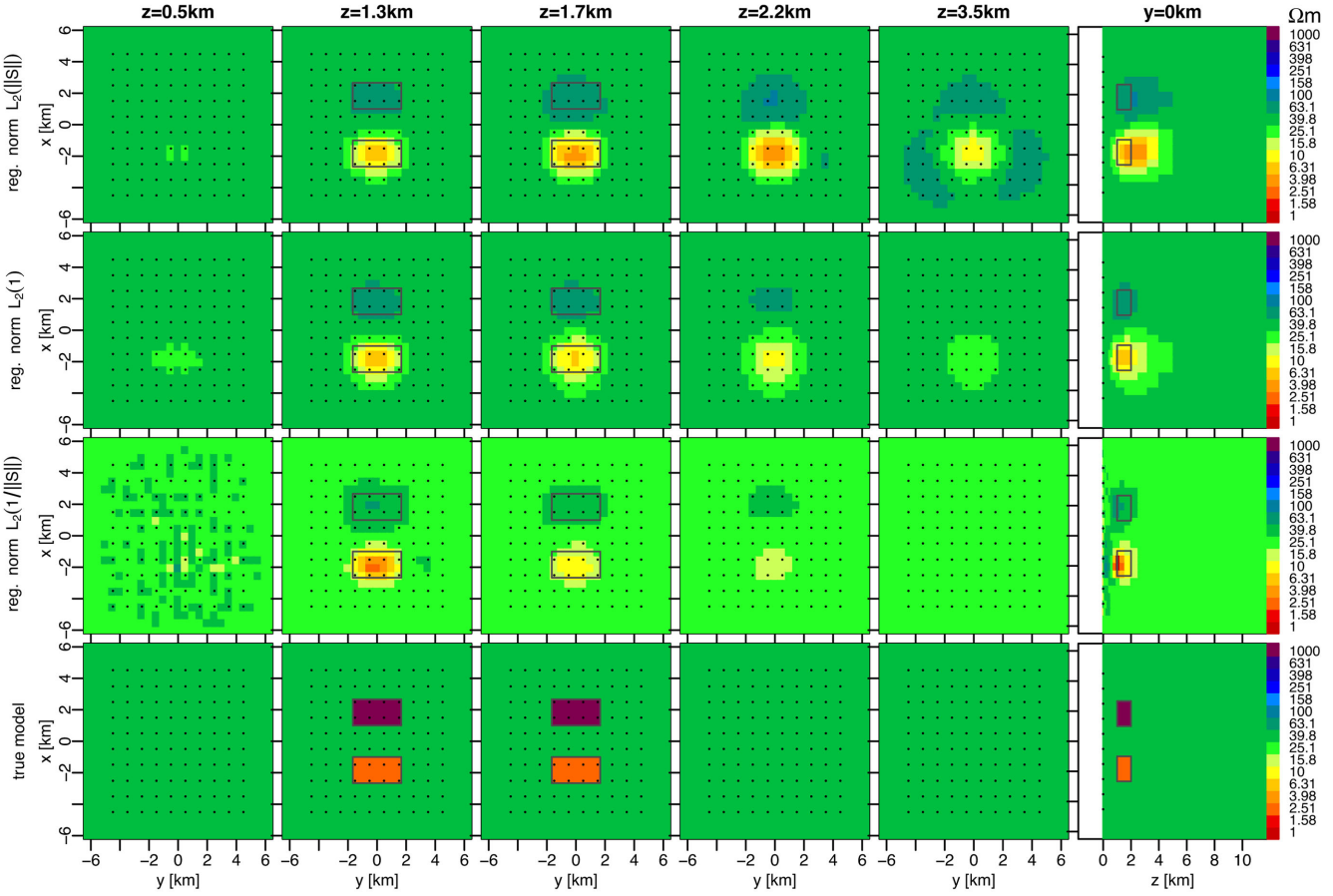

Figure 9. Models calculated by inversions of synthetic responses of two bricks using regularization functionals $\|\nabla m\|^2_{L_2(\|S\|_2)}$, $\|\nabla m\|^2_{L_2(1)}$ and $\|\nabla m\|^2_{L_2\left(\frac{1}{\|S\|_2}\right)}$. In each case, the model obtained at iteration 6 is plotted.

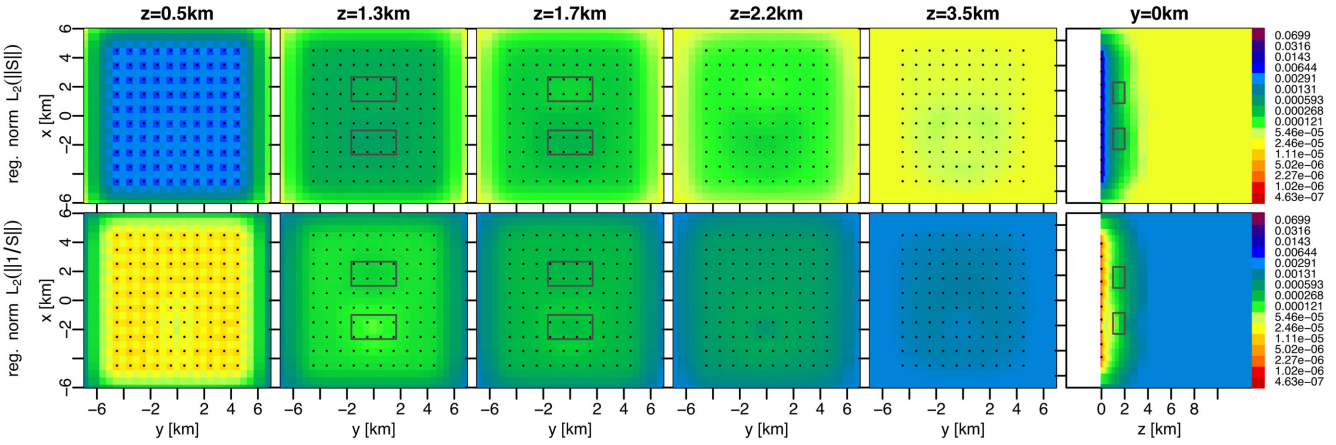

Figure 10. Weight ν of $L_2(\nu)$ norm used to obtain model number 6 for regularization schemes used for two bricks model. For $L_2(1)$ regularization, the weight is constant so is not plotted.

there is some scatter in the norm of distortion matrices versus iteration. This presumably is a result of small regularization ($\tau = 0.01$). Further investigation is warranted as to when and to what degree of regularization, distortion should be estimated through the iteration history.

When the fine mesh inversion for $\log_{10}$ resistivity only is considered, the resulting model has nRMS of 2.2, significantly less than the similar model obtained on a coarse mesh. The fine mesh inversion is able to represent some of the distortion by small-scale variability of $\log_{10}$ resistivity in the vicinity of the receivers, at shallow depths. Nevertheless, the fine mesh inversion for $\log_{10}$ resistivity including the distortion estimation provides a smoother model with a smaller nRMS of 1.1 (see Fig. 14). Here we see smoother behaviour in the estimated distortion versus iteration. From this result we suggest

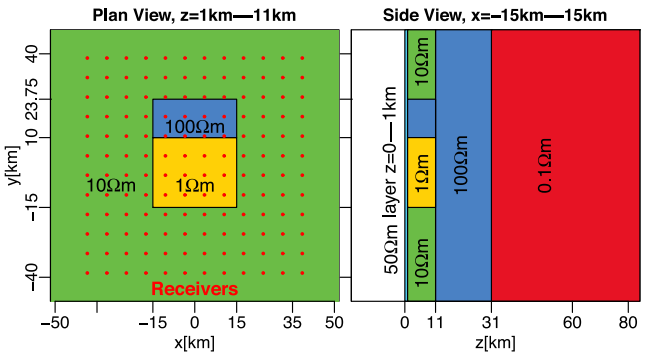

Figure 11. Sketch of DSM2 model.

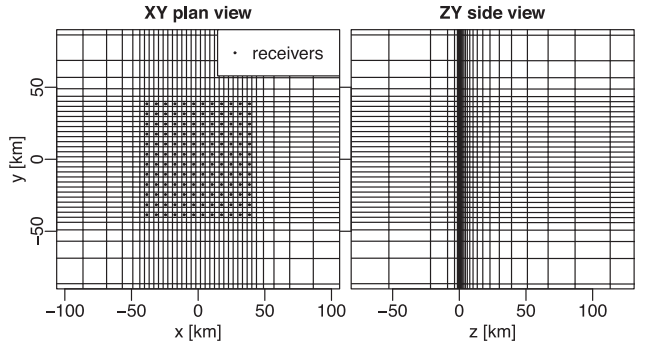

Figure 12. Cross-sections of the central part of the coarse inversion grid for DSM2 model.

that distortion matrices should be considered in tensor impedance inversion even for fine discretizations. However, we also advocate that fine discretization be used to the extent practical to ensure that non-galvanic variations at the highest frequencies are accommodated by the smallest scale mesh structure.

5 FIELD INVERSION EXAMPLES

5.1 Mount St Helens

Finally, we examine the MT field data set collected by Hill *et al.* (2009) from the north-central Cascade volcanic environment in Washington State, USA, to demonstrate the ability of our solution to handle moderately large models with topography. There are 82 soundings primarily clustered over the recently active Mount St Helens volcano, but with 14 of the sites extending in a nearly E-W profile past the north side of Mount Adams (Fig. 15). This gives us the opportunity also to compare 3-D inversion of profile data (e.g. Siripunvaraporn *et al.* 2005b) with 2-D inversion results. We invert the complex tensor impedance Z and tipper K for 20 frequencies log-uniformly distributed from 100 through 0.0018 Hz.

The mesh consists of $111x$ $167y$ $62z$ elements in total (see Fig. 16). This requires storage of 500 GB which fills the capacity of our particular workstation. Over the large central section including the two volcanoes, horizontal dimensions of the elements were in the 500 × 600 to 500 ×1000 m range typically. Around this region the element sizes grew gradually, covering a total area of 375 km × 425 km. In the z-direction, there are 50 elements below the ground and 12 elements in the air. The elements at the earth's surface have a thickness of 80 m (at mesh edge) and grow gradually to reach an elevation of 250 km above the surface and a depth of 220 km below the ground. Topography for the area was obtained from ASTER GDEM data (downloaded from http://gdex.cr.usgs.gov/gdex/), a product of METI and NASA. We did not attempt to include the Pacific Ocean nearly 200 km to the west, as that distance is significantly larger than the depth range of interest here (<100 km). A rim of one element around the side edges and bottom of the mesh was excluded from the inversion and fixed to be a 1-D (flat) initial model. Thus, there are 109 × 165 × 49 = 881 265 inversion parameters in the Mount St Helens model. However, in data-space formulation, the rank of the model update matrix is only 19 680. This may seem like a large model to handle 82 MT sites, but that is a result of particular site distribution. In principle, many more MT sites could be placed in this model mesh with additional computational cost only being more Jacobian source reductions and a larger (though still modest) data-space model update matrix.

The inversion was run without distortion matrix estimation for 11 iterations, with iteration history shown in Fig. 17. Data error floors as given in eq. (23) were adopted. The starting model was a 100 Ωm half-space, the same as considered by Hill *et al.* (2009), and the starting nRMS was ∼11.5. Run-time on the 24-core workstation was ∼13 hr per iteration, which was by far dominated by the forward and Jacobian calculations over the 20 frequencies. Model 11 has nRMS of 1.2, which is considered a good fit so that distortion correction should yield little improvement and was not carried out.

Model cross-section and plan views are presented in Figs 18 and 19, and can be compared to the original results of Hill *et al.* (2009). The cross-section overall bears a close resemblance to the 2-D inversion of Hill et al, which emphasized the nominal TM mode (relative to profile orientation) of data. Steep low resistivity is seen in the middle crust directly under Mount St Helens, presumably related to recent eruptive processes, of which more will be discussed shortly. This gives way at depths >20 km to broad, quasi-horizontal low resistivity between the two volcanoes, which we attribute to lower crustal magmatic underplating and high-temperature fluid release. Shallow, very low resistivity overlies the deep crustal conductor approaching Mount Adams which may reflect in part the presence of graphitic metasediments associated with a suture between the Siletz terrane and former North American margin (the southern Washington Cascades conductor or SWCC of Stanley *et al.* 1996), although this interpretation is non-unique and not without controversy (Egbert & Booker 1993; Hill *et al.* 2009). A large resistive body extending to >15 km depth lies between the Mount St Helens and Mount Adams and could be correlated with earlier Western Cascades intrusive rocks (see Wannamaker *et al.* 2014).

The steep low resistivity directly under Mount St Helens in Fig. 18 is similar to that in the flat-earth 3-D inversion model of Hill *et al.* (2009) although the most anomalous portion does not extend to quite as shallow a depth as that in Hill's. This may in part be explained by the conical edifice of the volcano inducing additional depression of the electric field as discussed with Fig. 4. A second, somewhat lesser conductor in the 4–9 km depth range appears just west of the first one, which is more subtly expressed in the model of Hill *et al.* These two conductors correspond reasonably well to the two high-scattering bodies displayed in east–west section by DeSiena *et al.* (2014, their fig. 6e). In plan view at 7 km depth (Fig. 19), we see that this steep conductor is strongly linear in a nearly N-S direction and is associated with the Mount St Helens shear zone (MSZ) passing through the volcanic edifice (Weaver *et al.* 1987; Lagmay *et al.* 2000). Clear representation of this structure in our model we believe may be due to inclusion of the tipper elements in the inversion, as the tipper shows a subtle reversal on the west flank of the volcano (Hill *et al.* 2009, also see our Supplemental Material

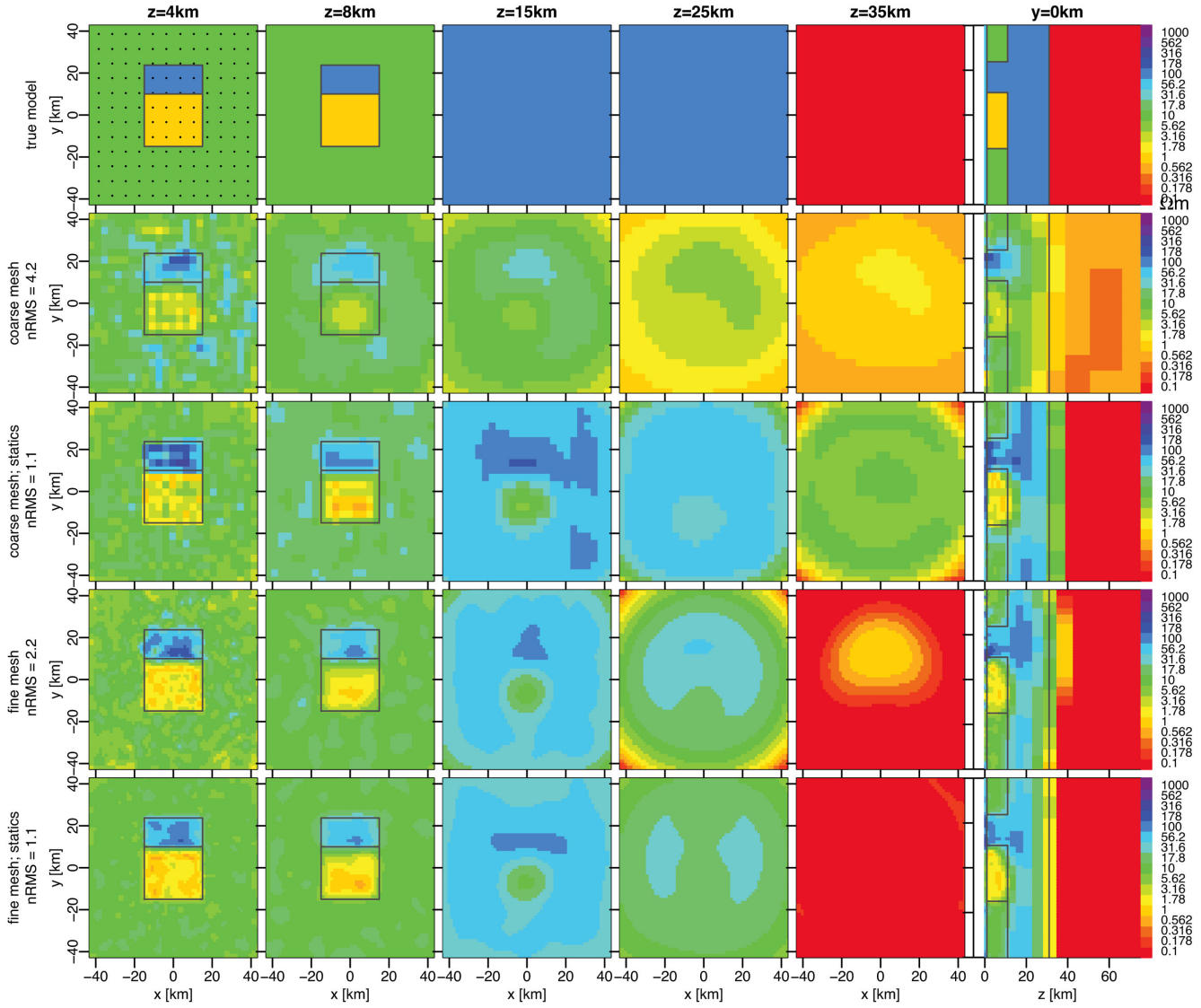

Figure 13. Comparison of inversion models obtained for DSM2 model. The second and the third rows contain the result of inversions on a coarse mesh. The fourth and the fifth rows show results of inversions on a fine mesh. The third and the fifth rows, denoted by 'statics', show results of inversions for $\log_{10}$ resistivity and the static distortion matrices. The top row shows the true model.

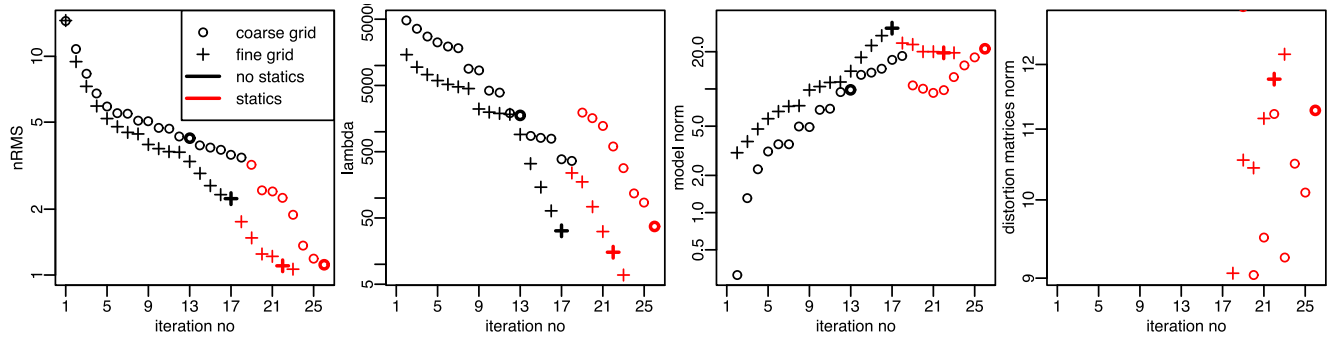

Figure 14. Iteration history for DSM2 model, for coarse and fine meshes. Initial inversion without static distortion is shown in black. Subsequent inversion with distortion matrix estimation is plotted in red. Bold symbols denote models shown in Fig. 13.

section). The second, subsidiary conductor flanks the shear zone nearby to the west.

The large resistor east of Mount St Helens confines the large conductor further east to be in the Mount Adams area, providing better resolution than prior 3-D images based just on regional tipper data (Egbert & Booker 1993). The NNW-SSE limits of the resistor cannot be considered as well-resolved, however, without site coverage. At lower crustal depths (27 km in Fig. 19), resistivity under

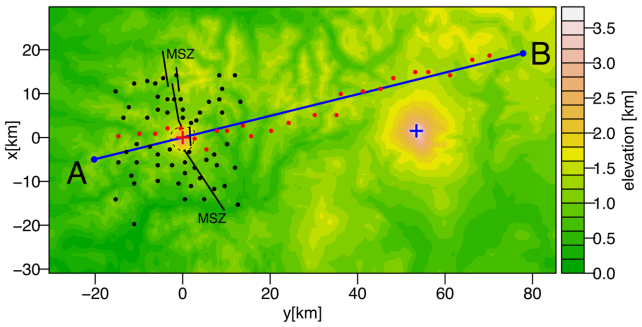

Figure 15. Mount St Helens inversion model. Contour plot of topography of the central part of the domain is presented. Coordinate (0, 0) corresponds to the location of Mount St Helens peak, marked by a red cross. Blue cross denotes Mount Adams. Blue line denotes profile A–B used in Fig. 18. MT receiver locations are marked by black and red dots. Red dots denote receivers used in the 2-D inversion of Hill *et al.* (2009). Mount St Helens shear zone (MSZ) after Lagmay *et al.* (2000).

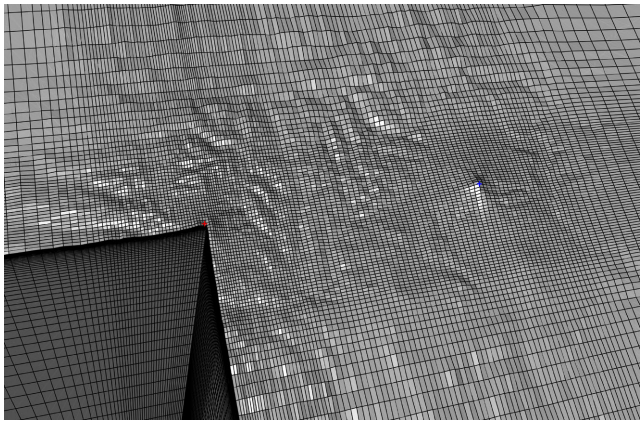

Figure 16. Central part of the mesh for the Mount St Helens inversion model. Blue and red crosses denote Mount Adams and Mount St Helens peaks, respectively.

Mount St Helens decreases from west to east as in Hill *et al.* (2009) and the low is somewhat elongate toward the south–southeast. On the other hand, low deep crustal resistivity under Mount Adams expands to the north. It is tempting to assign this geometry to an offset in lower crustal magmatic underplating associated with the E-W offset in the Cascade volcanic chain at this latitude. However, such conjecture should await better resistivity structural constraints from further 3-D MT coverage both north and south of the current data set.

Finally, in Fig. 20, we show a 3 Ωm isosurface within the Mount St Helens model viewed from the east with conductive material around Mount Adams excluded. It represents the conductive upper reaches of the MSZ. The top of the main surface is only slightly undulatory along its north–south extent. A few steep, narrow conductors projecting upward mainly to the north of the mount itself could represent local fluidized damage zones but do not obviously correspond to a central volcanic conduit (e.g. Musumeci *et al.* 2002).

6 CONCLUSIONS

As other researchers are finding as well, direct solutions to various aspects of the diffusive EM inversion problem are becoming

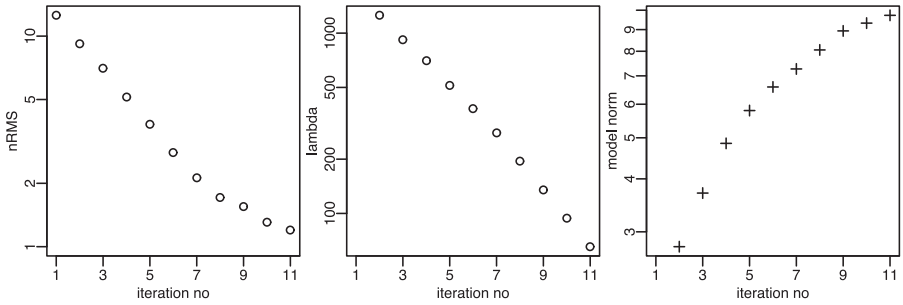

Figure 17. Values of nRMS, λ and model norm as a function of iteration number for the Mount St Helens inversion.

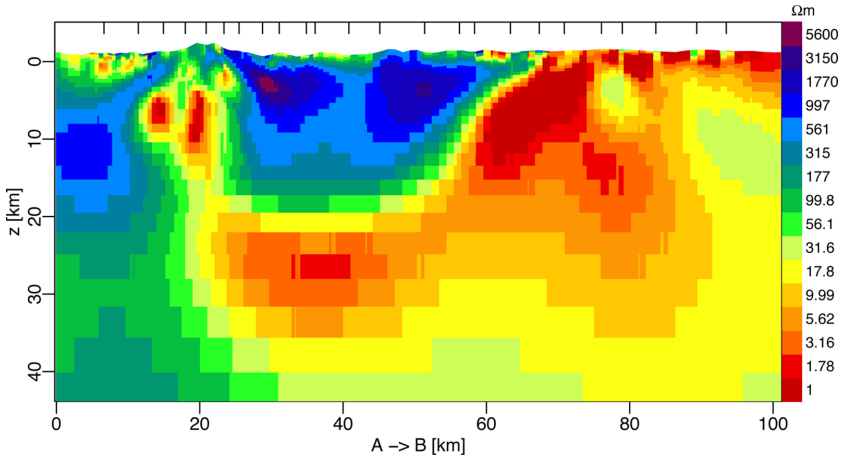

Figure 18. Cross-section of Mount St Helens inversion at iteration 11 along profile A–B marked on Fig. 15. Black ticks at the top denote the locations of receivers plotted in red on Fig. 15 that were used in the 2-D inversion of Hill *et al.* (2009).

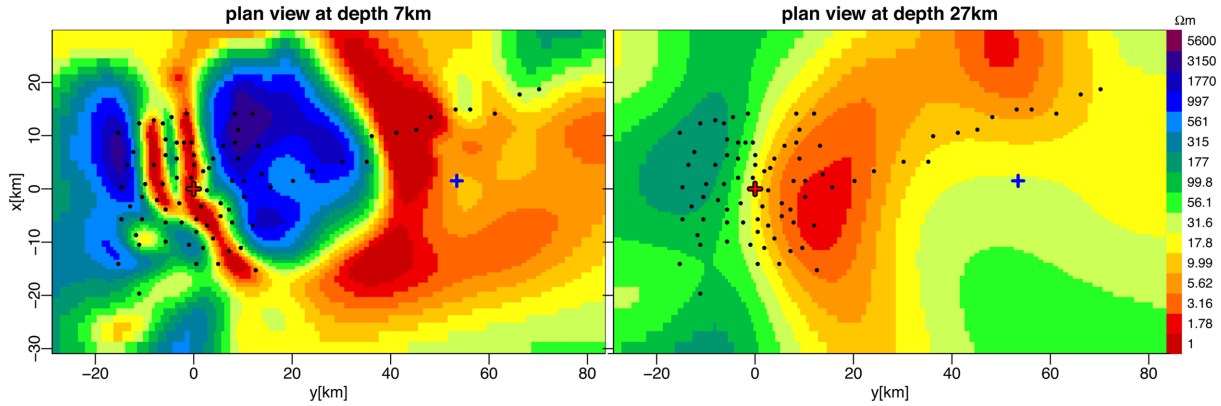

Figure 19. Plan views of Mount St Helens inversion model 11. Receivers' locations marked by black dots, Mount St Helens peak by red cross and Mount Adams peak by blue cross.

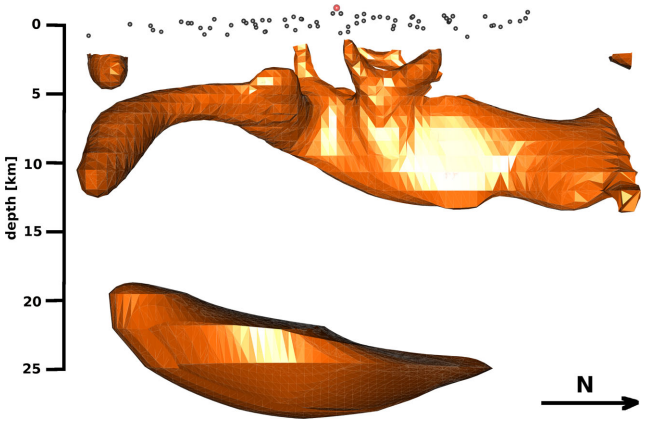

Figure 20. 3-D view from the East onto the 3 Ωm isosurface below Mount St Helens. A region (−25 km, 25 km) × (−24 km, 19 km) around St Helens only is shown, so the conductors below Mount Adams are not seen. Only structures deeper than 2 km are shown. Red circle denotes Mount St Helens peak, black circles denote locations of the receivers around the mountain.

increasingly practical. Here we have shown that direct solvers can effectively handle the Gauss–Newton update for inverse problems approaching one million parameters with parallelization on multicore SMP workstations and large RAM if the model update is formulated in data space. In this case, the limiting computational cost both in run-time and memory is the forward problem (including Jacobians), which can be computed effectively using MKL PARDISO. Finite-element models of order 176 × 176 × 70 elements fill half the memory of a workstation with 0.5 TB RAM but such meshes can, for example, fit large MT data sets of 400 sites with six columns of parameters between sites in both *x*- and *y*-directions with padding of nearly 30 expanding element columns around the mesh edges. We have not experienced system conditioning problems due to high element aspect ratios with our direct solutions.

Single-box SMP workstation capabilities continue to progress, with platforms holding up to 4 TB RAM available at the time of this writing. The overall scalability of MKL PARDISO is good on multicore shared memory systems and may be expected to do well on machines with more cores. Another option could be to construct a distributed cluster whose nodes were large-RAM multicore machines such as we employed herein each devoted to a different response frequency, although at considerably greater hardware investment. Finally, we find that the deformable hexahedral mesh framework lends a predictability to mesh design and performance of libraries such as MKL PARDISO that should offset concerns that the geometries of simulation with such a mesh may not be as arbitrary as is possible with assemblies of tetrahedra. More research is warranted, however, into optimal inversion regularization functionals and methods for guaranteeing rapid convergence.

ACKNOWLEDGEMENTS

We acknowledge the support of this work from U.S. Department of Energy under contract DE-EE0002750 and the U.S. National Science Foundation under grant AES-1443522 to PW. EC acknowledges the partial support of the U.S. National Science Foundation through grants ARC-0934721 and DMS-1413454. GH acknowledges the support of both an MIPRS and MGS award through Monash University and the support of the Royal Society of New Zealand Marsden Fund award ASL-1301. Presentation and content of the paper were improved substantially following the remarks of three anonymous reviewers. The submission was handled by Associate Editor Ute Weckmann.

REFERENCES

Avdeeva, A., Moorkamp, M., Avdeev, D., Jegen, M. & Miensopust, M., 2015. Three-dimensional inversion of magnetotelluric impedance tensor data and full distortion matrix, *Geophys. J. Int.,* **202**(1), 464–481.

Baboulin, M., Giraud, L. & Gratton, S., 2005. A parallel distributed solver for large dense symmetric systems: applications to geodesy and electromagnetism problems, *Int. J. High Perform. Comput. Appl.,* **19**(4), 353–363.

Baboulin, M., Becker, D. & Dongarra, J., 2011. A parallel tiled solver for dense symmetric indefinite systems on multicore architectures, *Technical Rep.*, University of Tennessee Computer Science, ICL-UT-11-07.

Buttari, A., Langou, J., Kurzak, J. & Dongarra, J., 2009. A class of parallel tiled linear algebra algorithms for multicore architectures, *Parallel Computing*, **35**, 38–53.

Commer, M. & Newman, G.A., 2008. New advances in three-dimensional controlled-source electromagnetic inversion, *Geophys. J. Int.,* **172,** 513–535.

Constable, S.C., Parker, R.L. & Constable, C.G., 1987. Occam's inversion: a practical algorithm for generating smooth models from electromagnetic sounding data, *Geophysics,* **52**(3), 289–300.

deGroot-Hedlin, C. & Constable, S., 1990. Occam's inversion to generate smooth, two-dimensional models from magnetotelluric data, *Geophysics,* **55**(12), 1613–1624.

DeSiena, L., Thomas, C., Waite, G., Moran, S. & Klemme, S., 2014. Attenuation and scattering tomography of the deep plumbing system of mount st. helens, *J. geophys. Res.: Solid Earth,* **119**(11), 8223–8238.

Egbert, P.G.D. & Booker, J.R., 1993. Imaging crustal structure in southwestern Washington with small magnetometer arrays, *J. geophys. Res.,* **98,** 15 967–15 985.
Grayver, A.V., Streich, R. & Ritter, O., 2013. Three-dimensional parallel distributed inversion of CSEM data using a direct forward solver, *Geophys. J. Int.,* **193,** 1432–1446.
Groom, R.W. & Bahr, K., 1992. Corrections for near surface effects: decomposition of the magnetotelluric impedance tensor and scaling corrections for regional resistivities: a tutorial, *Surv. Geophys.,* **13**(4–5), 341–379.
Haber, E., Oldenburg, D.W. & Shekhtman, R., 2007. Inversion of time domain three-dimensional electromagnetic data, *Geophys. J. Int.,* **171**(2), 550–564.
Hill, G.J., Caldwell, T.G., Heise, W., Chertkoff, D.G., Bibby, H.M., Burgess, M.K., Cull, J.P. & Cass, R.A.F., 2009. Distribution of melt beneath Mount St Helens and Mount Adams inferred from magnetotelluric data, *Nat. Geosci.,* **2,** 785–789.
Hohmann, G.W. & Raiche, A.P., 1988. Inversion of controlled-source electromagnetic data, in *Electromagnetic Methods in Applied Geophysics*, Vol. 1, pp. 469–503, ed. Nabighian, M.N., Soc. Expl. Geophys., Tulsa, OK.
Key, K. & Constable, S., 2011. Coast effect distortion of marine magnetotelluric data: insights from a pilot study offshore northeastern Japan, *Phys. Earth planet. Inter.,* **184,** 194–207.
Kordy, M., Maris, V., Wannamaker, P. & Cherkaev, E., 2013. 3-D edge finite element solution for scattered electric field using a direct solver parallelized on an SMP workstation, in *5th International Symposium on Three-Dimensional Electromagnetics,* Sapporo, May 7–9, p. 4.
Kordy, M., Wannamaker, P., Maris, V., Cherkaev, E. & Hill, G.J., 2015. 3-dimensional magnetotelluric inversion including topography using deformed hexahedral edge finite elements and direct solvers parallelized on SMP computers, Part I: forward problem and parameter Jacobians, *Geophys. J. Int.,* doi:10.1093/gji/ggv410.
Lagmay, A. M.F., van Wyk de Vries, B., Kerle, N. & Pyle, D.M., 2000. Volcano instability induced by strike-slip faulting, *Bull. Volc.,* **62,** 331–346.
Levenberg, K., 1944. A method for the solution of certain non-linear problems in least squares, *Q. appl. Math.,* **2,** 164–168.
Liu, J., Brio, M. & Moloney, J., 2009. Overlapping Yee FDTD method on nonorthogonal grids, *J. Sci. Comput.,* **39**(1), 129–143.
Maris, V. & Wannamaker, P.E., 2010. Parallelizing a 3-D finite difference MT inversion algorithm on a multicore PC using OpenMP, *Comput. Geosci.,* **36**(10), 1384–1387.
Meqbel, N.M., Egbert, G.D., Wannamaker, P.E., Kelbert, A. & Schultz, A., 2014. Deep electrical resistivity structure of the northwestern U.S. derived from 3-D inversion of USArray magnetotelluric data, *Earth planet. Sci. Lett.,* **402,** 290–304.
Miensopust, M.P., Queralt, P., Jones, A.G. & the 3-D Modelers, 2013. Magnetotelluric 3-D inversion—a review of two successful workshops on forward and inversion code testing and comparison, *Geophys. J. Int.,* **193,** 1216–1238.
Musumeci, C., Gresta, S. & Malone, S.D., 2002. Magma system recharge of Mount St. Helens from precise relative hypocenter location of microearthquakes, *J. geophys. Res.: Solid Earth (1978–2012),* **107**(B10), ESE 16-1–ESE 16-9.
Nocedal, J. & Wright Stephen, J., 2006. *Numerical Optimization,* Springer.
Oldenburg, D.W., Haber, E. & Shekhtman, R., 2013. Three dimensional inversion of multi-source time domain electromagnetic data, *Geophysics,* **78**(1), E47–E57.
Parker, R.L., 1994. *Geophysical Inverse Theory, Princeton University Press*, Princeton, 386 pp.
Sasaki, Y., 2001. Full 3-D inversion of electromagnetic data on PC, *J. appl. Geophys.,* **46,** 45–54.
Schwarzbach, C. & Haber, E., 2013. Finite element based inversion for time-harmonic electromagnetic problems, *Geophys. J. Int.,* **193,** 615–634.
Siripunvaraporn, W. & Egbert, G., 2000. An efficient data-subspace inversion method for 2-D magnetotelluric data, *Geophysics,* **65,** 791–803.
Siripunvaraporn, W., Egbert, G., Lenbury, Y. & Uyeshima, M., 2005a. Three-dimensional magnetotelluric inversion: data-space method, *Phys. Earth planet. Inter.,* **150,** 3–14.
Siripunvaraporn, W., Egbert, G. & Uyeshima, M., 2005b. Interpretation of two-dimensional magnetotelluric profile data with three-dimensional inversion: synthetic examples, *Geophys. J. Int.,* **160**(3), 804–814.
Stanley, W.D., Johnson, S.Y., Qamar, A.Y., Weaver, C.S. & Williams, J.M., 1996. Tectonics and seismicity of the southwest Washington Cascade Range, *Bull. seism. Soc. Am.,* **86,** 1–18.
Stark, M.A., Soyer, W., Hallinan, S. & Watts, M.D., 2013. Distortion effects on magnetotelluric sounding data investigated by 3d modeling of high-resolution topography, *Geotherm. Res. Counc. Trans.,* **37,** 521–527.
Usui, Y., 2015. 3-D inversion of magnetotelluric data using unstructured tetrahedral elements: applicability to data affected by topography, *Geophys. J. Int.,* **202**(2), 828–849.
Wannamaker, P., Stodt, J. & Rijo, L., 1986. Two-dimensional topographic responses in magnetotelluric modeling using finite elements, *Geophysics,* **51,** 2131–2144.
Wannamaker, P.E., Evans, R.L., Bedrosian, P.A., Unsworth, M.J., Maris, V. & McGary, R.S., 2014. Segmentation of plate coupling, fate of subduction fluids, and modes of arc magmatism in Cascadia, inferred from magnetotelluric resistivity, *Geochem. Geophys. Geosyst.,* **15**(11), 4230–4253.
Weaver, C.S., Grant, W.C. & Shemeta, J.E., 1987. Local crustal extension at Mount St. Helens, Washington, *J. geophys. Res.: Solid Earth (1978–2012),* **92**(B10), 10 170–10 178.
Yi, M.J., Kim, J.H. & Chung, S.H., 2003. Enhancing the resolving power of least-squares inversion with active constraint balancing, *Geophysics,* **68**(3), 931–941.
Zhdanov, M.S., 2002. *Geophysical Inverse Theory and Regularization Problems,* Elsevier.
Zhdanov, M.S., Wan, L., Gribenko, A., Cuma, M., Key, K. & Constable, S., 2011. Large-scale 3-D inversion of marine magnetotelluric data: case study from the Gemini prospect, Gulf of Mexico, *Geophysics,* **76,** F77–F87.

SUPPORTING INFORMATION

Additional Supporting Information may be found in the online version of this paper:

Figure 1. Real and imaginary induction vectors for the measured data and the prediction by the model obtained in the Mount St Helens inversion for five frequencies between 1 Hz and 0.01 Hz. Parkinson convention is used.
Figure 2. nRMS for each component of the MT response and for each receiver for the final model of Mount St Helens inversion.
Table 1. Table of nRMS as a function of frequency for the starting model and the final model for Mount St Helens inversion.
(http://gji.oxfordjournals.org/lookup/suppl/doi:10.1093/gji/ggv411/-/DC1).

Please note: Oxford University Press is not responsible for the content or functionality of any supporting materials supplied by the authors. Any queries (other than missing material) should be directed to the corresponding author for the paper.

APPENDIX A: APPROXIMATION OF REGULARIZATION NORMS

Here, we present how we approximate norms $\|\nabla(m - m_0)\|_{L_2(1)}$,$\|\nabla(m - m_0)\|_{L_2(\|S\|_2)}$,$\|\nabla(m - m_0)\|_{L_2\left(\frac{1}{\|S\|_2}\right)}$. For simplicity we will write m instead of $m - m_0$.

Assume that the discrete m is a representation of an infinite-dimensional model, that is, a function $m(\mathbf{r})$ defined for every location $\mathbf{r}$ in the subsurface part of Ω. If the discrete norms $\|m\|_{L_2(v)}$ and $\|\nabla m\|_{L_2(v)}$ are defined as the norms of the infinite-dimensional model, they have the property that they are mesh independent. If one considers two different meshes with two different discrete

representations of the same infinite-dimensional model $m(\mathbf{r})$, the two norms on different meshes will be equal, as they are equal to the norm of the infinite-dimensional model.

In the case of the norm $\|m\|_{L_2(\nu)}$ one can think of the infinite-dimensional model $m(\mathbf{r})$ being piecewise constant, that is, $m(\mathbf{r}) = m_j$ whenever $\mathbf{r}$ is inside an inversion cell V_j. In such a case, if a mesh is refined and the value of the model at an inversion cell is passed on to the subcells that the cell is split to, then the infinite-dimensional model remains the same. In the case of the norm $\|\nabla(m)\|_{L_2(\nu)}$ one cannot think of the infinite-dimensional model being piecewise constant as the gradient of such a model does not exist (the gradient is not a square integrable vector field). The infinite-dimensional model should be continuous. In 1-D one could think of a model that is piecewise linear between the centres of inversion cells.

First we will consider norms $\|m\|_{L_2(1)}$, $\|m\|_{L_2(\|S\|_2)}$, $\|m\|_{L_2\left(\frac{1}{\|S\|_2}\right)}$. To approximate them, we will take norm of the form:

$$\|m\|^2_{B_m} = m^T B_m m \tag{A1}$$

with appropriate matrix B_m, where $m = (m)_{j=1}^{N_m}$ is a vector of $\log_{10}$ resistivities of inversion cells.

If one takes B_m to be a diagonal matrix with entries w_j equal to volumes of inversion cells:

$$w_j = \#V_j = \int_{V_j} d\mathbf{r} \tag{A2}$$

then one obtains a model norm $\|m\|_{B_m}$ that is equal to the $L_2(1)$ norm of the piecewise constant model $m(\mathbf{r})$:

$$\begin{aligned}\|m\|^2_{B_m} &= \sum_{j=1}^{N_m} m_j^2 B_m(j,j) = \sum_{j=1}^{N_m} m_j^2 \#V_j \\ &= \sum_{j=1}^{N_m} \int_{V_j} m(\mathbf{r})^2 d\mathbf{r} = \int_{\Omega} m(\mathbf{r})^2 d\mathbf{r} \\ &= \|m\|^2_{L_2(1)}\end{aligned} \tag{A3}$$

Consider the derivative S of infinite-dimensional problem defined at (21). Assuming that the discretization of the domain is fine enough so that the finite-dimensional approximation of the problem is close to the infinite-dimensional problem, using F for finite-dimensional response, one could write that the jth column of Jacobian matrix J is:

$$J_{\cdot j} = \frac{\partial F}{\partial m_j} = \int_{V_j} S(\mathbf{r}) d\mathbf{r} \tag{A4}$$

where V_j is a j-th inversion cell. If we assume that the inversion cell V_j is small enough that $S(\mathbf{r}) \approx S_j = \text{const}$ for $\mathbf{r} \in V_j$, then a sensitivity of inversion cell V_j is obtained:

$$\begin{aligned}w_j &= \sqrt{\sum_{i=1}^{N_d} J_{ij}^2} = \sqrt{J_{\cdot j}^T J_{\cdot j}} = \|J_{\cdot j}\|_2 = \left\| \int_{V_j} S(\mathbf{r}) d\mathbf{r} \right\|_2 \\ &\approx \|\#V_j S_j\|_2 = \#V_j \|S_j\|_2 = \int_{V_j} \|S_j\|_2 d\mathbf{r} \\ &\approx \int_{V_j} \|S(\mathbf{r})\|_2 d\mathbf{r}\end{aligned} \tag{A5}$$

If we define B_m to be a diagonal matrix with w_j as entries, then

$$\begin{aligned}\|m\|^2_{B_m} &= \sum_{j=1}^{N_m} m_j^2 w_j \approx \sum_{j=1}^{N_m} m_j^2 \int_{V_j} \|S(\mathbf{r})\|_2 d\mathbf{r} \\ &= \int_{\Omega} \|m(\mathbf{r})\|_2^2 \|S(\mathbf{r})\|_2 d\mathbf{r} \\ &= \|m\|^2_{L_2(\|S\|_2)}.\end{aligned} \tag{A6}$$

The regularization norm is approximately equal to the weighted L_2 norm with $\|S\|_2$ as a weight. Note also that to calculate $w_j = \|J_j\|_2$ one does not need to know the cell volume, only Jacobian matrix J is used. This regularization was considered in Zhdanov (2002) (see eq. 3.89).

The third weight we consider is defined as

$$w_j = \frac{(\#V_j)^2}{\sqrt{J_{\cdot j}^T J_{\cdot j}}} \approx \frac{(\#V_j)^2}{\#V_j \|S_j\|_2} = \#V_j \frac{1}{\|S_j\|_2} \tag{A7}$$

The corresponding norm of the model is approximately

$$\begin{aligned}\|m\|^2_{B_m} &= \sum_{j=1}^{N_m} m_j^2 w_j \approx \sum_{j=1}^{N_m} m_j^2 \#V_j \frac{1}{\|S_j\|_2} \\ &\approx \sum_{j=1}^{N_m} m_j^2 \int_{V_j} \frac{1}{\|S(\mathbf{r})\|_2} d\mathbf{r} \\ &= \int_{\Omega} \|m(\mathbf{r})\|_2^2 \frac{1}{\|S(\mathbf{r})\|_2} d\mathbf{r} \\ &= \|m\|^2_{L_2\left(\frac{1}{\|S\|_2}\right)}\end{aligned} \tag{A8}$$

The norm is approximately equal to the weighted L_2 norm with $\frac{1}{\|S\|_2}$ as a weight. This norm will suppress model change in regions with low sensitivity, using the reasoning that if we cannot detect the properties of a region well, we will make it similar to its surroundings. This is similar to the approach of Yi *et al.* (2003).

To get an approximation of a norm of the model gradient, rather than of the model, so a norm that resembles $\|\nabla m\|_{L_2(\nu)}$ rather than $\|m\|_{L_2(\nu)}$ in essence one should think of an infinite-dimensional continuous model $m(\mathbf{r})$ that is represented by the discrete model m and calculate the $L^2(\nu)$ norm of its gradient. For simplicity though, we do not pursue this approach and we use a simple finite-difference approximation calculated as if the topography was not present and the element layers were horizontal. Assume that each inversion cell consists of one finite element. Air layers as well as one layer of elements close to the boundary $\partial\Omega$ are not used in the inversion. One layer close to the boundary has a fixed conductivity equal to the conductivity of the 1-D layered Earth primary model. This is done to prevent us from having a non-zero source term J^{imp} very close to the boundary. As a result the inversion cells can be addressed using three indices $i_x = 1, \ldots, n_x, i_y = 1, \ldots, n_y, i_z = 1, \ldots, n_z$, where the total number of inversion cells is $N_m = n_x n_y n_z$. Matrix B_m is such that

$$\begin{aligned}\|m\|^2_{B_m} = &\sum_{i_x=2}^{n_x} \sum_{i_y=1}^{n_y} \sum_{i_z=1}^{n_z} \tilde{w}^x_{i_x,i_y,i_z} \left(\frac{m_{i_x,i_y,i_z} - m_{i_x-1,i_y,i_z}}{x_{i_x,i_y,i_z} - x_{i_x-1,i_y,i_z}} \right)^2 \\ &+ \sum_{i_x=1}^{n_x} \sum_{i_y=2}^{n_y} \sum_{i_z=1}^{n_z} \tilde{w}^y_{i_x,i_y,i_z} \left(\frac{m_{i_x,i_y,i_z} - m_{i_x,i_y-1,i_z}}{y_{i_x,i_y,i_z} - y_{i_x,i_y-1,i_z}} \right)^2 \\ &+ \sum_{i_x=1}^{n_x} \sum_{i_y=1}^{n_y} \sum_{i_z=2}^{n_z} \tilde{w}^z_{i_x,i_y,i_z} \left(\frac{m_{i_x,i_y,i_z} - m_{i_x,i_y,i_z-1}}{z_{i_x,i_y,i_z} - z_{i_x,i_y,i_z-1}} \right)^2\end{aligned}$$

where

$$\tilde{w}^x_{i_x,i_y,i_z} = \frac{w_{i_x-1,i_y,i_z} + w_{i_x,i_y,i_z}}{2}$$

$$\tilde{w}^y_{i_x,i_y,i_z} = \frac{w_{i_x,i_y-1,i_z} + w_{i_x,i_y,i_z}}{2}$$

$$\tilde{w}^z_{i_x,i_y,i_z} = \frac{w_{i_x,i_y,i_z-1j} + w_{i_x,i_y,i_z}}{2} \tag{A9}$$

and

$$\left[x_{i_x,i_y,i_z}, y_{i_x,i_y,i_z}, z_{i_x,i_y,i_z}\right]$$

is the location of the centre of mass of the inversion cell denoted by i_x, i_y, i_z.

Using the procedure described above with w given by (A5), (A2) or (A7) one gets norms of model m resembling $\|\nabla m\|_{L_2(\|S\|_2)}$, $\|\nabla m\|_{L_2(1)}$ and $\|\nabla m\|_{L_2\left(\frac{1}{\|S\|_2}\right)}$, respectively. Those norms are used for regularization and the inversion results are compared.

APPENDIX B: INVERSION FOR STATIC DISTORTION MATRICES

We present the inversion for the impedance static distortion matrices similar to the approach of Avdeeva *et al.* (2015). Shallow conductivity structure causes a static distortion of the impedance such that

$$Z^{\text{obs}}_k(\omega) = C_k Z_k(\omega) \tag{B1}$$

where Z_k is the impedance without the shallow conductivity structure and Z^{obs}_k is the impedance with the shallow conductivity structure. Matrix $C_k \in \mathbb{R}^{2\times 2}$ is real valued and not dependent on frequency, yet different for each receiver $k = 1, \ldots, N_{\text{rec}}$ (see Avdeeva *et al.* 2015).

In the inversion procedure, apart from calculating the unknown model $m = (m_j)_{j=1}^{N_m}$ of $\log_{10}$ resistivities, we invert also for real valued matrices $C = (C_k)_{k=1}^{N_{\text{rec}}}$, one for each receiver location.

The forward problem response $F(m)$, defined by (5), is modified by applying (B1) to obtain $F(m, C)$. The regularized functional to be minimized changes from (8) by adding squares of Frobenius norms $\|.\|_F$ of the difference between distortion matrices C_k and identity matrix I, yielding:

$$\tilde{W}(m, C) = (F(m, C) - d)^T B_d (F(m, C) - d) + \lambda(m - m_0)^T B_m (m - m_0) + \tau \sum_{k=1}^{N_{\text{rec}}} \|C_k - I\|_F^2 \tag{B2}$$

Note that if we define $\tilde{N}_m = N_m + 4N_{\text{rec}}$,

$$\begin{aligned}
\tilde{m} = (\tilde{m}_k)_{k=1}^{\tilde{N}_m} = \; & (m_1, \ldots, m_{N_m}, \\
& C_{1,xx}, C_{1,yx}, C_{1,yx}, C_{1,yy}, \ldots, \\
& C_{N_{\text{rec}},xx}, C_{N_{\text{rec}},yx}, C_{N_{\text{rec}},yx}, C_{N_{\text{rec}},yy}) \\
\tilde{m}_0 = (\tilde{m}_{k,0})_{k=1}^{\tilde{N}_m} = \; & (m_{1,0}, \ldots, m_{N_m,0}, \\
& 1, 0, 0, 1, \ldots, \\
& 1, 0, 0, 1)
\end{aligned}$$

$$\tilde{B}_m = \begin{bmatrix} B_m & 0 \\ 0 & \frac{\tau}{\lambda} I \end{bmatrix}$$

Then (B2) may be written in the form similar to (8):

$$\tilde{W}(\tilde{m}) = (F(\tilde{m}) - d)^T B_d (F(\tilde{m}) - d) + \lambda(\tilde{m} - \tilde{m}_0)^T \tilde{B}_m (\tilde{m} - \tilde{m}_0)$$

Jacobian $\tilde{J}$ of the forward response $F(\tilde{m})$ may be easily obtained from J using chain rule. As a result one can apply Gauss–Newton and data-space Gauss–Newton procedure similarly to the case of inversion for m only.

Similarly to Avdeeva *et al.* (2015), we use $\tau = 0.01$. Note that this value of τ is very small, giving almost no regularization for distortion matrices term in (B2). Yet it is enough to obtain good models, if only the starting model is not far from the true model. It is our experience so far that using the starting model that was obtained in the inversion without the distortion matrix yields good results. On the other hand, if one starts from a half-space that is far from the true model, the iteration may not converge to a plausible model. In this case, we have seen the matrices C converge to 0.

Geophysical Journal International

Geophys. J. Int. (2016) **204,** 74–93 doi: 10.1093/gji/ggv410

GJI Geomagnetism, rock magnetism and palaeomagnetism

3-D magnetotelluric inversion including topography using deformed hexahedral edge finite elements and direct solvers parallelized on SMP computers – Part I: forward problem and parameter Jacobians

M. Kordy,[1,2] P. Wannamaker,[2] V. Maris,[2] E. Cherkaev[1] and G. Hill[3]

[1]*Department of Mathematics at the University of Utah,* 155 *S* 1400 *E Room* 233, *Salt Lake City, UT* 84112-0090, *USA. E-mail: kordy@math.utah.edu*

[2]*Energy and Geoscience Institute at the University of Utah,* 423 *Wakara Way, Suite* 300, *Salt Lake City, UT* 84108, *USA*

[3]*Gateway Antarctica, University of Canterbury, Private Bag* 4800 *Christchurch* 8140 *and Antarctica Scientific Limited, Unit* 5*E*/39 *Taranaki Street Wellington* 6011

Accepted 2015 September 23. Received 2015 September 22; in original form 2014 November 3

SUMMARY

We have developed an algorithm, which we call HexMT, for 3-D simulation and inversion of magnetotelluric (MT) responses using deformable hexahedral finite elements that permit incorporation of topography. Direct solvers parallelized on symmetric multiprocessor (SMP), single-chassis workstations with large RAM are used throughout, including the forward solution, parameter Jacobians and model parameter update. In Part I, the forward simulator and Jacobian calculations are presented. We use first-order edge elements to represent the secondary electric field (E), yielding accuracy $O(h)$ for E and its curl (magnetic field). For very low frequencies or small material admittivities, the E-field requires divergence correction. With the help of Hodge decomposition, the correction may be applied in one step after the forward solution is calculated. This allows accurate E-field solutions in dielectric air. The system matrix factorization and source vector solutions are computed using the MKL PARDISO library, which shows good scalability through 24 processor cores. The factorized matrix is used to calculate the forward response as well as the Jacobians of electromagnetic (EM) field and MT responses using the reciprocity theorem. Comparison with other codes demonstrates accuracy of our forward calculations. We consider a popular conductive/resistive double brick structure, several synthetic topographic models and the natural topography of Mount Erebus in Antarctica. In particular, the ability of finite elements to represent smooth topographic slopes permits accurate simulation of refraction of EM waves normal to the slopes at high frequencies. Run-time tests of the parallelized algorithm indicate that for meshes as large as $176 \times 176 \times 70$ elements, MT forward responses and Jacobians can be calculated in $\sim$1.5 hr per frequency. Together with an efficient inversion parameter step described in Part II, MT inversion problems of 200–300 stations are computable with total run times of several days on such workstations.

Key words: Numerical approximations and analysis; Electrical properties; Magnetotelluric; Geomagnetic induction; Physics of magma and magma bodies; Antarctica.

1 INTRODUCTION

Impressive progress has been made over the past several years in the simulation and inversion of three-dimensional (3-D) diffusive electromagnetic (EM) responses for earth electrical resistivity structure. Most approaches have adopted finite difference or finite element (FE) numerical methods although the integral equations technique also has been utilized (see reviews by Börner 2010; Everett 2012). An effective simulation and inversion algorithm needs to handle a large range of structural scales due to possibly complex resistivity distributions and the wide frequency bandwidth of survey techniques (e.g. potentially seven or more orders of magnitude in magnetotellurics (MTs); Chave & Jones 2012). Furthermore, in many orogenic or resource settings, the earth's surface can show considerable topographic variation which will have its own EM response and introduces vertical variation of receiver placement with respect to subsurface structure.

To include topography in earth resistivity models, we pursue the FE method. FEs allow for a relatively smooth representation of topography. Although it is possible to consider finite difference or finite volume discretization on unstructured (i.e. non stair-stepped) meshes (Hyman & Shashkov 1999; Liu *et al.* 2009; Jahandari & Farquharson 2014), it may lead to spurious modes in the solution (see a discussion in Hyman & Shashkov 1999), late time instability

(see a discussion in Liu *et al.* 2009) or geometric restrictions on the grid (Liu *et al.* 2009). Proper discretization of the operators ∇, $\nabla \times$ and $\nabla \cdot$ that are important in Maxwell's equations (Hyman & Shashkov 1999) is a challenge for unstructured meshes. Edge elements, considered in this paper, respect the relationship between those operators, expressed by an algebraic topology structure called de Rham diagram (Gunzburger & Bochev 2009), which allows us to apply the divergence correction in a natural way.

Several authors have considered the choice between tetrahedral and hexahedral elements for including topography (e.g. daSilva *et al.* 2012; Lelièvre & Farquharson 2013; Schwarzbach & Haber 2013), with tetrahedra argued by some to allow a more arbitrary discretization of structure. However, we will show that much can be accomplished using hexahedra, and their simpler implementation in both the forward and inverse modules helps to keep computer resources manageable and may facilitate wider transfer of technique within the EM community. We solve for the electric field through the governing Helmholtz equation, so edge FEs are used (lowest order type) (Nédélec 1986). These conforming elements allow field discontinuities normal to conductivity interfaces to be represented but preserve continuity of the tangential field component. FEs do not invoke material averaging procedures across cell boundaries as is done in staggered grid finite difference schemes (daSilva *et al.* 2012) so there is no question about the placement of sharp interfaces.

The design factors cited above can put high demands upon mesh discretization and computing resources for larger data sets. Because of such demands, especially memory, iterative solutions have dominated the literature heretofore (Haber *et al.* 2007; Börner *et al.* 2008; Commer & Newman 2008; Um *et al.* 2012, and many others). Since at least the work of Pridmore *et al.* (1981), however, iterative forward solvers are known to become ill-conditioned and slow to converge if grid cell aspect ratios grow to be extreme. Moreover, iterative solutions for the Helmholtz equation require careful preconditioning and even so may sometimes fail to converge (also see Grayver *et al.* 2013). They become expensive when many right-hand source vectors are needed, such as in controlled-source applications or the inversion approach we describe, as each source requires the work of a full simulation. Conditioning issues may apply as well to iteratively solving normal equations in the inversion parameter step (*op. cit.*).

Recent advances in computing power, especially emergence of less expensive many-core, symmetric multiprocessor (SMP) workstations with substantial RAM, have motivated us to implement direct solvers both for the forward model responses and for Gauss–Newton inversion parameter steps. This is intended to produce a practical 3-D inversion code incorporating topography that can handle moderately large data sets on an affordable, single-box computer format. We find that accurate solutions for meshes with large element aspect ratios having run times nearly independent of frequency are possible. The solution of hundreds of source vectors at the cost of factoring the forward system matrix allows explicit calculation of parameter Jacobians accurately and efficiently, as has been applied for some time with the 2-D problem (e.g. deGroot-Hedlin & Constable 1990; deLugao & Wannamaker 1996; Key & Constable 2011).

We certainly are not the first to examine direct solutions for 3-D problems. Streich (2009) created a staggered-grid finite difference algorithm with a direct solver for simulating marine controlled source electromagnetic (CSEM) responses. Oldenburg *et al.* (2008, 2013) used a direct solver in their finite difference H-field simulator for time domain electromagnetic (TDEM) inversion and Um *et al.* (2015) used a mixed direct-iterative solution to model well casing effects with FEs. daSilva *et al.* (2012) utilized rectilinear edge FEs in forward modelling of seafloor CSEM models while Ren *et al.* (2013) considered a direct solver for tetrahedral meshes. Grayver *et al.* (2013) incorporated Streich's solver to compute forward responses and parameter Jacobians explicitly and create an inversion algorithm where the parameter step was estimated using a pre-conditioned conjugate gradient (PCG) scheme. Schwarzbach & Haber (2013) developed an unstructured mesh of tetrahedra with the forward problem solved directly and the parameter step computed via PCG or iterative quasi-Newton method. Usui (2015) solved MT responses directly using a tetrahedral mesh and developed an inversion code with direct solution of the parameter step in model space.

In Part I of our contribution, we apply a direct solver to edge FE equations of a deformed hexahedral mesh and verify that accurate responses are achieved for subsurface and topographic structure. Good responses are obtained also in the dielectric air portion of the model after applying a divergence correction. Parameter Jacobians are computed accurately and efficiently in the direct framework exploiting reciprocity. Moderately large meshes can be computed in what we believe are practical run times. In Part II, forward simulations are used together with MT data to form normal equations for a regularized inversion step. We investigate the data space (Siripunvaraporn *et al.* 2005) formulations of the step and confirm that it can handle significant parameter sets. We invert a well-known field data set to demonstrate algorithm performance in real-world settings. The HexMT algorithm, is parallelized for widely available, server-class SMP workstations.

2 FINITE ELEMENT FORMULATION

For representing structure with topography, we use an FE mesh such as in Fig. 1. Corners of elements at the air-earth interface (surface) are adjusted vertically to represent elevation changes. This is similar to the fashion of Nam *et al.* (2007). Sub- and superajacent element layers are moved similarly but with steadily diminishing magnitude away from the surface until upper and lower datum planes are reached. Beyond those planes, the element layers remain flat. The height and depth of these planes from the background air-earth interface typically is several times the maximal topographic model relief to allow the elements to be close to parallelepipeds in shape. If there are elements that are not close to parallelepipeds, the order of convergence versus discretization may be reduced (see Falk *et al.* 2011).

Formally, the spatial domain of Fig. 1 is a cuboid Ω, whose top portion is air ($\sigma = 0$) and whose lower portion is earth's subsurface ($\sigma > 0$) which may exhibit topography in its central portion. We assume that the conductivity of the earth's subsurface may be an arbitrary 3-D isotropic function in the middle of the domain, while towards the distant domain boundaries the conductivity becomes 1-D with flat topography, that is, changing only vertically. In the frequency domain with $e^{i\omega t}$ time dependence, where ω is the angular frequency, the physical property variables are admittivity $\hat{\sigma} = \sigma + i\omega\epsilon$ with electrical conductivity $\sigma \geq 0$, dielectric permittivity $\epsilon > 0$, and magnetic permeability $\mu > 0$.

Similar to numerous other authors (e.g. following Hohmann 1988), we define (E^p, H^p) as primary fields, which would be those within and over the 1-D host, for use as an impressed source J^{imp}. Thus we denote

$$J^{\text{imp}} = -(\hat{\sigma} - \hat{\sigma}^p)E^p \tag{1}$$

Secondary and primary fields are added to obtain total fields as:

$$E^t = E + E^p, \quad H^t = H + H^p \tag{2}$$

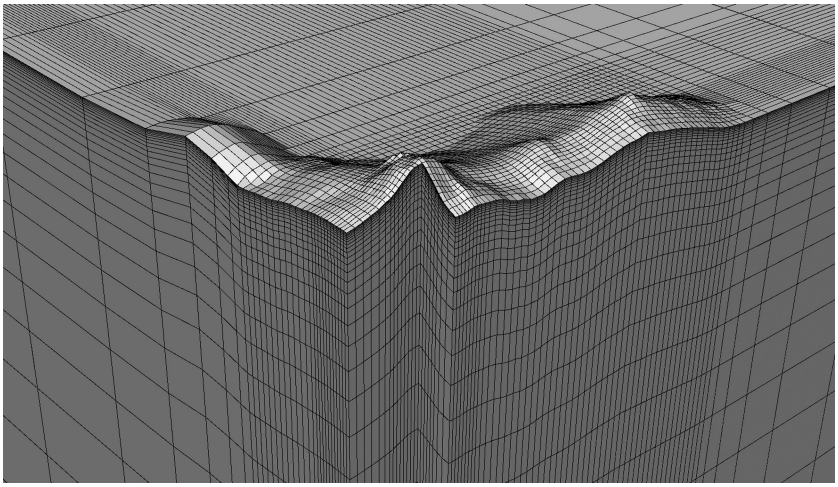

Figure 1. 3-D view of an example hexahedral mesh with topography. Only the underground part of the mesh is shown. One sees increasingly high aspect ratio of elements approaching the boundary $\partial\Omega$. This view is from the southwest of mesh number 3 for Mount Erebus model analysed later.

One assumes that far from conductivity inhomogeneity, that is, near $\partial\Omega$,

$$E^t \approx E^p, \quad H^t \approx H^p \tag{3}$$

and thus the secondary electric field satisfies $E \approx 0$ near the domain boundary.

The secondary field E obeys the vector Helmholtz equation in the open spatial domain $\Omega \subset \mathbb{R}^3$:

$$\nabla \times \left(\frac{1}{\mu}\nabla \times E\right) + \mathrm{i}\omega\hat{\sigma}E = -\mathrm{i}\omega(\hat{\sigma} - \hat{\sigma}^p)E^p \tag{4}$$

(Hohmann 1988). As a basis for FE formulation, we will consider a weak form of eq. (4) (*cf.* Monk 1992):

$$\int_\Omega \frac{1}{\mu}\nabla \times E \cdot \nabla \times M + \mathrm{i}\omega \int_\Omega \hat{\sigma}E \cdot M = \mathrm{i}\omega \int_\Omega J^{\mathrm{imp}} \cdot M \tag{5}$$

satisfied for all $M \in \mathcal{H}_0(\nabla\times, \Omega)$. The solution E should be a member of the same Sobolev space $\mathcal{H}_0(\nabla\times, \Omega)$ which is formally defined as

$$\mathcal{H}_0(\nabla\times, \Omega) = \left\{ M{:}\Omega \to \mathbb{C}^3 : \int_\Omega \left(|M|^2 + |\nabla \times M|^2\right) < \infty, \right.$$
$$\left. n \times M|_{\partial\Omega} = 0 \right\} \tag{6}$$

It is a space of complex valued vector fields that are square integrable with square integrable curl. Heuristically, one can think of the members of this space as having continuous tangential components across any surface going through Ω. $\mathcal{H}_0(\nabla\times, \Omega)$ is a natural space for the electric field E. The boundary condition $n \times E = 0$ is a natural consequence of eqs (2) and (3).

For numerical approximation, we choose first-order edge elements $\mathcal{H}_0^h(\nabla\times, \Omega)$ on a hexahedral mesh (see Nédélec 1986). By construction $\mathcal{H}_0^h(\nabla\times, \Omega) \subset \mathcal{H}_0(\nabla\times, \Omega)$ and as the mesh element size $h \to 0$, $\mathcal{H}_0^h(\nabla\times, \Omega)$ approaches $\mathcal{H}_0(\nabla\times, \Omega)$. The tangential components of the members of $\mathcal{H}_0^h(\nabla\times, \Omega)$ are continuous across elements while the normal component may experience a jump. Degrees of freedom of the first-order edge elements are related to the integral of the E-field along an edge. Through Stokes' theorem, an integration of E along the edges, around the face yields the flux of $\nabla \times E$ through the face. This shows that edge element discretization is compatible with the curl operator.

The electric field over Ω is represented as a linear combination of the edge shape functions N_i with coefficients ξ_i:

$$E = \sum_{i=1}^{n_e} \xi_i N_i \tag{7}$$

where $i = 1, \ldots, n_e$ are indices of the edges that do not lie on the boundary. By excluding the edges lying on the boundary one imposes the boundary condition of $n \times E = 0$ on $\partial\Omega$. It is equivalent to setting the coefficients related to the edges lying on the boundary to zero. By substituting eq. (7) into eq. (5) and using N_j as test functions, one obtains a linear system (*cf.* Monk 1992)

$$A\xi = b \tag{8}$$

$$A_{i,j} = \left[\int_\Omega \frac{1}{\mu}\nabla \times N_i \cdot \nabla \times N_j + \mathrm{i}\omega \int_\Omega \hat{\sigma}N_i \cdot N_j\right] \tag{9}$$

$$b_i = \mathrm{i}\omega \int_\Omega J^{\mathrm{imp}} \cdot N_i. \tag{10}$$

The secondary magnetic field is calculated as

$$H = \frac{-\nabla \times E}{i\omega\mu}. \tag{11}$$

This justifies the choice of first-order edge elements which have the same accuracy $O(h)$ for both the field and the curl.

Note that 1-D host layer interfaces may project through individual deformed elements and as a result J^{imp} is discontinuous within an element. The integration of terms in eqs (9) and (10) is done using a quadrature integration of the form

$$\sum_{i=1}^{n} f(u_i)v_i, \tag{12}$$

where u_i are points in the reference element, which is a unit cube in our case and v_i are weights. If the integrand f is smooth in the element, which is true for eq. (9) and for eq. (10) if the 1-D host layer interface does not project through an element, positions u_i and weights v_i are set according to Gaussian quadrature. Yet for eq. (10), if a 1-D conductivity layer interface splits the element, the integrated function is discontinuous and the integration is done by distributing u_i uniformly in the unit cube and setting all $v_i = \frac{1}{n}$. For accuracy of integration, n should have larger values than in the case of a smooth function. As will be seen, with sufficiently fine integration of the

primary field over the element conductivity differences, we are able to achieve accurate responses. For the numerical integration, we use 10 points in each direction, which results in 1000 points in each element. To limit the additional computational effort due to the evaluation of the source term at so many points, such an integration is done only if the layer boundary crosses the element.

In this paper we consider the MT source, namely that of a vertically propagating, planar EM wave. The total field components at specified surface locations and frequencies are interrelated through the tensor impedance Z and tipper K as

$$\begin{bmatrix} E_x^t \\ E_y^t \\ H_z^t \end{bmatrix} = \begin{bmatrix} Z_{xx} & Z_{xy} \\ Z_{yz} & Z_{yy} \\ K_{zx} & K_{zy} \end{bmatrix} \begin{bmatrix} H_x^t \\ H_y^t \end{bmatrix}, \tag{13}$$

where subscripts x, y, z denote components of a vector field. Eq. (8) is solved twice for two polarizations ($k = 1, 2$) of the source field E^p, typically in the x- and then the y-directions, to generate two equations in two unknowns for each row of the tensor (13). The equations expressing the impedance in terms of the electric and magnetic fields are listed in, for example, Newman & Alumbaugh (2000) and can be written analogously for the tipper.

A receiver can be positioned at an arbitrary location $\mathbf{r}$ with respect to element edges via appropriate interpolation. In general, let $\mathbf{r}$ be inside an element with edges $e_1, \ldots, e_{12}$. Then field E^k at location $\mathbf{r}$ is given by

$$E^k(\mathbf{r}) = \sum_{l=1}^{12} N_{e_l}(\mathbf{r})\xi_{e_l} = \begin{bmatrix} (w_x^E)^T \xi^k \\ (w_y^E)^T \xi^k \\ (w_z^E)^T \xi^k \end{bmatrix}. \tag{14}$$

Here w_x^E, w_y^E, w_z^E contain interpolation vectors with at most 12 non-zero values corresponding to x, y and z components of edge shape functions $N_{e_1}(\mathbf{r}), \ldots, N_{e_{12}}(\mathbf{r})$.

Similarly, the secondary magnetic field $H^k(\mathbf{r})$ for polarization k, calculated using eq. (11) at location $\mathbf{r}$, is given by

$$H^k(\mathbf{r}) = \sum_{l=1}^{12} \frac{\nabla \times N_{e_l}(\mathbf{r})}{-i\omega\mu}\xi_{e_l} = \begin{bmatrix} (w_x^H)^T \xi^k \\ (w_y^H)^T \xi^k \\ (w_z^H)^T \xi^k \end{bmatrix}. \tag{15}$$

This time the only non-zero values of w_x^H, w_y^H, w_z^H are x, y and z components of

$$\left(\frac{\nabla \times N_{e_1}(\mathbf{r})}{-i\omega\mu}, \ldots, \frac{\nabla \times N_{e_{12}}(\mathbf{r})}{-i\omega\mu} \right).$$

Total fields are obtained as in eq. (2).

The locations of the MT receivers are on the Earth's surface, which is always at an element's face. The along-face (tangential) components of the discretized electric field experience a jump at the face edges, thus it is best to use the values of the field calculated at the face centre. One could evaluate the field elsewhere by interpolation of the fields from the neighbouring face centres, yet for simplicity we assume that the receiver's location $\mathbf{r}$ is at the face centre. This requires MT receiver relocations in practice. In our inversions (see our companion paper, Kordy *et al.* 2015b) we consider the element size to be several times smaller than the distance between the receivers, thus the relocation is not very large and does not appear to lead to a significant inversion error (see subsequent Mount Erebus simulation and the brick-under-hill synthetic inversion of Kordy *et al.* 2015b).

Because the tangential electric field is continuous across the surface, it is immaterial whether we approach the surface from within an element below or above the air-earth interface. E-fields normal to a surface are discontinuous and must be evaluated on the side of interest, or interpolated using the values of the total electric current at the element centres. If magnetic permeability μ is the same above and below the surface, the magnetic field should be continuous as well. However, because the H-field obtained through curl E is piecewise constant from element face to face, we use an average of the H-field from the elements on either side of a receiver. As a result interpolation vectors w corresponding to the magnetic field may have up to 20 non-zero entries. The interpolation vectors w depend neither on the primary source fields nor on the conductivity model σ.

To calculate the MT response apart from solving eq. (8) one needs to evaluate the entries of matrix A as well as calculate the source vectors b (eq. 10). In our implementation using OpenMP, for a model with a mesh with 101, 101 and 50 cells in the x, y and z directions, respectively ($101x\,101y\,50z$) and 256 MT receivers, the calculation of the system matrix takes about 1.7 per cent of the time of the forward modelling (response F and Jacobian J). We have parallelized the calculation of the source vectors (10) also using OpenMP. If 9-point quadrature is used for all elements, the time of the calculation of the right hand side (rhs) vectors, for the same model, is about 0.15 per cent of the total forward modelling time. In practice, if the background conductivity layer crosses an element, we use a quadrature with 1000 points, which increases the computational time. Yet even if the quadrature with 1000 points is used for all of the elements, the time of computation is around 0.8 per cent of the total forward modelling time.

3 DIVERGENCE CORRECTION

Smith (1996) recognized that matrices formed from the numerical approximation of eq. (4) suffer from a particular ill-conditioning. This is why researchers considered solving for vector and scalar potentials (Haber *et al.* 2000; Mitsuhata & Uchida 2004; Roy 2007; Kordy *et al.* 2015a). The second term on the left side of eq. (4) becomes very small at either low frequencies or small admittivities, so the solution becomes vulnerable to parasitic curl-free fields. These are manifest as erroneous divergences of current density within the earth model that require corrective steps. For example, consider linear system (8) whose true solution is ξ, approximated by eq. (7). Let the gradient of a potential field be added to the solution such that

$$\hat{E} = E + \nabla\tilde{\varphi} = \sum_{i=1}^{n_e} \hat{\xi} N_i \tag{16}$$

and let the values of $\nabla\tilde{\varphi}$ be of order 1. The residual r of eq. (7) is defined by:

$$r = A\hat{\xi} - b = A\xi - b + A(\hat{\xi} - \xi) = A(\hat{\xi} - \xi). \tag{17}$$

The ith component of the residual vector r is

$$r_i = \sum_{j=1}^{n_e} A_{i,j}(\hat{\xi_j} - \xi_j),$$

which for the air ($\hat{\sigma} = i\omega\epsilon_0$) reduces to

$$r_i = -\omega^2\epsilon_0 \int_\Omega N_i \cdot \nabla\tilde{\varphi}.$$

Thus, the residual will be nonzero, but very small—of the order $\omega^2\epsilon_0$ for air. Even if we modify the field substantially by adding

$\nabla\tilde{\varphi}$, there may be hardly any difference in the residual value. An eigenvalue analysis of ill-conditioning of eq. (8) is presented in Appendix A.

For iterative solutions to eq. (8), the typical procedure for removing spurious curl-free fields, called divergence correction, is to compute several solution iterations, estimate current divergences over the discretized model domain, calculate the curl-free fields arising from such divergences and remove these fields from the full iterative solution at that stage (e.g. Smith 1996; Newman & Alumbaugh 2000; Sasaki 2001; Siripunvaraporn *et al.* 2002; Farquharson & Miensopust 2011). This is repeated numerous times until final convergence. One can also add the divergence condition to the system of equations (Vardapetyan & Demkowicz 1999; Schwarzbach 2009; Grayver *et al.* 2013) although that increases the number of unknowns in the linear system. For example, Grayver *et al.* (2013) in their approach increase the number of unknowns by one-third.

We present an alternative technique that achieves an efficient and accurate divergence correction for our FE method. Consider any domain Ω, with spatially changing conductivity $\hat{\sigma}$, which includes both air and the subsurface. The space $\mathcal{H}_0(\nabla\times,\Omega)$, defined in eq. (6), may be decomposed into the null space of the curl and the space orthogonal to it (Gunzburger & Bochev 2009). Specifically:

$$\mathcal{H}_0(\nabla\times,\Omega) = R(\nabla)\oplus R(\nabla)^{\perp_{\hat{\sigma}}} \tag{18}$$

For every $M\in\mathcal{H}_0(\nabla\times,\Omega)$, there is a unique decomposition:

$$M=\nabla\varphi_M + M_\perp,\quad \varphi_M\in H_0^1(\Omega),\ \ M_\perp\in R(\nabla)^{\perp_{\hat{\sigma}}} \tag{19}$$

where

$$\begin{aligned}
\mathcal{H}_0^1(\Omega) &= \left\{\varphi:\Omega\to\mathbb{C} \quad : \int_\Omega \left(|\varphi|^2+|\nabla\varphi|^2\right)<\infty,\ \varphi|_{\partial\Omega}=0\right\}\\
R(\nabla) &= \{\nabla\varphi \quad : \varphi\in\mathcal{H}_0^1(\Omega)\}\\
R(\nabla)^{\perp_{\hat{\sigma}}} &= \left\{M\in\mathcal{H}_0(\nabla\times,\Omega) \quad : \int_\Omega \hat{\sigma}M\cdot\nabla\varphi=0\ \ \forall\varphi\in\mathcal{H}_0^1(\Omega)\right\}
\end{aligned}$$

Space $\mathcal{H}_0^1(\Omega)$ is a space of complex valued scalar potentials, the square integrable scalar fields which have a gradient that is square integrable. One can think of the members of this space as of scalar functions that are continuous across any surface inside the domain. The '0' subscript corresponds to the assumption of zero value on the boundary Ω. Once the gradient ∇ is applied to those functions one obtains the space $R(\nabla)$. Because $\nabla\times\nabla\varphi=0$, $R(\nabla)$ is in the null space of the curl. Moreover, the range of the gradient on $\mathcal{H}_0^1$ is exactly equal to the null space of the curl in the space $\mathcal{H}_0(\nabla\times,\Omega)$ (Gunzburger & Bochev 2009). For more thorough discussion of Sobolev spaces $\mathcal{H}_0(\nabla\times,\Omega)$ and $\mathcal{H}_0^1(\Omega)$ see Girault & Raviart (1986) and Adams & Fournier (2003). The decomposition in eq. (18) allows us to represent a field from $\mathcal{H}_0(\nabla\times,\Omega)$ as a sum of two fields, one in the null space and the other orthogonal to it. This decomposition is called the Helmholtz decomposition or the Hodge decomposition of $\mathcal{H}_0(\nabla\times,\Omega)$. The proof of its existence for the case of a constant $\hat{\sigma}$ may be found in Amrouche *et al.* (1998). For a proof given our case of non-constant $\hat{\sigma}$ when Ω includes both air and the earth's subsurface, one should consider a Poisson equation for φ_M:

$$\int_\Omega \hat{\sigma}\nabla\varphi_M\cdot\nabla\phi = \int_\Omega \hat{\sigma}M\cdot\nabla\phi$$

for $\varphi_M,\ \phi\in\mathcal{H}_0^1$, which has a unique solution.

In the case of a constant $\hat{\sigma}$, it is a decomposition into a curl-free part $\nabla\varphi_M$ and a divergence-free part $M_\perp$, which is orthogonal to $R(\nabla)$. In the constant $\hat{\sigma}$ case it is the same as representing the original field using a vector and a scalar potential with a Coulomb gauge, in which case the vector potential is divergence free (Mitsuhata & Uchida 2004).

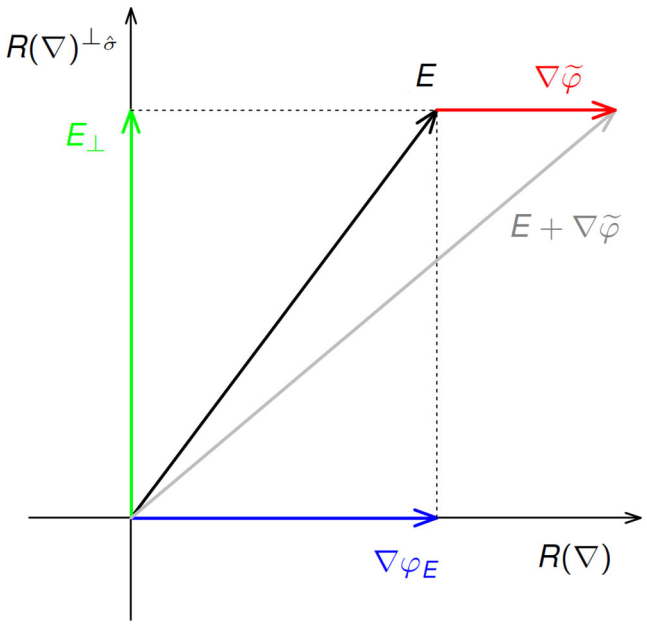

Figure 2. Hodge decomposition of the solution E, together with the added error of the form $\nabla\tilde{\varphi}$.

In our context, when $\hat{\sigma}\neq$ constant, we have $\nabla\cdot(\hat{\sigma}M_\perp)=0$, which may be seen through integration by parts of the condition defining $R(\nabla)^{\perp_{\hat{\sigma}}}$. Also, if $\hat{\sigma}\in\mathbb{R}$ and $\hat{\sigma}>0$ one may interpret the space $R(\nabla)^{\perp_{\hat{\sigma}}}$ as the space orthogonal to $R(\nabla)$ with an inner product having $\hat{\sigma}$ as the weight.

To visualize the subsequent derivations consider Fig. 2. Let the solution E to eq. (5) be represented using the Hodge decomposition (19), namely

$$E=\nabla\varphi_E+E_\perp,\quad \varphi_E\in H_0^1(\Omega),\ \ E_\perp\in R(\nabla)^{\perp_{\hat{\sigma}}}. \tag{20}$$

By setting $M=M_\perp\in R(\nabla)^{\perp_{\hat{\sigma}}}$ and then $M=\nabla\varphi$, one can show that eq. (5) is equivalent to two uncoupled equations on $R(\nabla)^{\perp_{\hat{\sigma}}}$ and $R(\nabla)$ respectively:

$$\begin{aligned}
\int_\Omega \frac{1}{\mu}\nabla\times E_\perp\cdot\nabla\times M_\perp + \mathrm{i}\omega\int_\Omega \hat{\sigma}E_\perp\cdot M_\perp &= \mathrm{i}\omega\int_\Omega J^{\mathrm{imp}}\cdot M_\perp\\
\mathrm{i}\omega\int_\Omega \hat{\sigma}\nabla\varphi_E\cdot\nabla\varphi &= \mathrm{i}\omega\int_\Omega J^{\mathrm{imp}}\cdot\nabla\varphi.
\end{aligned} \tag{21}$$

The first equation is satisfied $\forall M_\perp\in R(\nabla)^{\perp_{\hat{\sigma}}}$, the second $\forall\varphi\in\mathcal{H}_0^1(\Omega)$. The second equation ensures that the component $\nabla\varphi_E$ is proper, so if we impose this equation, we may remove the error of the form $\nabla\tilde{\varphi}$. In a discrete case, we are dealing with $\mathcal{H}_0^h(\nabla\times,\Omega)$, which is the space of first-order edge elements. An important property of this space is that a Hodge decomposition similar to eq. (18) exists (see Gunzburger & Bochev 2009). The space $\mathcal{H}_0^1(\Omega)$ has to be replaced with $\mathcal{H}_0^{1,h}(\Omega)$—the space spanned by first-order nodal shape functions on the same mesh.

The correction is applied as follows. Let E, be an approximation of the electric field given by eq. (7). Solve Poisson equation for $\nabla\varphi_{\mathrm{corr}}\in\mathcal{H}_0^{1,h}(\Omega)$, $\forall\varphi\in\mathcal{H}_0^{1,h}(\Omega)$:

$$\mathrm{i}\omega\int_\Omega \hat{\sigma}\nabla\varphi_{\mathrm{corr}}\cdot\nabla\varphi = \mathrm{i}\omega\int_\Omega (\hat{\sigma}E-J^{\mathrm{imp}})\cdot\nabla\varphi. \tag{22}$$

The corrected electric field $E_{\rm corr}$ is

$$E_{\rm corr} = E - \nabla\varphi_{\rm corr}. \tag{23}$$

Note that the corrected field satisfies the original eq. (5) in a discrete setting for $E, M \in \mathcal{H}_0^h(\nabla\times, \Omega)$. In fact, if infinite precision was used to solve eq. (5) numerically, there would be no need for the correction. The correction considers the original equation on a subspace and removes a numerical error introduced by a direct solver that uses finite precision.

The correction may be given further justification by considering the second equation in eq. (21). Using the fact that $E_\perp = E - \nabla\varphi_E \in R(\nabla)^{\perp_{\hat\sigma}}$ and integrating by parts, we obtain:

$$\mathrm{i}\omega \int_\Omega (\nabla\cdot(\hat\sigma E))\varphi = \mathrm{i}\omega \int_\Omega (\nabla\cdot J^{\rm imp})\varphi. \tag{24}$$

Thus, we ensure that the divergence of electric current is proper weakly, on average, with $\varphi \in \mathcal{H}_0^{1,h}(\Omega)$ as a weight. The right-hand side of eq. (22) may be viewed as excessive divergence of the electric current, which is removed when eq. (23) is applied.

Divergence correction requires solving the Poisson eq. (22), which we do using nodal-based FEs. The divergence correction system matrix has three times less variables than the original system matrix, and at least four times less non-zeroes. In our experience, the divergence correction requires much less run time than solving the original system (8); factorization phase is at least eight times faster and solve phase is at least five times faster.

Although the main computational cost is related to the solution of the linear system (22), it is not the only cost of the divergence correction. One needs to calculate the system matrix of eq. (22), evaluate the right-hand side of eq. (22), and once $\varphi_{\rm corr}$ is obtained one needs to apply the correction using eq. (23). We have parallelized those calculations using MKL SparseBLAS library as well as using OpenMP. After parallelization, all of those additional calculations for a model with a mesh $101x\ 101y\ 50z$ and 256 MT receivers are more than 2.5 times faster than the solution of eq. (22) using MKL PARDISO and constitute about 3.4 per cent of the forward modelling time. The divergence correction sparse solve with MKL PARDISO takes about 9 per cent of the forward modelling time.

4 FIELD AND MT RESPONSE JACOBIANS

A primary goal in developing the FE simulator is to apply it to non-linear inversion of MT field data. As described more fully in our companion paper, we examine both model and data space approaches to parameter updates under the Gauss–Newton framework (Siripunvaraporn *et al.* 2005). For defining terms as related to FE simulation, the model space update equation is (e.g. Tarantola 2005; Mackie *et al.* 1988):

$$\begin{aligned}&[J^T B_d J + \lambda B_m](m_{n+1} - m_0)\\ &\quad = J^T B_d[d - F(m_n) + J(m_n - m_0)],\end{aligned} \tag{25}$$

where $F(m_n)$ is the MT response at iteration n using our FE code, d is the vector of N_d observed MT data weighted against their estimated covariance matrix B_d^{-1}, B_m^{-1} is a model covariance matrix which stabilizes or regularizes the N_m model parameter variations, m_0 is a reference model, and λ is a constant controlling trade-off between data fit and model parameter stabilization.

Term J is the N_d by N_m matrix of parameter Jacobians or derivatives (Tarantola 2005) which specify the incremental change in the value of an MT response datum (in Z or K) to an incremental change in the value of a subsurface electrical conductivity parameter. First, we focus on the derivatives of the secondary fields. There have been numerous ways to express this in the literature (e.g. McGillivray *et al.* 1994); here we basically generalize from the 2-D approach of deLugao & Wannamaker (1996). Recalling the interpolation vectors w, consider an entry σ_j of the FE mesh conductivity vector σ. The entry may correspond to a single element or a group of them. The derivative of a field value $w^T\xi^k$ with respect to σ_j may be evaluated as:

$$\begin{aligned}\frac{\partial(w^T\xi^k)}{\partial\sigma_j} &= w^T\frac{\partial\xi^k}{\partial\sigma_j} = w^T\frac{\partial(A^{-1}b^k)}{\partial\sigma_j} = w^T\left[\frac{\partial A^{-1}}{\partial\sigma_j}b^k + A^{-1}\frac{\partial b^k}{\partial\sigma_j}\right]\\ &= w^T\left[\left(-A^{-1}\frac{\partial A}{\partial\sigma_j}A^{-1}\right)b^k + A^{-1}\frac{\partial b^k}{\partial\sigma_j}\right]\\ &= w^T\left[-A^{-1}\frac{\partial A}{\partial\sigma_j}(A^{-1}b^k) + A^{-1}\frac{\partial b^k}{\partial\sigma_j}\right]\\ &= w^T\left[-A^{-1}\frac{\partial A}{\partial\sigma_j}\xi^k + A^{-1}\frac{\partial b^k}{\partial\sigma_j}\right]\end{aligned}$$

for source polarization k. This reduces to

$$\frac{\partial(w^T\xi^k)}{\partial\sigma_j} = w^T\left(A^{-1}\left[-\frac{\partial A}{\partial\sigma_j}\xi^k + \frac{\partial b^k}{\partial\sigma_j}\right]\right). \tag{26}$$

As written, in order to calculate the derivatives of the field values with respect to all $(\sigma_j)_{j=1}^{N_m}$, one would have to solve one linear equation for each polarization and for each σ_j, and then multiply by the proper w, to obtain the desired derivatives. That yields $2\cdot N_m$ linear systems to solve, where N_m is the number of inversion cells. However, exploiting interchangeability of sources and receivers in reciprocity, or using the adjoint method, or simply using the associativity of the matrix multiplication, eq. (26) may be rewritten as

$$\begin{aligned}\frac{\partial(w^T\xi^k)}{\partial\sigma_j} &= \left(w^TA^{-1}\right)\left[-\frac{\partial A}{\partial\sigma_j}\xi^k + \frac{\partial b^k}{\partial\sigma_j}\right]\\ &= \left(A^{-T}w\right)^T\left[-\frac{\partial A}{\partial\sigma_j}\xi^k + \frac{\partial b^k}{\partial\sigma_j}\right].\end{aligned} \tag{27}$$

In this form we solve one linear system for each field component. The method yields $5\cdot N_{\rm rec}$ linear systems to solve, where $N_{\rm rec}$ denotes the number of receivers. The matrix A, defined at (9), is symmetric, so $A^{-T} = A^{-1}$. To calculate $A^{-1}w$, we are solving a linear system where the source w, defined in eqs (14) and (15), is distributed on the edges surrounding the receiver location (*cf.* deLugao & Wannamaker 1996).

Jacobians for impedance Z and tipper K at each receiver follow by applying the chain rule to the equations for the impedance and tipper elements of eq. (13) defined from applying the two source polarizations $k = 1, 2$. The individual impedance element derivatives are listed in Newman & Alumbaugh (2000) and the tipper element derivatives follow by analogy. For inversion implementation, derivatives are converted to be with respect to $\log_{10}$ resistivity (Hohmann & Raiche 1988).

The main computational cost of the calculation of the Jacobian is the factorization of A and application of its inverse to w, for which example run times are given further in the paper. Yet one also needs to use the result of this calculation in eq. (27). And as for large models the Jacobian matrix is large, it might take a notable time to fill its entries in the memory. In our implementation with OpenMP the time of evaluation of eq. (27), once $(A^{-T}w)$ is obtained, and the successive evaluation of the derivative of Z and K with respect to

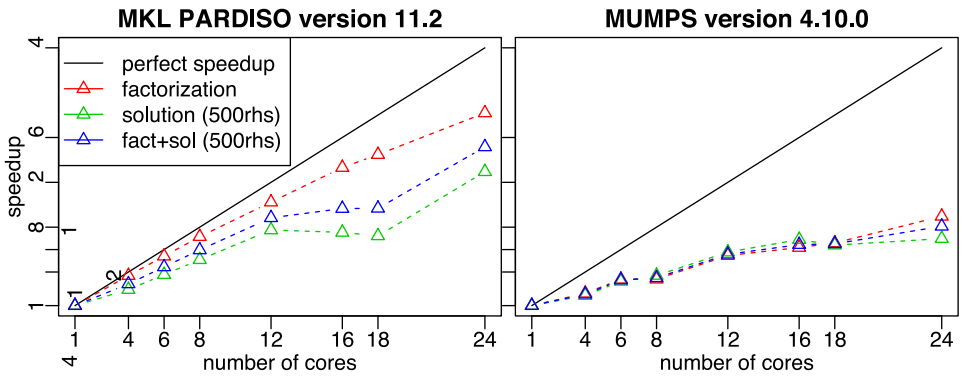

Figure 3. Speedup of MKL PARDISO and MUMPS for a fixed problem with mesh with 85x 85y 50z cells on a single workstation with 24 cores. For PARDISO, runs with different number of OpenMP threads are compared. For MUMPS, we present runs with different number of MPI processes, each using a single OpenMP thread, which is the configuration with the smallest total time (factorization + solution of 500 rhs). We show the speedup of the factorization phase, the solution phase with 500 rhs, and of both of the phases together.

the model, takes about 4 per cent of the forward modelling time for a model with a mesh 101x 101y 50z and 256 MT receivers.

5 DIRECT SOLVER

Several attractive features of direct solutions were listed in Introduction. Here we investigate the viability of 3-D FE modelling and inversion performed on single-chassis, multicore, SMP computers typically used in server applications and which are relatively affordable. We were attracted to this platform at first for direct solution of the model-space, Gauss–Newton parameter step equation, which was parallelized using a matrix tiling approach under OpenMP compiler directives and showed good scalability across an 8-core workstation with 32 GB RAM (Maris & Wannamaker 2010). Initially this tiling solution was applied also to the banded (daSilva *et al.* 2012) FE matrix and showed good scalability across a newer 24-core workstation with 512 GB RAM (Kordy *et al.* 2013). However, solution time overall was slower than desired, for example taking over 1 hr per frequency for a mesh 85x 88y 50z and two source vectors (i.e. no Jacobians).

Thus, in an effort to improve speed, we have investigated two popular computational libraries for directly factorizing $A = LDL^T$ and reducing source vectors. One is MUMPS (Amestoy *et al.* 2001, 2006), utilized by others (e.g. Oldenburg *et al.* 2008; Streich 2009; daSilva *et al.* 2012; Oldenburg *et al.* 2013). The other is PARDISO (Intel MKL implementation) (Schenk & Gärtner 2004). PARDISO has turned out to be faster in a shared memory setting.

The matrix A in eq. (9) is complex valued and symmetric (but not Hermitian). Both solvers initially find a permutation of variables, P, and the matrix is replaced with PAP^T (permutation of both columns and rows of the matrix, so that the matrix remains symmetric). Then a lower triangular matrix L and a diagonal matrix D are found such that $PAP^T = LDL^T$. The last step is the solve phase, that is, solving the system (8), which may be written as

$$PAP^T(P\xi) = Pb \quad \text{or} \quad LDL^T\tilde{\xi} = Pb, \quad \text{where} \quad \tilde{\xi} = P\xi$$

Permutation P is chosen to minimize the number of nonzero values in L matrix, and to allow for parallelization of the factorization and solve phases.

Both MUMPS and MKL PARDISO use third party ordering libraries to find P. For a comparison of the two solvers, we used the METIS (Karypis 2003) ordering library and thus both MUMPS and PARDISO calculate L having the same number of non-zeros. For a mesh with 85x 85y 90z cells, on a 24-core workstation (four Intel E5-4610 Sandy Bridge hex-core processors at 2.4 GHz), the factorization time of matrix (9) with MKL PARDISO was typically ∼40 per cent of that of MUMPS. The solution phase of MKL PARDISO took about 80 per cent of that of MUMPS. This may reflect the fact that PARDISO is written for the shared memory architecture (although there is an option to use it on a cluster), whereas

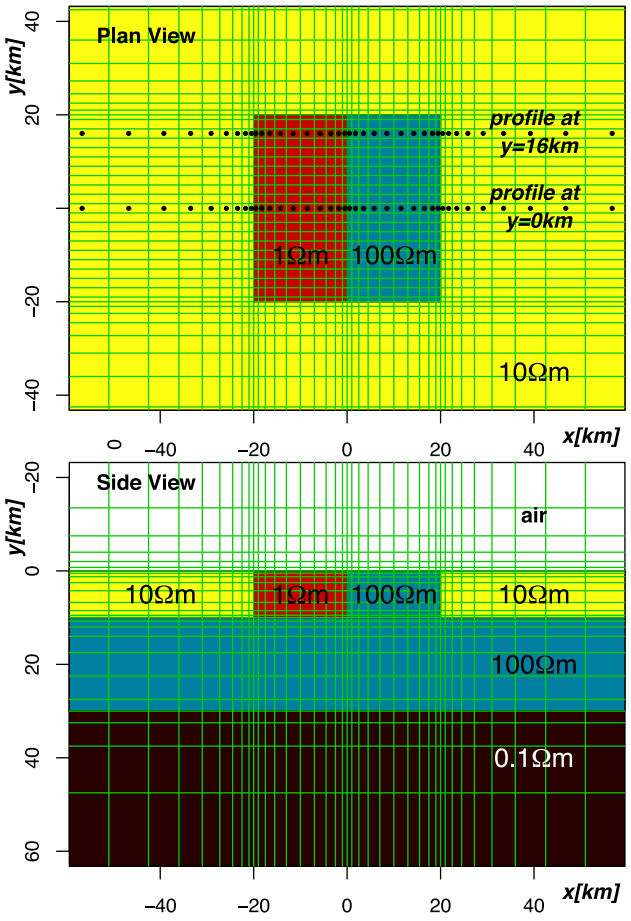

Figure 4. Outcropping double brick resistivity model, together with the mesh used. Element boundaries are drawn as solid green lines.

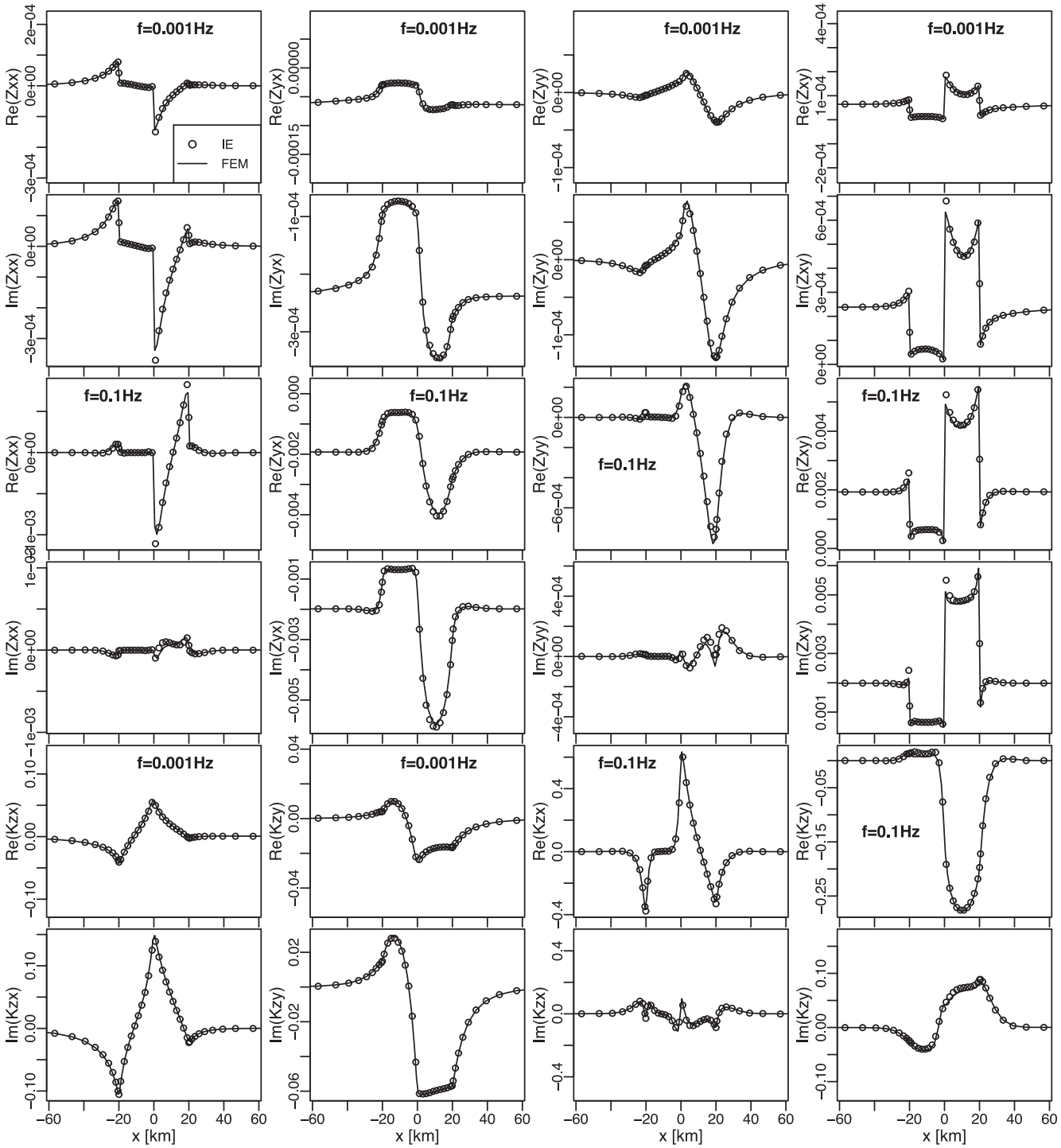

Figure 5. Forward MT response of a double brick model for profile at $y = 16$ km for comparison with Integral Equation code response. Frequencies are 0.001 and 0.1 Hz.

MUMPS is written for a distributed memory system. Additionally MUMPS uses more memory if many MPI processes are used, as the data are copied between the processes. MUMPS with 24 MPI processes uses more than twice the memory than that when run with one MPI process, which is about the amount of memory that MKL PARDISO needs.

The scalability of MKL PARDISO (version 11.2 of MKL library) and MUMPS (version 4.10.0) libraries is presented in Fig. 3. With 24 cores, the speedup of the factorization and solution phases is 18 and 13, respectively for PARDISO. For comparison, the speedup of MUMPS with 24 MPI processes, for the same problem, is 9 and 7 for the factorization and solution phases respectively. Furthermore we found that MUMPS scalability nearly plateaued between 12 and 24 cores. The times of computation for 24 cores were 81 and 111 s for factorization and solution phases in the case of PARDISO, and 190 and 153 s for factorization and solution phases in the case of MUMPS. Performance improvements may be expected in future versions of either library.

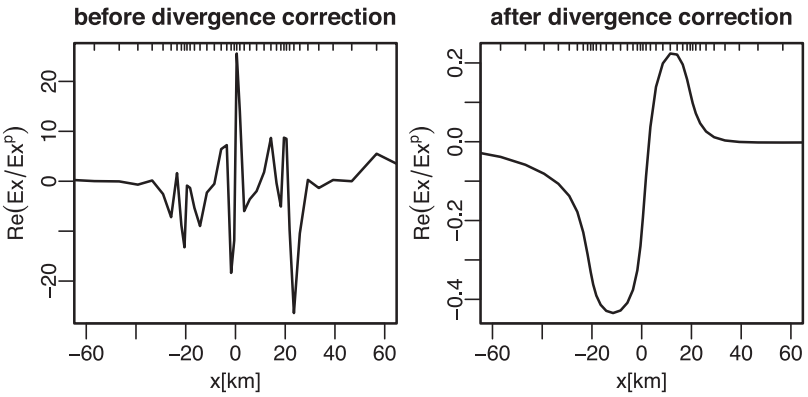

Figure 6. Real component of electric field E_x at a height of 2 km for the double brick model calculated before and after divergence correction for a frequency of 0.001 Hz. *Y*-axis scales are different for figure on the right and on the left; the field before correction is 100 × larger overall in magnitude. Tick marks along top plot border show calculation point locations.

6 EXAMPLE FORWARD CALCULATIONS

The accuracy of our 3-D FE forward code is tested against independent algorithms. These include a standard test of conductive and resistive heterogeneity under a flat surface, but we also focus on topography as a principal rationale for this work. Tests highlight the strength of the FE method in defining smooth, non-jagged topographic slopes.

6.1 Outcropping double brick Model

First we consider the popular, outcropping double brick 3-D model originally proposed in 2-D by Weaver *et al.* (1985, 1986) and included in the Commemi collection of trial models by Zhdanov *et al.* (1997). The central portion of its FE mesh appears in Fig. 4. The mesh has $52x\,53y\,31z$ elements, out of which the two bodies consist of $20x\,21y\,8z$ elements. We used 10 layers for the air and 21 layers for the earth. Element sizes grow steadily away from the centre of the domain to a total distance of 555 km from the centre. The 1-D background model is the true 3-D model without the two outcropping bricks. All calculations are done in double precision.

Complex tensor impedance Z and tipper K elements were calculated at the surface, over the cells' centres, along a profile at $y = 16$ km for frequencies of 0.001 Hz and 0.1 Hz. They are compared in Fig. 5 with those computed using the Integral Equations code of Wannamaker (1991), for which the body discretization coincides with that of the FE mesh. The agreement between the two codes clearly is very good, and compares favourably with the check against a finite difference approach in Mackie *et al.* (1993). Comparison was similarly good for the profile at $y = 0$ km (not shown) although Z_{xx}, Z_{yy}, K_{zy} are zero there.

The requirement for, and effectiveness of, the divergence correction described previously, is demonstrated for a profile 2km in the air over the centre of the double brick model in Fig. 6. On the left is the electric field in the *x*-direction across the sides of the body at the low frequency of 0.001 Hz. It consists mainly of numerical noise due to spurious curl-free electric fields. Nevertheless, as seen on the right side, the divergence correction is able to remove the error leaving a response which is a smooth, upward-continued version of a surface response (*cf.* Z_{xy} in Fig. 5). Thus we are able to model accurate E-fields in the air with our FE method as would be desired under efforts to create airborne MT platforms (e.g. Macnae 2010).

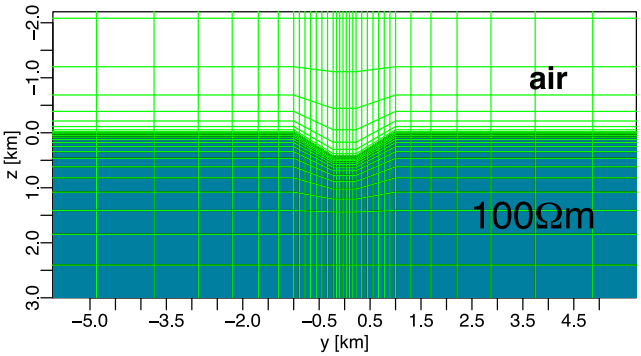

Figure 7. *YZ* cross-section of a 2-D valley, together with the central part of the 3-D FEM mesh. Element boundaries are drawn as solid green lines.

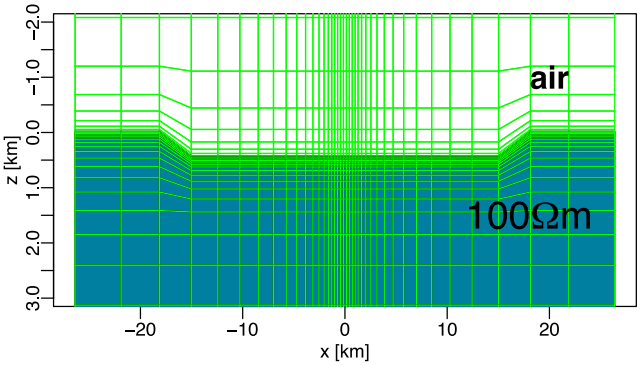

Figure 8. *XZ* cross-section of the 2-D valley, together with the 3-D FEM mesh. 5× vertical exaggeration.

6.2 2-D valley and hill

Because topographic simulation and inversion is a principal motivation for this work, we present several accuracy checks here. First, we compare fields over an elongate 3-D valley with those of the 2-D valley model of Wannamaker *et al.* (1986) computed with their nodal FE code. The valley is 450 m deep, 500 m wide at the bottom and 3 km wide at the top in a host of resistivity $\rho = 100\,\Omega$m (3-D cross-section in Fig. 7). In 3-D, infinite strike is approximated with a 30 km length (Fig. 8). The entire 3-D mesh consisted of $39x\,41y\,30z$ elements while the valley portion was covered by 21 elements across the *y*-direction. The mesh extended to 6 km above the ground, 11 km below the ground and laterally 26 km and 14 km from the valley

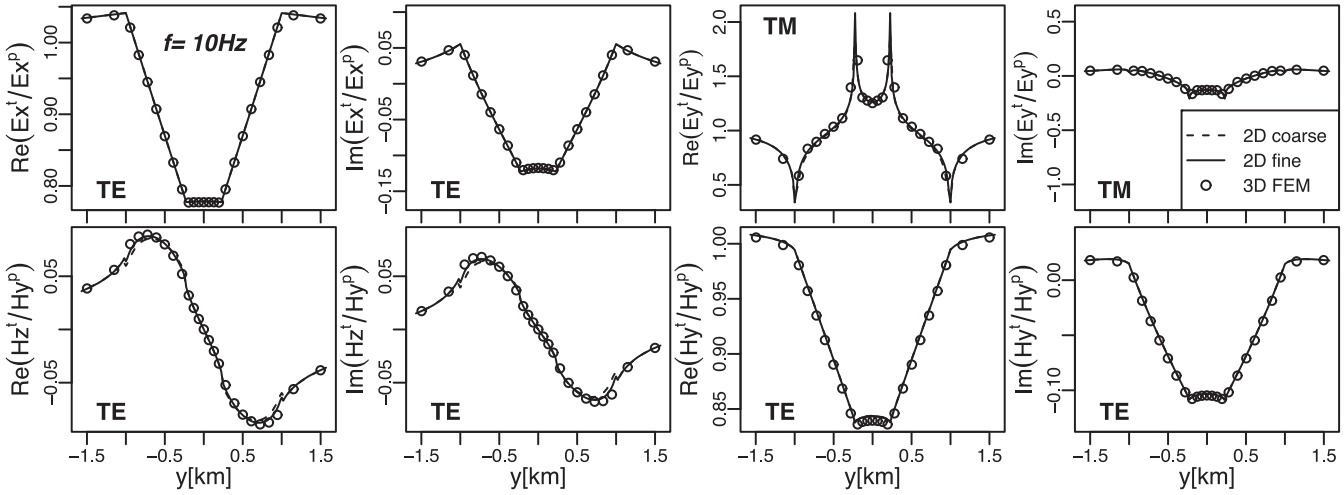

Figure 9. Normalized EM fields along the profile across the 2-D valley, for $x = 0$ km.

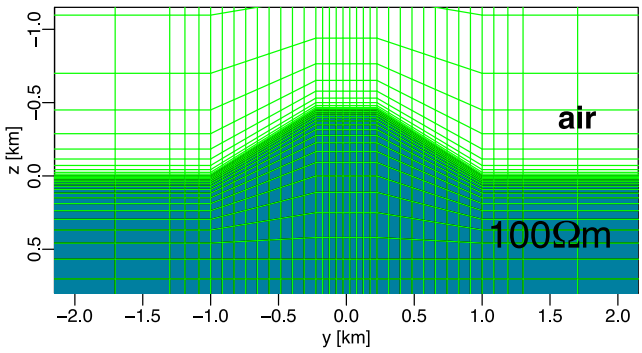

Figure 10. *YZ* cross-section of a 2-D hill, together with the central part of 3-D FEM mesh.

in *x*- and *y*-directions respectively. The 1-D background model is a 100 Ωm half space.

A coarse and a finer 2-D discretization are considered. The coarse valley is made up of 20 layers of elements each 22.5 m thick. The finer valley is made up of 40 layers of elements each 11.25 m thick. Element dimensions grow steadily away from the centre to a total distance of over 20 km to the sides and depth. Note that the 2-D mesh is rectilinear such that slopes must be made up of triangles rather than deformed quadrilaterals (Wannamaker *et al.* 1986). The *E*- and *H*-fields across the valley centre normalized by the primary fields are plotted in Fig. 9. The responses of the 3-D and 2-D codes are in close agreement.

For the hill model, we consider the high frequency of 1000 Hz to test whether the 3-D code can accurately simulate refraction of the EM fields normal to the slope, as was done in 2-D by Wannamaker *et al.* (1986). The small skin depth (∼160 m) requires a finer mesh

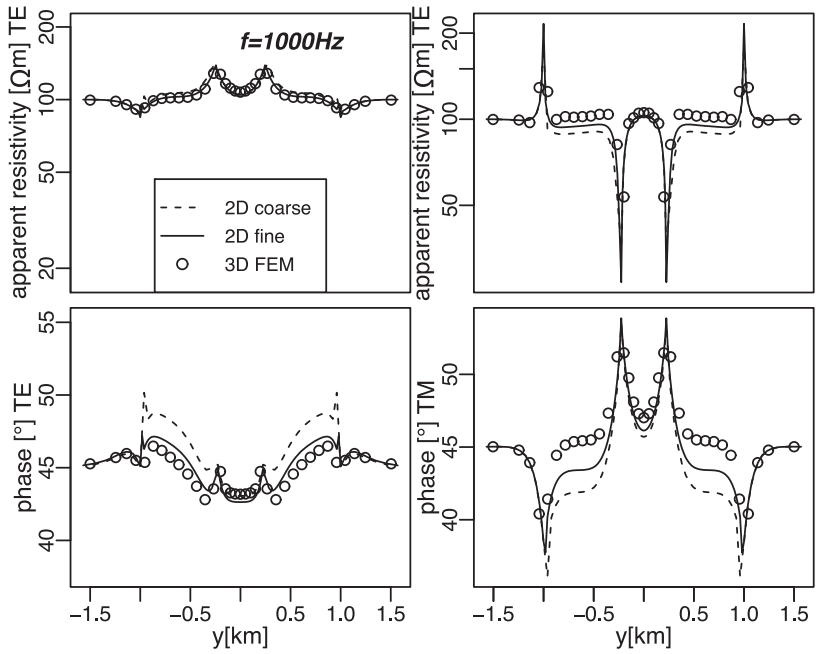

Figure 11. The ρ_a and phase responses from the 2-D code and 3-D codes for the 2-D hill at 1000 Hz. TE denotes the values derived from Z_{xy}, TM denotes the values derived from Z_{yz}.

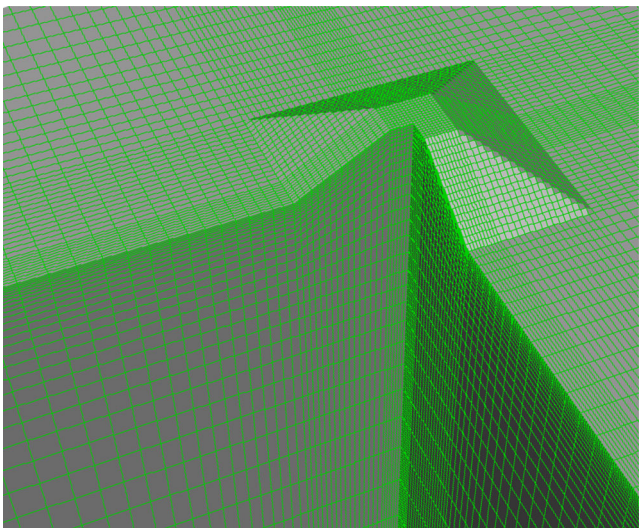

Figure 12. Central part of the finer mesh for the 3-D hill model.

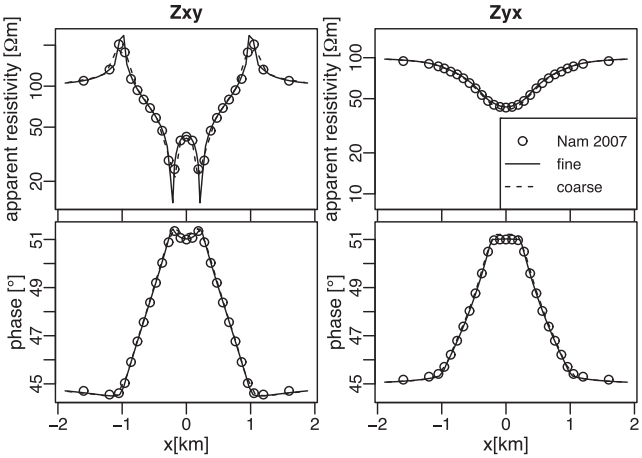

Figure 13. Apparent resistivities and phases for the 3-D hill model along a profile across the hill compared with the result of Nam *et al.* (2007). The results of Nam have been discretized from their plots.

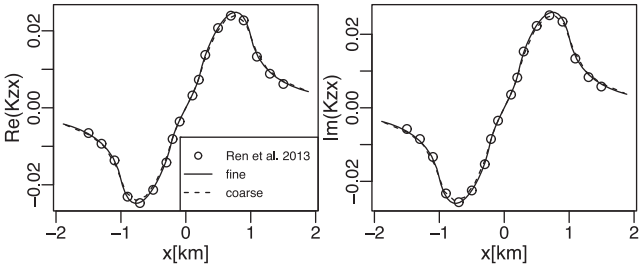

Figure 14. Tipper (x-component) for the 3-D hill model along a profile across the hill compared with the result of Ren *et al.* (2013) calculated on their seventh mesh. The results of Ren *et al.* have been discretized from their plots and converted to $e^{i\omega t}$ time dependence.

closer to the hill surface, although the lateral limits do not have to be so far (Fig. 10). The mesh extends 3 km above the highest point, 1.3 km below the base and laterally 5 and 4 km from the hill in x- and y-directions. The 2-D hill has the same dimensions and discretization as the valley for both coarse and fine versions. We compute the E- and H- fields parallel to the slope of the hill, and use those values to calculate apparent resistivity ρ_a.

The ρ_a should approach the true resistivity of the ground (100 Ωm) at high frequency because the total EM fields ideally become purely parallel to the slope. We present ρ_a and phase for TE and TM modes in Fig. 11. Note that for both fine mesh 2-D code and 3-D code results, away from breaks in slope, ρ_a is close to 100 Ωm and phase is close to 45°. In fact, the 3-D phase results look the most accurate, which may reflect a greater ease for layers of hexahedral elements to simulate essentially 1-D fields than for triangles, although the 2-D results are converging with finer discretization.

6.3 3-D trapezoidal hill

The next test model is the 3-D hill model considered by Nam *et al.* (2007). It has the same dimensions as the previous 2-D hill, but is square in horizontal cross-section (see Fig. 12). It is 0.45 km high, 0.5 km wide at the hilltop, 2 km wide at the base with resistivity of 100 m. It is calculated for 2 Hz, and the MT response is compared to that of Nam *et al.* (2007) and Ren *et al.* (2013). The background 1-D model is a 100 Ωm half space. Two grids were considered, the finer grid being 97x, 97y, and 50z while the coarser grid is 27x, 27y, 24z. The ρ_a, phase and the tipper along a profile across the centre of the hill are presented in Figs 13 and 14. The MT response calculated in Nam *et al.* (2007), Ren *et al.* (2013) and the field calculated by our FE code appear very similar.

6.4 Mount Erebus volcanic edifice, Antarctica

The prior topographic models involve relatively simple shapes and slopes. To test our algorithm's ability to accurately simulate topographic response of a complex natural structure, we consider Mount Erebus on Ross Island, Antarctica. Rising from sea level to 3794 m elevation, it may be the best example of an active phonolitic volcano (Moussallam *et al.* 2013). Our group has begun a comprehensive 3-D MT field survey to verify petrological models for magma genesis and transport (Hill *et al.* 2015). One season of fieldwork has been completed in 2014–2015, with two more consecutive seasons mobilizing at the time of this writing. Final responses are to be available for modelling in mid-2017. All sites are placed by helicopter assist, enabling relatively uniform coverage even in steep terrain. The digital elevation model (DEM) for Ross Island and surrounding bathymetry was provided by the New Zealand GNS Science organization at 40 m lateral spacing and ±6 m vertical accuracy from the resource described in Csatho *et al.* (2008) and the Ross Sea map of Davey (2004).

The main test is one of convergence with discretization, which involves three aspects. The first is convergence of MT response with mesh discretization for a fixed topographic geometry. The second is convergence of the subsampled topography towards the true surface with finer meshing. The third is convergence of computed response as mesh receiver location approaches true receiver location with discretization. As noted previously, mesh receivers are placed over element centres consistent with the fact that a single magnetic flux is estimated from $\nabla \times E$ around cell edges; this is standard both for first order Nédélec elements and for staggered grid finite difference methods (e.g. Madden & Mackie 1989; Mackie *et al.* 1993; Siripunvaraporn *et al.* 2002).

We consider five meshes, where mesh 1 is the coarsest (35x 52y 26z) and mesh 5 is the finest (127x 193y 101z) (Fig. 15; the intermediate mesh 3 is shown in Fig. 1). At each step, the mesh is refined by a factor of $\sqrt{2}$, so that in two steps the mesh is refined by a factor of 2. The location of the receiver on each mesh is the face

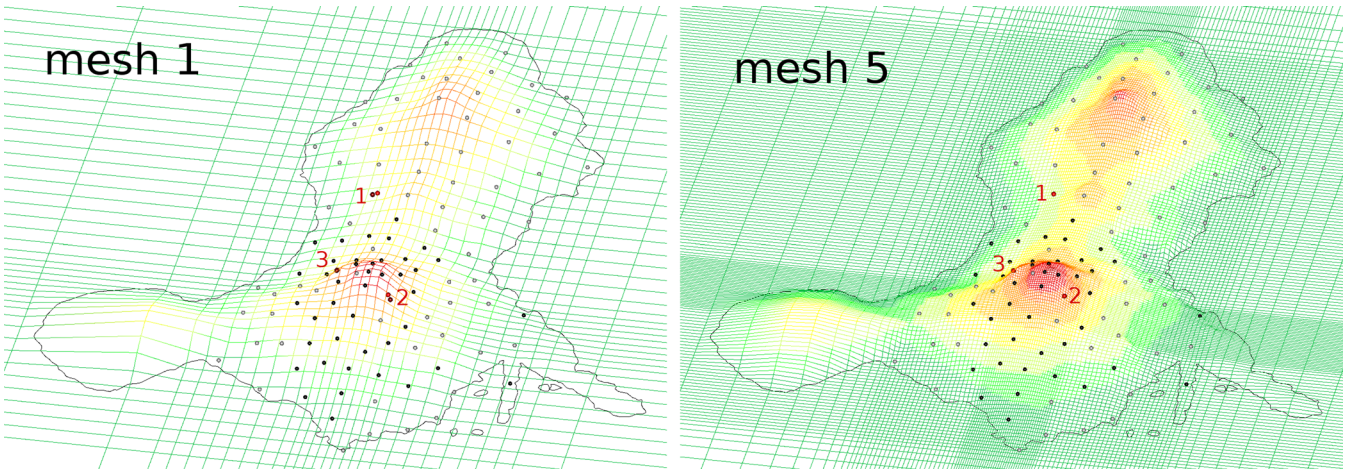

Figure 15. Meshes 1 and 5 for Mount Erebus model. Black dots show the locations of MT data collected to date, while grey dots are planned locations. Three light red dots show the true location of receivers for which MT responses are considered here. Dark red dots are the location of the closest surface face centre, where the fields are calculated.

centre closest to the true receiver location. The steep cone of Mount Erebus has the elements with the smallest x and y extent, the rest of Ross Island has its elements up to two times larger, and around the island the elements grow at a constant geometrical rate to reach the boundary of the domain which is 500 km away. The bottom and the top of the domain are at ±500 km distance from sea level. Bathymetry around the island is included to a distance of ∼200 km whereupon it is terminated, although seawater depths are only a few hundred meters until several kilometres from the shoreline. Additionally for each mesh, the elevation of the surface vertices was calculated as an average of the DEM on an area comparable to the horizontal extent of the element. As a result, the topography represented on a mesh converges towards the true topography as the mesh gets finer.

The Mount Erebus model is given a uniform resistivity of 100 Ωm in order to illustrate the effects of topography and meshing. Although it is difficult to isolate the three prior issues, if responses from all five meshes are reasonably close and converge with discretization, then our approach to modelling natural topography should be robust. We consider three MT receivers in Fig. 15 whose local slope is 7–8°, 28–25° and 32–40° respectively from meshes 1–5. Sites 1 and 2 are actual survey locations; 2 in particular required picketed roped travel from the landing spot and is the steepest of the project. Site 3 is hypothetical and considered inaccessible, and so should be a limiting test. The complex impedance and tipper elements are plotted in Fig. 16. For plotting, the impedance Z_k is normalized relative to that at mesh 5 according to

$$\tilde{Z}_k(i,j,l,m) = \frac{Z_k(i,j,l,m)}{\frac{1}{2}|Z_5(1,2,l,m) - Z_5(2,1,l,m)|} \tag{28}$$

for $i = 1, 2$ $j = 1, 2$ for mesh k, receiver l and frequency m. The denominator in eq. (28) is the impedance invariant for mesh 5.

Fig. 16 shows good agreement across meshes and good convergence of the MT responses with mesh refinement. As a measure of error, a relative difference (RD) between the responses from mesh k and mesh 5 is computed in a normalized root-mean-square fashion:

$$\mathrm{RD}(k,5) = \sqrt{\frac{1}{12 N_{\mathrm{rec}} N_{\mathrm{freq}}} \sum_{l=1}^{N_{\mathrm{rec}}} \sum_{m=1}^{N_{\mathrm{freq}}} R^2_{l,m}} \tag{29}$$

where

$$R^2_{l,m} = \sum_{i=1}^{2}\sum_{j=1}^{2} \left|\tilde{Z}_k(i,j,l,m) - \tilde{Z}_5(i,j,l,m)\right|^2 + \sum_{j=1}^{2} \left|K_k(j,l,m) - K_5(j,l,m)\right|^2$$

Values of RD are listed in Table 1. With mesh refinement, the topography changes and the receivers shift modestly. This may be degrading the order of convergence slightly, which shows a value of about 0.8 instead of the ideal 1. Nevertheless, the relative differences are small compared to typical error floors adopted in 3-D inversion, for example 5 per cent on the impedance elements by Meqbel *et al.* (2014). This is achieved even for the receiver where local slope reaches 40 degrees.

As a second test, in Appendix B we present the results of a high frequency test similar to the one of Fig. 11 for the 2-D hill. For each receiver, we rotate the coordinate system such that the X and Y axes are parallel to the slope and the Z axis is perpendicular to the slope and calculate the MT response in those coordinates. We observe that as frequency increases, the apparent resistivity approaches 100 Ωm, the phase approaches 45°, and the tipper components approach 0 as should be expected. Note that the on-diagonal impedance elements in Fig. 16 also approach zero towards high frequency. The asymptotes occur near 100 Hz, above which results begin to diverge, although this is near the highest frequency usefully interpreted for a survey of this scale. We might expect further modest mesh changes as the project progresses, but these results demonstrate the efficacy of our approach to topographic modelling.

6.5 Jacobians test calculations

Next, we test the calculation of MT response Jacobians as they are essential for inversion purposes. We consider derivatives with respect to $\log_{10}$ resistivity model $m = (m_j)_{j=1}^{N_m}$, where in principle each m_j could be parsed as finely as a single FE. We consider the coarse 3-D hill mesh with receivers over the centres of surface element faces at $y = 0$ km. For the test parameter we use two adjacent FEs on the facing hill slope (Fig. 17). Jacobians are calculated using

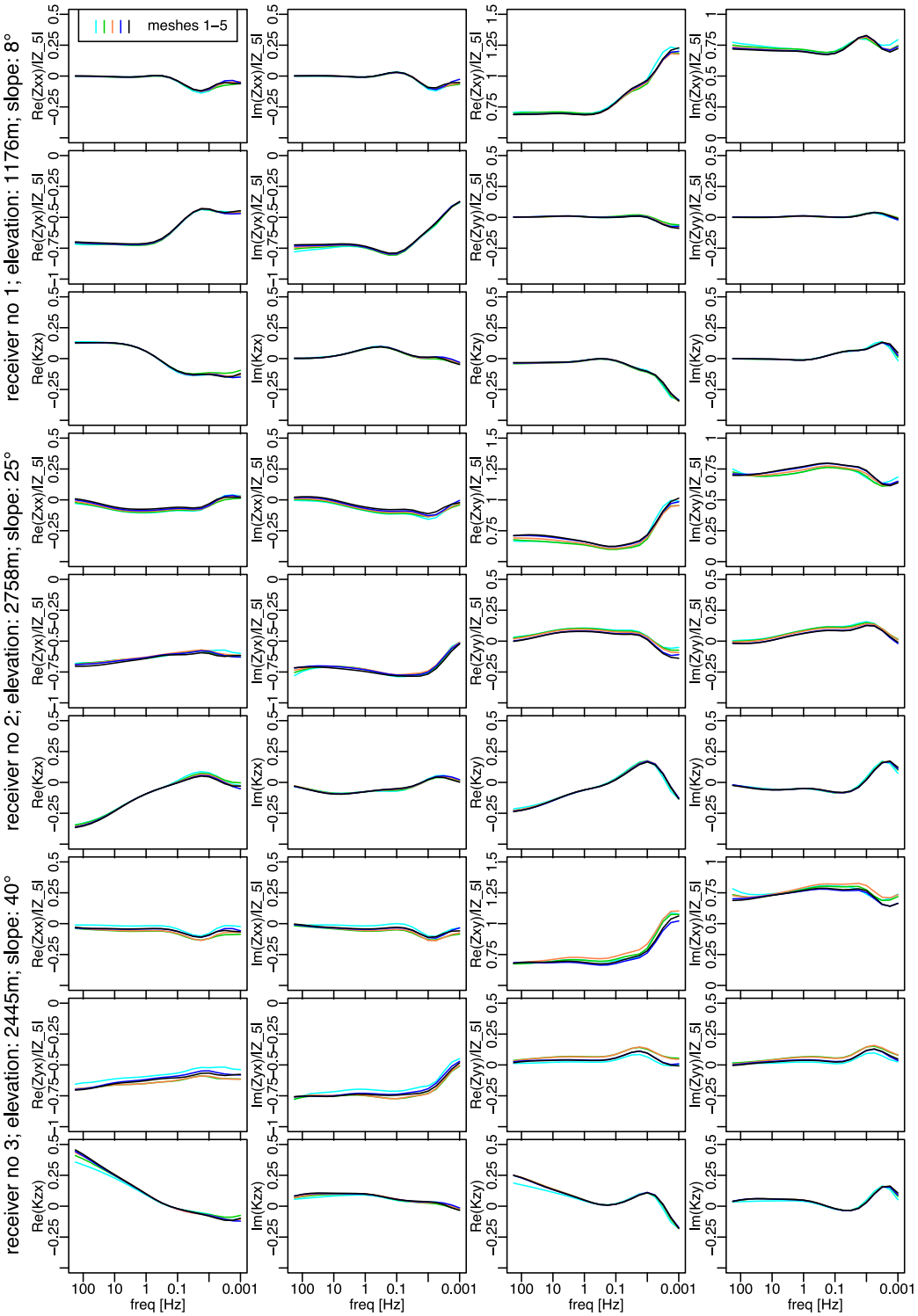

Figure 16. Normalized impedance $\tilde{Z}$ (eq. 28) and tipper K as a function of frequency for three receivers of the Mount Erebus model. The denominator in eq. (28) is abbreviated here as $|Z\_5|$.

Table 1. Comparison of the response of mesh k with the response of the finest mesh 5 for the three receivers together and separately using eq. (29).

	RD(1,5)	RD(2,5)	RD(3,5)	RD(4,5)
All 3 recs	2.36%	1.89%	1.69%	0.79%
rec 1	2.62%	2.28%	1.69%	0.88%
rec 2	1.5%	1.17%	0.7%	0.63%
rec 3	2.75%	2.04%	2.29%	0.85%

reciprocity as described previously and they are compared with a symmetric difference approximation of the derivative, that is,

$$\frac{\partial(Z,K)}{\partial m_j}(m) \approx \frac{(Z,K)(m+e_j h)-(Z,K)(m-e_j h)}{2h}$$

where e_j is a vector with only one nonzero entry at the jth position, which is equal to 1. In Fig. 18, we present the result of calculation for

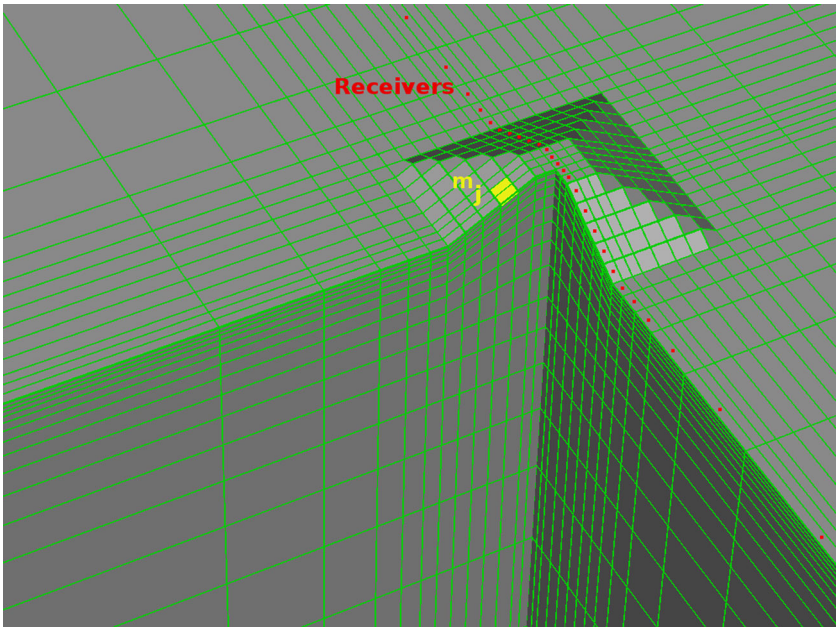

Figure 17. Central part of the coarse mesh of 3-D hill, together with the location of receivers and the chosen inversion cell m_j.

frequencies of 100 Hz and 0.001 Hz for all components of Z, K and for the inversion cell marked in the model figure. We used $h = 0.05$. A wide range of frequencies and various locations of the inversion cell have been tried, including the location under the receiver line. In all cases the values of the Jacobians showed very close agreement, with the relative difference no more than 0.2 per cent for non-zero components of the Jacobian.

7 EXAMPLE RUN TIMES

In Tables 2 and 3, we present run times related to solving eq. (8) with the MKL PARDISO library. Those run times constitute the main computational time of the forward modelling. For a model with a mesh $101x\,101y\,50z$ and 256 MT receivers other calculations (the calculation of the system matrix A and the source vectors b, sparse calculations related to divergence correction and the evaluation of the Jacobian, once the solutions $A^{-1}w$ are obtained) take about 13 per cent of the forward modelling time. The calculations were done on a 24 core workstation (four Intel Xeon E5-4607 v2 Hexa-core 2.60 GHz processors). Recall that MKL PARDISO finds a permutation matrix P (reordering phase), then calculates matrices L, D such that $P^TAP = LDL^T$ (factorization phase). Then L and D are used to solve linear system (8) for numerous rhs vectors b.

Times in the tables correspond to work done for a single frequency. In order to calculate full MT Jacobians, for each receiver location one needs to solve five linear systems (8). For example, 500 rhs in Table 3 would correspond to a survey with 100 receivers. As expected, run-time increase is geometric with respect to number of unknowns. In Table 2 we present the reordering time, which is about 10 times less than the factorization time with 24 cores. Here it is calculated using the sequential library METIS, which we found to be stable. METIS uses only one core; thus on a machine with more cores, the reordering time will become more significant. However, since reordering depends only on the non-zero pattern of the matrix and not on entry values, reordering is the same for every frequency so it may be reused for all frequencies following the first.

With a data-space parameter step formulation, as discussed in Part II, the inversion run time will be dominated by the forward problem and Jacobians. For the largest test mesh of Table 2 and assuming each element can be a parameter, a regular 400 site survey (20×20) could be inverted using a mesh with six columns of parameters per site in both x- and y-directions leaving nearly 30 columns of padding to far distances outside the survey domain.

8 CONCLUSIONS

FEs provide a flexible and accurate means of simulating EM responses of 3-D resistivity structure beneath topographic variations. Hexahedral elements provide a straightforward means of representing earth surface slopes, are compatible with the Helmholtz governing equation as discretization increases, and generate FE system matrices of simple structure. In particular, discretization requirements for topography at high frequencies are modest compared to those for traditional rectilinear meshes because layers of elements can lie parallel to the earth's surface. Further research is warranted into element discretization and geometry, applications for bathymetry and seafloor responses, and more complex background structures. By invoking an efficient current divergence correction, accurate E-field results may be obtained at very low frequencies and small admittivities, even those of dielectric air. Because we utilize a secondary field approach, it should be straightforward to generalize to finite source problems. As will be shown in Part II, hexahedral elements also provide a simple path to regularized inversion, for example by direct mapping of triaxial parameter roughness damping into deformed coordinates.

Efficient and affordable parallel computing solutions have emerged that are putting direct solutions to fairly large 3-D EM simulation problems within reach of an increasing number of users. These include a powerful public-domain library for direct solutions (MUMPS) that is seeing increased community use or a commercial library MKL PARDISO as exploited in this paper. Because the factorization provided by direct solvers allows economical solution

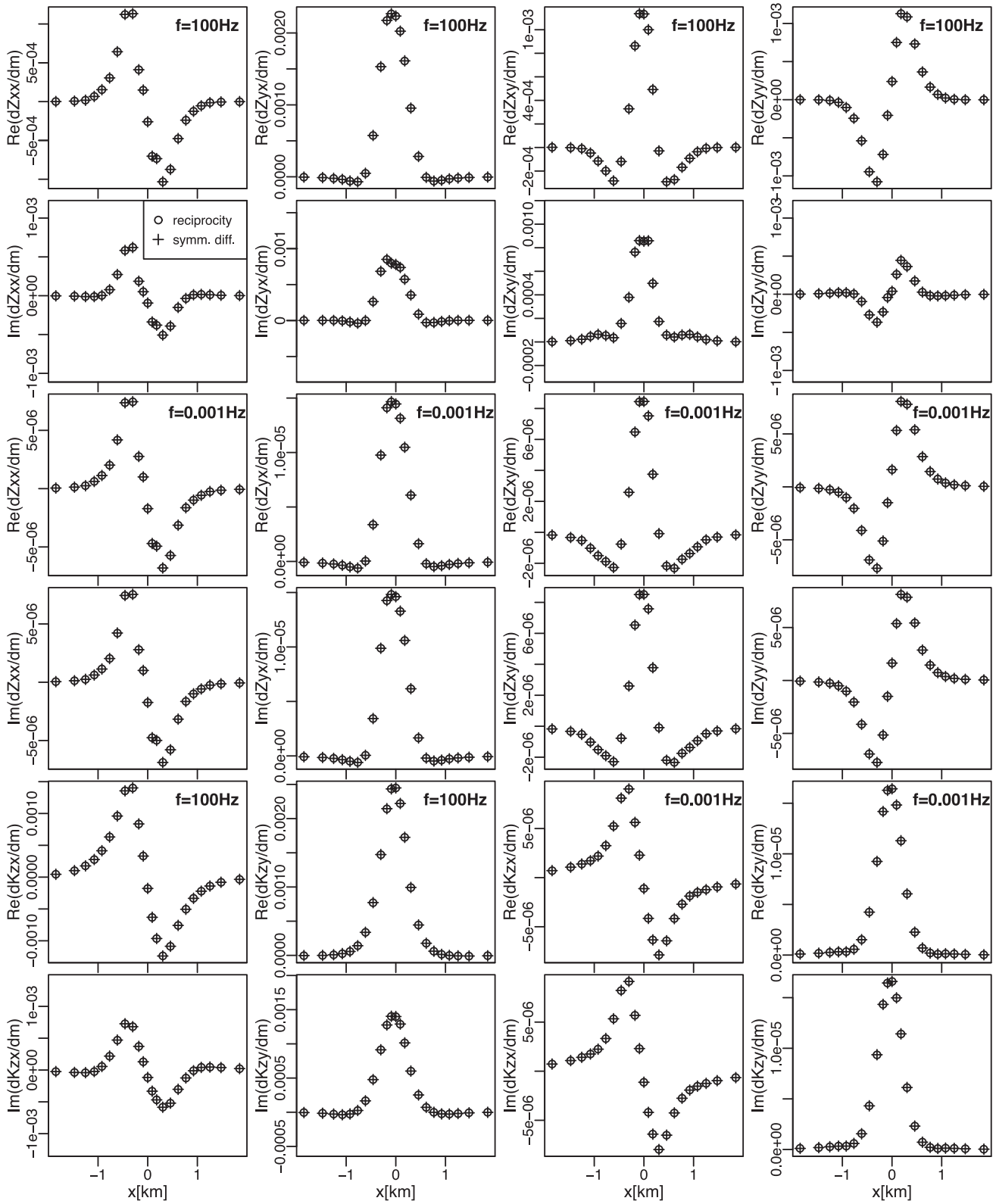

Figure 18. Comparison of a Jacobian of *Z*, *K* calculated using reciprocity and symmetric difference. The relative difference between the plotted values is less than 0.1 per cent.

of large numbers of source vectors, explicit and accurate values of parameter Jacobians can be obtained. Technological advances also include single-box, server-class workstations with numerous cores and substantial RAM that provide relatively affordable computing. Parallelization of the direct solver MKL PARDISO on multicore SMP computers is good, reaching an overall speedup of 15 on a 24 core machine for the forward problem calculations. Parallelization also could be increased with distributed computing using multiple

Table 2. MKL PARDISO analysis and factorization phase times (in min:sec) for factoring matrix A in eq. (8) for various meshes.

Mesh	Number of unknowns A	Number of non-zeroes in A	Number of non-zeroes in L	Reordering time	Factorization time	RAM memory used (GB)
30x 30y 25z	62 785	1 008 965	24 225 432	00:01	00:01	0.68
50x 50y 35z	250 635	4 111 215	180 177 821	00:05	00:13	4.17
75x 75y 45z	734 820	12 179 490	770 644 591	00:17	01:00	14.55
100x 100y 50z	1 460 250	24 316 190	1 981 092 177	00:37	03:48	35.09
125x 125y 55z	2 519 680	42 085 390	4 135 494 960	01:08	10:55	70.41
150x 150y 60z	3 969 360	66 443 340	7 022 172 676	01:53	21:03	117.10
176x 176y 70z	6 394 150	107 274 730	14 344 449 730	03:18	64:10	233.80

Table 3. MKL PARDISO solution phase time (in min:sec) for the linear system (8), for various meshes and numbers of rhs vectors b.

Mesh	100 rhs	500 rhs	1000 rhs	1500 rhs	2000 rhs
30x 30y 25z	00:01	00:03	00:07	00:10	00:13
50x 50y 35z	00:02	00:11	00:23	00:34	00:45
75x 75y 45z	00:11	00:54	01:48	02:42	03:36
100x 100y 50y	00:05	00:23	00:46	01:10	01:33
125x 125y 55z	01:24	06:58	13:57	20:55	27:53
150x 150y 60z	02:09	10:47	21:34	32:22	43:09
176x 176y 70z	03:41	18:23	36:47	55:10	73:34

SMP. Nevertheless, direct simulations including Jacobians can be done on a single workstation for meshes with one million elements in less than 1 hr per frequency.

ACKNOWLEDGEMENTS

We acknowledge the support for this work from the U.S. Department of Energy under contract DE-EE0002750 and the U.S. National Science Foundation under grant AES-1443522 to PW. EC acknowledges the partial support of the U.S. National Science Foundation through grants ARC-0934721 and DMS-1413454. GH acknowledges the support of the Royal Society of New Zealand through grant ASL-1301. The University of Utah/EGI funded acquisition of the 24-core workstations. Drs. Rita Streich and Martin Čuma are thanked for discussions on libraries for direct solutions of sparse systems. Belinda Lyttle of the New Zealand GNS Science organization kindly provided the Ross Island and surroundings DEM. Presentation and content of the paper were improved substantially following the remarks of three anonymous reviewers. The submission was handled by Associate Editor Ute Weckmann.

REFERENCES

Adams, R. & Fournier, J., 2003. *Sobolev Spaces,* Elsevier Science.

Amestoy, P.R., Duff, I.S., Koster, J. & L'Excellent, J.-Y., 2001. A fully asynchronous multifrontal solver using distributed dynamic scheduling, *SIAM J. Matrix Anal. Appl.,* **23**(1), 15–41.

Amestoy, P.R., Guermouche, A., L'Excellent, J.-Y. & Pralet, S., 2006. Hybrid scheduling for the parallel solution of linear systems, *Parallel Comput.,* **32**(2), 136–156.

Amrouche, C., Bernardi, C., Dauge, M. & Girault, V., 1998. Vector potentials in three-dimensional non-smooth domains, *Math. Methods Appl. Sci.,* **21**(9), 823–864.

Börner, R.-U., 2010. Numerical modelling in geo-electromagnetics: advances and challenges, *Surv. Geophys.,* **31,** 225–245.

Börner, R.-U., Ernst, O.G. & Spitzer, K., 2008. Fast 3D simulations of transient electromagnetic fields by model reduction in the frequency domain using Krylov subspace projection, *Geophys. J. Int.,* **173,** 766–780.

Chave, A.D. & Jones, A.G., 2012. *The Magnetotelluric Method: Theory and Practice,* Cambridge Univ. Press.

Commer, M. & Newman, G.A., 2008. New advances in three-dimensional controlled-source electromagnetic inversion, *Geophys. J. Int.,* **172,** 513–535.

Csatho, B., Schenk, T., Kyle, P., Wilson, T. & Krabill, W.B., 2008. Airborne laser swath mapping of the summit of Erebus volcano, Antarctica: applications to geological mapping of a volcano, *J. Volc. Geotherm. Res.,* **177**(3), 531–548.

daSilva, N.V., Morgan, J.V., MacGregor, L. & Warner, M., 2012. A finite element multi-frontal method for 3D CSEM modeling in the frequency domain, *Geophysics,* **77,** E101–E115.

Davey, F.J., 2004. *Ross Sea bathymetry,* Institute of Geological & Nuclear Sciences, Geophys. Map 1172-0301, 1:2,000,000.

deGroot-Hedlin, C. & Constable, S., 1990. Occam's inversion to generate smooth, two-dimensional models from magnetotelluric data, *Geophysics,* **55**(12), 1613–1624.

deLugao, P.P. & Wannamaker, P.E., 1996. Calculating the two-dimensional magnetotelluric Jacobian in finite elements using reciprocity, *Geophys. J. Int.,* **127,** 806–810.

Everett, M.E., 2012. Theoretical developments in electromagnetic induction geophysics with selected applications in the near-surface, *Surv. Geophys.,* **33,** 29–63.

Falk, R.S., Gatto, P. & Monk, P., 2011. Hexahedral H (div) and H (curl) finite elements, *ESAIM: Math. Modelling Numer. Anal.,* **45**(01), 115–143.

Farquharson, C.G. & Miensopust, M., 2011. Three-dimensional finite-element modeling of magnetotelluric data with a divergence correction, *J. Appl. Geophys.,* **75,** 699–710.

Girault, V. & Raviart, P.-A., 1986. *Finite Element Methods for Navier-Stokes Equations: Theory and Algorithms,* Springer.

Grayver, A.V., Streich, R. & Ritter, O., 2013. Three-dimensional parallel distributed inversion of CSEM data using a direct forward solver, *Geophys. J. Int.,* **193,** 1432–1446.

Gunzburger, M.D. & Bochev, P.B., 2009. *Least-Squares Finite Element Methods,* Springer.

Haber, E., Ascher, U., Aruliah, D. & Oldenburg, D., 2000. Fast simulation of 3D electromagnetic problems using potentials, *J. Comput. Phys.,* **163**(1), 150–171.

Haber, E., Oldenburg, D.W. & Shekhtman, R., 2007. Inversion of time domain three-dimensional electromagnetic data, *Geophys. J. Int.,* **171**(2), 550–564.

Hill, G.J., Wannamaker, P.E., Wallin, E.L., Unsworth, M.J., Stodt, J.A. & Ogawa, Y., 2015. The Mount Erebus (Ross Dependency – Antarctica) magmatic system from surface to source: insights from magnetotelluric

measurements, in *NZARI Antarctic Science Conference 'Antarctica - A Changing Environment',* June 29–July 2, Christchurch, New Zealand.
Hohmann, G.W., 1988. Numerical modeling for electromagnetic methods of geophysics, in *Electromagnetic Methods in Applied Geophysics — Theory,* vol. 1, pp. 313–363, ed Nabighian, M.N., Society of Exploration Geophysicists, Tulsa, OK.
Hohmann, G.W. & Raiche, A.P., 1988. Inversion of controlled-source electromagnetic data, in *Electromagnetic Methods in Applied Geophysics—Theory,* vol. 1, pp. 469–503, ed. Nabighian, M.N., Society of Exploration Geophysicists, Tulsa, OK.
Hyman, J.M. & Shashkov, M., 1999. Mimetic discretizations for Maxwell's equations, *J. Comput. Phys.,* **151**(2), 881–909.
Jahandari, H. & Farquharson, C.G., 2014. A finite-volume solution to the geophysical electromagnetic forward problem using unstructured grids, *Geophysics,* **79,** E287–E302.
Karypis, G., 2003. Multi-constraint mesh partitioning for contact/impact computations, in *Proc. SC2003,* Phoenix, AZ, ACM.
Key, K. & Constable, S., 2011. Coast effect distortion of marine magnetotelluric data: insights from a pilot study offshore northeastern Japan, *Phys. Earth planet. Inter.,* **184,** 194–207.
Kordy, M., Maris, V., Wannamaker, P. & Cherkaev, E., 2013. 3D edge finite element solution for scattered electric field using a direct solver parallelized on an SMP workstation, in *5th International Symposium on Three-Dimensional Electromagnetics,* Sapporo, May 7–9, p. 4.
Kordy, M., Cherkaev, E. & Wannamaker, P., 2015a. Variational formulation for Maxwell's equations with Lorenz gauge: existence and uniqueness of solution, *Int. J. Numer. Anal. Model.,* **12**(4), 731–749.
Kordy, M., Wannamaker, P., Maris, V., Cherkaev, E. & Hill, G.J., 2015b. Three-dimensional magnetotelluric inversion including topography using deformed hexahedral edge finite elements and direct solvers parallelized on SMP computers, Part II: Direct data-space inverse solution, *Geophys. J. Int.,* doi:10.1093/gji/ggv411.
Lelièvre, P.G. & Farquharson, C.G., 2013. Gradient and smoothness regularization operators for geophysical inversion on unstructured meshes, *Geophys. J. Int.,* **195,** 330–341.
Liu, J., Brio, M. & Moloney, J., 2009. Overlapping Yee FDTD method on nonorthogonal grids, *J. Sci. Comput.,* **39**(1), 129–143.
Mackie, R.L., Bennett, B.R. & Madden, T.R., 1988. Long-period magnetotelluric measurements near the central California coast: a land-locked view of the conductivity structure under the Pacific Ocean, *Geophys. J. Int.,* **95,** 181–194.
Mackie, R.L., Madden, T.R. & Wannamaker, P.E., 1993. Three-dimensional magnetotelluric modeling using difference equations – theory and comparisons to integral equation solutions, *Geophysics,* **58,** 215–226.
Macnae, J., 2010. Electric field measurements in air, in *80th Annual International Meeting,* Expanded Abstract, SEG, Denver, pp. 1773–1777.
Madden, T.R. & Mackie, R.L., 1989. Three-dimensional magnetotelluric modelling and inversion, *Proc. IEEE,* **77**(2), 318–333.
Maris, V. & Wannamaker, P.E., 2010. Parallelizing a 3D finite difference MT inversion algorithm on a multicore PC using OpenMP, *Comput. Geosci.,* **36**(10), 1384–1387.
McGillivray, P., Oldenburg, D., Ellis, R. & Habashy, T., 1994. Calculation of sensitivities for the frequency-domain electromagnetic problem, *Geophys. J. Int.,* **116**(1), 1–4.
Meqbel, N.M., Egbert, G.D., Wannamaker, P.E., Kelbert, A. & Schultz, A., 2014. Deep electrical resistivity structure of the northwestern U.S. derived from 3-D inversion of USArray magnetotelluric data, *Earth planet. Sci. Lett.,* **402,** 290–304.
Mitsuhata, Y. & Uchida, T., 2004. Three-dimensional magnetotelluric modeling using the $t - \omega$ finite element method, *Geohysics,* **69,** 108–119.
Monk, P., 1992. A finite element method for approximating the time-harmonic Maxwell equations, *Numer. Math.,* **63**(1), 243–261.
Moussallam, Y., Oppenheimer, C., Scaillet, B. & Kyle, P.R., 2013. Experimental phase-equilibrium constraints on the phonolite magmatic system of Erebus Volcano, Antarctica, *J. Petrol.,* **54**(7), 1285–1307.
Nam, M.J., Kim, H.J., Song, Y., Lee, T.J., Son, J.-S. & Suh, J.H., 2007. Three-dimensional magnetotelluric modeling including surface topography, *Geophys. Prospect.,* **55,** 277–287.
Nédélec, J.-C., 1986. A new family of mixed finite elements in $\mathbf{R}^3$, *Numer. Math.,* **50**(1), 57–81.
Newman, G.A. & Alumbaugh, D.L., 2000. Three-dimensional magnetotelluric inversion using non-linear conjugate gradients, *Geophys. J. Int,* **140,** 410–424.
Oldenburg, D.W., Haber, E. & Shekhtman, R., 2008. Forward modeling and inversion of multi-source TEM data, in *78th Annual International Meeting,* Expanded Abstract, SEG, Las Vegas, pp. 559–563.
Oldenburg, D.W., Haber, E. & Shekhtman, R., 2013. Three dimensional inversion of multi-source time domain electromagnetic data, *Geophysics,* **78**(1), E47–E57.
Pridmore, D.F., Hohmann, G.W., Ward, S.H. & Sill, W.R., 1981. An investigation of finite element modeling for electrical and electromagnetic data in three dimensions, *Geophysics,* **46,** 1009–1024.
Ren, Z., Kalscheuer, T., Greenhalgh, S. & Maurer, H., 2013. A goal-oriented adaptive finite-element approach for plane wave 3-D electromagnetic modelling, *Geophys. J. Int.,* **194,** 700–718.
Roy, K.K., 2007. *Potential Theory in Applied Geophysics,* Springer Science & Business Media.
Sasaki, Y., 2001. Full 3-D inversion of electromagnetic data on PC, *J. Appl. Geophys.,* **46,** 45–54.
Schenk, O. & Gärtner, K., 2004. Solving unsymmetric sparse systems of linear equations with PARDISO, *Future Gener. Comput. Syst.,* **20**(3), 475–487.
Schwarzbach, C., 2009. Stability of finite element solutions to Maxwell's equations in frequency domain, *PhD thesis,* Freiberg University of Mining and Technology.
Schwarzbach, C. & Haber, E., 2013. Finite element based inversion for time-harmonic electromagnetic problems, *Geophys. J. Int.,* **193,** 615–634.
Siripunvaraporn, W., Egbert, G. & Lenbury, Y., 2002. Numerical accuracy of magnetotelluric modeling: a comparison of finite difference approximations, *Earth Planets Space,* **54,** 721–725.
Siripunvaraporn, W., Egbert, G., Lenbury, Y. & Uyeshima, M., 2005. Three-dimensional magnetotelluric inversion: data-space method, *Phys. Earth planet. Inter.,* **150,** 3–14.
Smith, J., 1996. Conservative modeling of 3-D electromagnetic fields, Part II: biconjugate gradient solution and an accelerator, *Geophysics,* **61**(5), 1319–1324.
Streich, R., 2009. 3D finite-difference frequency-domain modeling of controlled-source electromagnetic data: direct solution and optimization for high accuracy, *Geophysics,* **74,** F95–F105.
Tarantola, A., 2005. *Inverse Problem Theory and Methods for Model Parameter Estimation,* SIAM.
Trottenberg, U., Oosterlee, C.W. & Schuller, A., 2000. *Multigrid,* Academic press.
Um, E.S., Harris, J.M. & Alumbaugh, D.L., 2012. An iterative finite element time-domain method for simulating three-dimensional electromagnetic diffusion in the earth, *Geophys. J. Int.,* **190,** 871–886.
Um, E.S., Commer, M., Newman, G.A. & Hoversten, G.M., 2015. Finite element modelling of transient electromagnetic fields near steel-cased wells, *Geophys. J. Int.,* **202**(2), 901–913.
Usui, Y., 2015. 3-D inversion of magnetotelluric data using unstructured tetrahedral elements: applicability to data affected by topography, *Geophys. J. Int.,* **202**(2), 828–849.
Vardapetyan, L. & Demkowicz, L., 1999. hp-adaptive finite elements in electromagnetics, Comput. Methods Appl. Mech. Eng., **169**(3), 331–344.
Wannamaker, P., Stodt, J. & Rijo, L., 1986. Two-dimensional topographic responses in magnetotelluric modeling using finite elements, *Geophysics,* **51,** 2131–2144.
Wannamaker, P.E., 1991. Advances in three-dimensional magnetotelluric modeling using integral equations, *Geophysics,* **56,** 1716–1728.
Weaver, J.T., LeQuang, B.V. & Fischer, G., 1985. A comparison of analytic and numerical results for a two-dimensional control model in electromagnetic induction—I. B-polarization calculations, *Geophys. J. R. astr. Soc.,* **82,** 263–277.
Weaver, J.T., LeQuang, B.V. & Fischer, G., 1986. A comparison of analytic and numerical results for a two-dimensional control model in

electromagnetic induction—II. E-polarization calculations, *Geophys. J. R. astr. Soc.*, **87,** 917–948.

Zhdanov, M.S., Varentsov, I.M., Weaver, J.T., Golubev, N.G. & Krylov, V.A., 1997. Methods for modelling electromagnetic fields: results from COMMEMI - the international project on the comparison of modelling methods for electromagnetic induction, *J. Appl. Geophys.*, **37,** 133–271.

APPENDIX A

To explain the ill-conditioning related to spurious curl-free E-fields, let us analyse eigenvalues of the system matrix A. A good approximation of those eigenvalues are eigenvalues of the operator

$$\mathcal{L}(M) = \nabla \times \left(\frac{1}{\mu}\nabla \times M\right) + \mathrm{i}\omega\hat{\sigma} M. \tag{A1}$$

$\mathcal{L}$ should be defined on some suitable finite dimensional space, dependent on the mesh size h. First, let us consider infinite dimensional space of vector fields $M \in \mathcal{H}_0(\nabla\times, \Omega)$, with the additional assumption that $\nabla \times \frac{1}{\mu}\nabla \times M$ exists and is square integrable. Let the domain be a cube $\Omega = [0, M]^3$ with $\hat{\sigma}, \mu = \text{const}$. It is straightforward to verify that the eigenvectors of $\mathcal{L}$ are of the form

$$v = \begin{bmatrix} C_x \cos\left(\pi\frac{k_x}{M}x\right)\sin\left(\pi\frac{k_y}{M}y\right)\sin\left(\pi\frac{k_z}{M}z\right) \\ C_y \sin\left(\pi\frac{k_x}{M}x\right)\cos\left(\pi\frac{k_y}{M}y\right)\sin\left(\pi\frac{k_z}{M}z\right) \\ C_z \sin\left(\pi\frac{k_x}{M}x\right)\sin\left(\pi\frac{k_y}{M}y\right)\cos\left(\pi\frac{k_z}{M}z\right) \end{bmatrix} \tag{A2}$$

for $k_x, k_y, k_z \in \mathbb{N}$ where

$$C = \begin{bmatrix} C_x \\ C_y \\ C_z \end{bmatrix} = \begin{bmatrix} k_x \\ k_y \\ k_z \end{bmatrix}, \begin{bmatrix} -k_z \\ 0 \\ k_x \end{bmatrix} \text{ or } \begin{bmatrix} 0 \\ k_z \\ -k_y \end{bmatrix}. \tag{A3}$$

Defining $|k|^2 = k_x^2 + k_y^2 + k_z^2$ one can write the corresponding eigenvalues as:

$$\lambda = \mathrm{i}\omega\hat{\sigma}, \quad \frac{\pi^2|k|^2}{\mu M^2} + \mathrm{i}\omega\hat{\sigma}, \quad \frac{\pi^2|k|^2}{\mu M^2} + \mathrm{i}\omega\hat{\sigma}. \tag{A4}$$

By checking that $\mathcal{L}(v) = \lambda v$, one can verify that v and λ are the eigenvectors and eigenvalues of $\mathcal{L}$. For an infinite dimensional space, we have $3 < |k|^2 < \infty$, yet for a discretization, with spatial mesh parameter h, it would be:

$$3 \le |k|^2 \le O\left(3\left(\frac{M}{h}\right)^2\right). \tag{A5}$$

The upper bound above would be correct if we used a finite difference discretization of the Laplacian (Trottenberg *et al.* 2000). We use it for the curl as it is also a second-order differential operator. One could consider also that in a discretized version of $\mathcal{L}$, roughly speaking, the natural numbers k_x, k_y, k_z would be allowed to vary from 1 to M/h.

Let us look at those eigenvalues for some practical setting for magnetotellurics. Let $M = 10$ km, $\frac{M}{h} = 50$. The quantity $\frac{\pi^2|k|^2}{\mu M^2}$ is in the interval $[2 \times 10^{-1}, 6 \times 10^{+2}]$. The values of the first eigenvalue $i\omega\hat{\sigma}$ for conductivity corresponding to the Earth's subsurface ($\hat{\sigma} = 0.01$ Sm^{-1}) and air ($\hat{\sigma} = i\omega\epsilon_0$) are presented in Table A1. The corresponding condition numbers of the system matrix, defined as $\text{cond}(A) = \frac{\max(|\lambda|)}{\min(|\lambda|)}$ are presented in Table A2. One can see that if a conductivity corresponding to the ground is used, the condition number increases as the frequency decreases, yet remains at a reasonable level of 10^{+5} even for frequency as small as 0.01 Hz. If conductivity of the air is used, the situation is different. As the frequency decreases, the condition number increases quadratically and reaches very large value of 10^{+16} for the frequency 0.01 Hz.

Table A1. Values of $|\omega\hat{\sigma}|$ for different σ and ω. Unit of $|\omega\hat{\sigma}|$ is S Hz m^{-1}.

ω	2π 100 Hz	2π 1 Hz	2π 0.01 Hz
Earth: $\hat{\sigma} = 0.01$ S m^{-1}	6.3	6.3×10^{-2}	6.3×10^{-4}
Air: $\hat{\sigma} = \mathrm{i}\omega\epsilon_0$	3.5×10^{-6}	3.5×10^{-10}	3.5×10^{-14}

Table A2. Condition number of the system matrix A as a function of frequency ω and $\hat{\sigma}$.

ω	2π 100 Hz	2π 1 Hz	2π 0.01 Hz
Earth: $\hat{\sigma} = 0.01$ S m^{-1}	$9.3 \times 10^{+1}$	$9.3 \times 10^{+3}$	$9.3 \times 10^{+5}$
Air: $\hat{\sigma} = \mathrm{i}\omega^2\epsilon_0$	$1.7 \times 10^{+8}$	$1.7 \times 10^{+12}$	$1.7 \times 10^{+16}$

In MTs, the domain contains both earth and air. Because of the presence of the air, the matrix is ill-conditioned. Nevertheless, the calculated electric field, approximated by solving eq. (8) using a direct solver, and using eq. (7) has improper values only in the air. The electric field below the Earth's surface does not suffer from numerical instability. It is also worth mentioning, that the magnetic field, calculated using the curl of electric field as in eq. (11) has proper values in all of the domain. It shows, that the error added to the electric field in the air is curl-free.

The condition number of the matrix gets this large because of the smallness of the eigenvalue $\lambda = \mathrm{i}\omega\hat{\sigma}$, corresponding to the first C in eq. (A3). Note that the corresponding eigenvector is curl-free, whereas the other two are not. Moreover the first eigenvector is equal to $\nabla\varphi$, where

$$\varphi = \frac{M}{\pi}\sin\left(\pi\frac{k_x}{M}x\right)\sin\left(\pi\frac{k_y}{M}y\right)\sin\left(\pi\frac{k_z}{M}z\right) \tag{A6}$$

and $\varphi|_{\partial\Omega} = 0$. This is not a coincidence. In fact, in this case the conductivity $\hat{\sigma}$ is constant in the domain, and the Hodge decomposition discussed in 'Divergence correction' section is the standard Helmholtz decomposition. The eigenvectors of $\mathcal{L}$ span the space $H_0(\nabla\times, \Omega)$ respecting the decomposition. The eigenvectors with the first C of eq. (A3) span the space $R(\nabla)$, the eigenvectors with the second and the third C of eq. (A3) span $R(\nabla)^{\perp_{\hat{\sigma}}}$. The eigenvectors form an orthogonal basis of $\mathcal{H}_0(\nabla\times, \Omega)$ and the spaces $R(\nabla)$ and $R(\nabla)^{\perp_{\hat{\sigma}}}$ are orthogonal.

APPENDIX B

Here we present a 3-D high frequency test similar to the one of Fig. 11 for the 2-D hill. Again, if skin depth in the subsurface is much less than the scale of topographic variation, the incident EM wave should refract normal to the slope and behave as if the surface is locally flat and horizontal (Wannamaker *et al.* 1986). For each receiver considered in the Mount Erebus model, we rotate the coordinate system such that X and Y axes are parallel to the slope and Z axis is perpendicular to the slope. The MT response is calculated in those coordinates. The apparent resistivity and impedance phase calculated using Z_{xy}, $-Z_{yx}$, and $\frac{1}{2}(Z_{xy} - Z_{yx})$ as a function of frequency

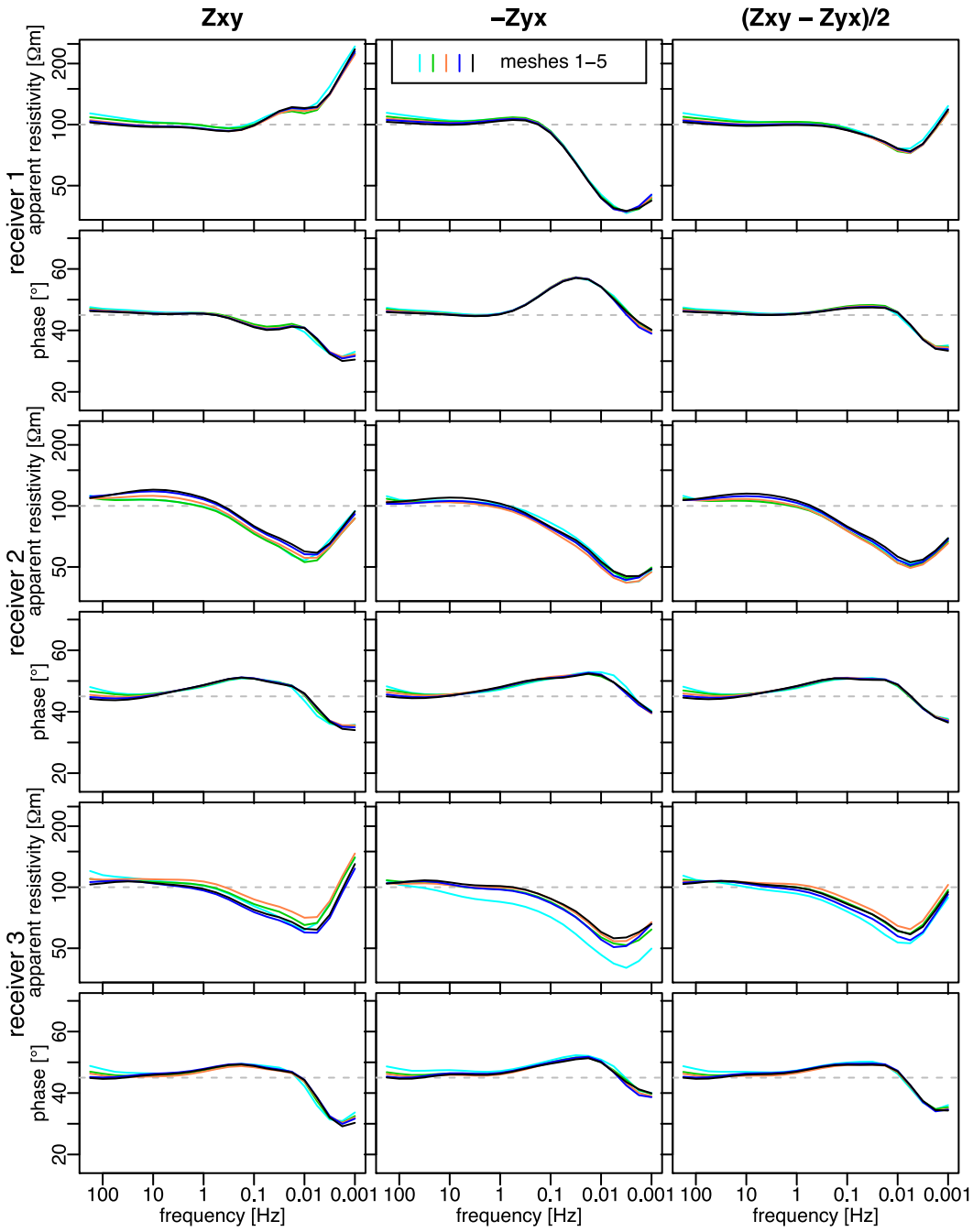

Figure B1. Apparent resistivity and impedance phase as a function of frequency for three receivers of the Mount Erebus model. The coordinate system in which the impedance is calculated has X and Y axes parallel to the slope and the Z axis perpendicular to it.

are presented in Fig. B1. We observe that as frequency becomes high, towards 100 Hz, the apparent resistivity approaches 100 Ωm and impedance phase approaches 45°, which is the response of the 100 Ωm half-space. Similarly, the tipper elements (see Fig. B2) approach 0 at high frequencies. The best results are obtained for meshes 4 and 5 where cell thicknesses become a smaller fraction of skin depth. The elements next to the Earth's surface have thickness of 100 m for mesh 1 and 25 m for mesh 5. Results begin to degrade much above 100 Hz even for mesh 5, and would require even finer discretization.

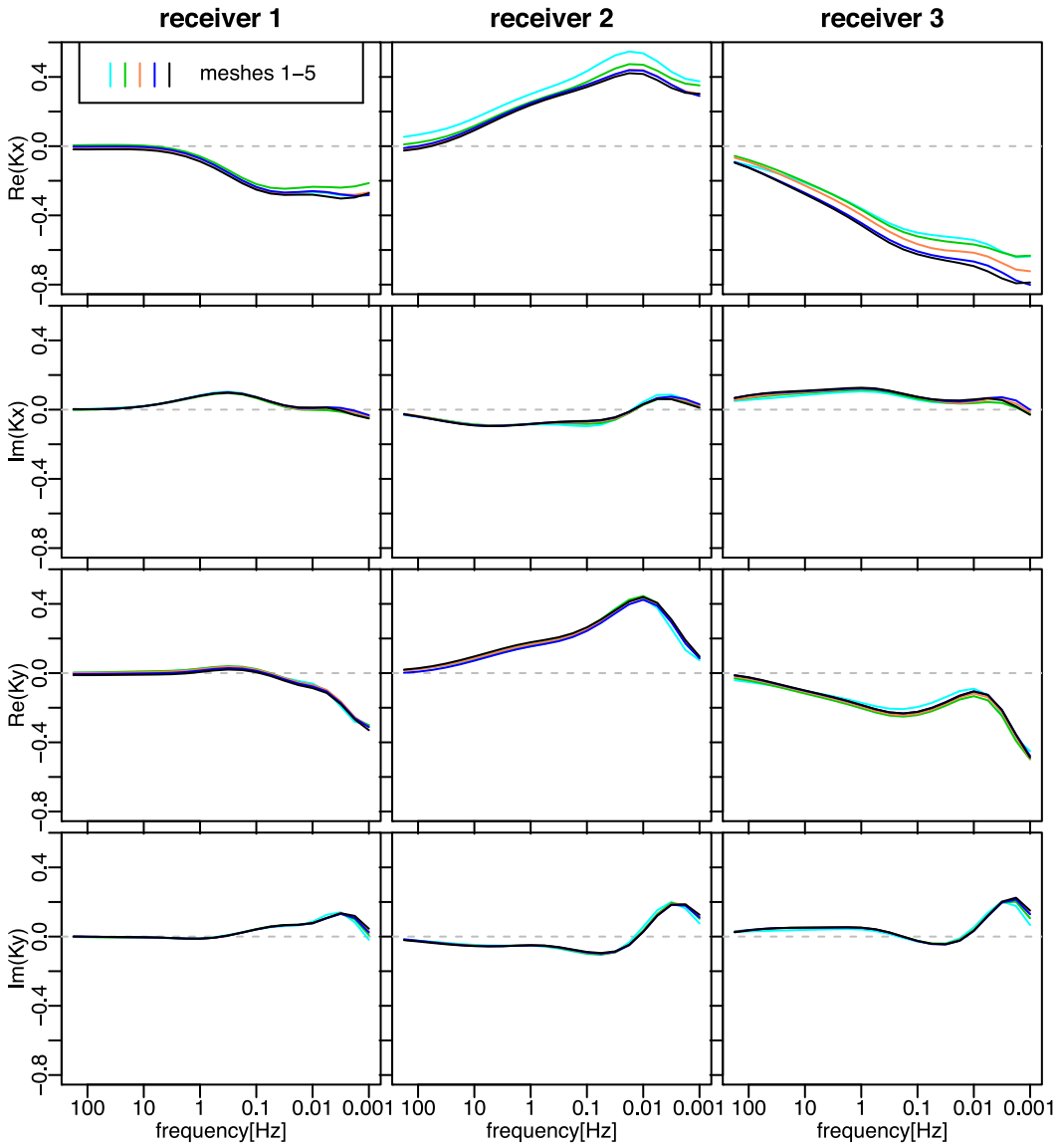

Figure B2. Complex tipper elements as a function of frequency for three receivers of the Mount Erebus model. The coordinate system in which the tipper is calculated has *X* and *Y* axes parallel to the slope and the *Z* axis perpendicular to it.